Communication and Synchronization Schemes for Chirp Sequence-based Automotive Radar Systems

Zur Erlangung des akademischen Grades eines

DOKTORS DER INGENIEURWISSENSCHAFTEN
(Dr.-Ing.)

von der KIT-Fakultät für
Elektrotechnik und Informationstechnik
des Karlsruher Instituts für Technologie (KIT)

angenommene

DISSERTATION

von

M.Sc. Mohamad Basim Alabd

geboren in Homs, Syrien

Tag der mündlichen Prüfung: 30.07.2024

Hauptreferent: Prof. Dr.-Ing. Dr. h.c. Thomas Zwick
Korreferent: Prof. Dr.-Ing. Christian Waldschmidt

Abstract

Radar technology has experienced massive developments over the past deca-
de. These traits have maintained the performance requirements and initiated a
new era of applications varying from self-autonomous driving to monitoring.
Among the investigated technologies, chirp sequence (CS) radar systems have
been employed by radar manufacturers as a promising approach to enhance
the conventional slow dual ramp (FMCW) and maximize its ability to detect
objects in the surroundings. However, in complex environments with more than
one radar sensor nearby, interference events can drastically degrade the overall
performance of detection. This drawback can be represented as the appearance
of ghost targets and the error in estimating the correct position of the actual
counterparts because of the high noise floor level. Accordingly, mitigating in-
terference while preserving radar performance has been investigated in the last
decade, and researchers have suggested algorithms be applied to the time or fre-
quency domain. These solutions require extra steps within the signal processing
chain that can be presumed within the operating cycle. Another vital approach
to avoid or minimize interference events focuses on integrating communication
data into radar signals so that the sensors can exchange vital parameters like
bandwidth and time duration of their signals in a shared spectrum of two func-
tionalities. Since the investigated systems in automotive applications are mainly
radar-centric, facilitating communications capabilities while keeping the desi-
red detection performance is required during the system design. Inspired by
shared spectrum systems, this thesis presents a novel CS-based radar concept
under the definition of "Communication-assisted Chirp Sequence system" that
ensures regular detection and data exchange between communicating radar no-
des through signal processing techniques and careful system design. Besides,
the investigation proposes a separate communication receiver architecture com-
patible with the radar transceiver to ascertain the level of freedom in completing
radar measurements. Following this, the thesis comprises two novel communi-
cation techniques and a synchronization approach between two communicating
radar nodes to achieve seamless data exchange. Based on the first technique,

the communication symbols are partially modulated at the top or bottom of each chirp to limit the impact on the inference process, whereas modulating the entire chirp reduces detection quality. The second technique splits each chirp into two components with predetermined pairwise time-frequency offsets derived from the Long Range Communication (LoRa) scheme, where each chirp represents a communication symbol. Nevertheless, the signal-processing chain should be modified to compensate for deviations in the time-frequency plane within the signal model. Furthermore, an innovative synchronization approach is proposed that allows the receiver of one communicating node to realign the transmitted signal in the time-frequency plane and initialize the demodulation process. The proposed approach is based on image-like processing, using short-time Fourier transform (STFT) and linear regression (LR) to generate a two-dimensional grid of signal points in the time-frequency plane. In addition, this study comprises an innovative interference detection mechanism to analyze the impact of interference on the synchronization between the communicating nodes in the environment. In this sense, the proposed synchronization approach can be extended to support multi-user scenarios, or a matched filter method can be designed when the signal parameters are known. Multiple measurements also validate the novel system on a KIT laboratory demonstrator at 79 GHz. For this purpose, the measurement campaign was built based on two subharmonic mixers, amplifiers, signal generators, antennas, and RFSoC. Furthermore, simulations were performed using MATLAB to analyze the system, employing parameters similar to those used in the measurements.

In conclusion, this thesis proposes an innovative CS-based radar system extended with communication features to minimize mutual interference by exchanging vital data between radars in the same environment. This integration will also establish a cornerstone in future 6G networks on the strength of the proposed shared sensing and communication systems.

Zusammenfassung

In den letzten Jahren haben bedeutende Fortschritte in der Radartechnologie, einschließlich höherer Auflösung, größerer Multifunktionalität und der Entwicklung von Radarchips, nicht nur die Fähigkeiten herkömmlicher Radarsysteme erhalten, sondern auch eine neue Ära von Radaranwendungen eingeläutet, die von autonomen Fahrzeugen bis hin zur Umweltüberwachung reichen. Unter diesen innovativen Entwicklungen haben sich Chipsequenz (engl. *Chirp Sequence*) Radarsysteme als vielversprechender Ansatz zur Verbesserung des klassischen FMCW (langsame Doppelrampen) und zur Maximierung ihres Potenzials bei der Erkennung von Zielen in der Umgebung erwiesen. In komplexen Umgebungen, in denen mehrere Radarsensoren naheinander arbeiten, können jedoch Interferenzen zwischen diesen Sensoren ihre Leistung erheblich beeinträchtigen und die Erkennungsqualität beeinträchtigen, was zu verpassten Erkennungen und ungenauer Ziellokalisierung führen kann, wodurch die Gesamteffizienz der untersuchten Radarsysteme eingeschränkt wird. Die Herausforderung, Interferenzen abzuschwächen und gleichzeitig die Wirksamkeit des Radars aufrechtzuerhalten, hat zur Entwicklung mehrerer Lösungen geführt, die entweder im Zeit- oder im Frequenzbereich eingesetzt werden können.

Ein weiterer wichtiger Ansatz, auf den sich diese Arbeit konzentriert, ist die Integration von Kommunikationsdaten in das Radarsignal, so dass die Sensoren kommunizieren und ihre wesentlichen Parameter (z.B. Bandbreite, Zeitdauer) austauschen können, um Interferenzen mit anderen Signalen zu vermeiden, die sich in der Umgebung ausbreiten und der Erkennung dienen. Dennoch ist die Aufrechterhaltung der Radarperformance bei gleichzeitiger Ermöglichung von Kommunikationsfähigkeiten ein entscheidender Aspekt des Systemdesigns. Das richtige Gleichgewicht zwischen den Radarerkennungsanforderungen und den Kommunikationsbedürfnissen ist von entscheidender Bedeutung, um nachteilige Auswirkungen auf die Radarperformance zu vermeiden. Daher wird ein konzeptionelles Radarsystem durch Signalverarbeitungstechniken und eine sorgfältige Systemauslegung vorgeschlagen, die eine konventionelle Radarer-

fassung und einen Datenaustausch ermöglichen. Zu diesem Zweck wird eine separate Architektur des Kommunikationsempfängers innerhalb des Radarentwurfs vorgeschlagen, um den Freiheitsgrad zu betonen, der für Radarmessungen mit seinem eigenständigen Empfänger gegeben ist, bei dem das Sendesignal für Radar- und Kommunikationsfunktionen von derselben Hardware in einer vordefinierten Zeitdauer erzeugt wird.

In diesem Zusammenhang beinhaltet die Arbeit zwei neuartige Kommunikationsverfahren und eine Synchronisationsmethode zwischen kommunizierenden Radarsensoren, um einen nahtlosen Datenaustausch zu ermöglichen. Ein kommunikationsbasierter Ansatz besteht darin, die Chirps teilweise mit Kommunikationssymbolen im oberen oder unteren Teil jedes Chirps zu modulieren, um die Auswirkungen auf das Radarsignal gering zu halten, wo die Modulation des gesamten Chirps die Detektionsqualität verschlechtert. Andererseits wird durch die Aufteilung jedes Chirps in zwei Segmente mit vorbestimmten Zeit-Frequenz-Verschiebungen, basierend auf dem LoRa (engl. *Long-Range Communication*), jeder Chirp als Kommunikationssymbol dargestellt. Es sollten jedoch zusätzliche Anpassungen für die Radarsignalverarbeitung vorgenommen werden, um die Verschiebungen innerhalb des Sendesignals zu kompensieren. Darüber hinaus wird ein innovativer Ansatz für die Synchronisation vorgeschlagen, der es den Kommunikationsknoten ermöglicht, ihre Sendeempfänger in der Zeit-/Frequenzebene neu zuzuordnen und den Übertragungsprozess zu initialisieren. Die vorgestellte Methode ist von bildähnlichen Verarbeitungstechniken abgeleitet, bei denen Kurzzeit-Fourier-Transformationen (STFTs) und lineare Regression eingesetzt werden, um eine 2D-Matrix der Signalpunkte in der Zeit-Frequenz-Ebene zu erzeugen. Außerdem werden fortschrittliche Mechanismen zur Erkennung von Interferenzen am Kommunikationsempfänger integriert, um die Auswirkungen von Interferenzen auf die Synchronisation zwischen den Knoten und die übertragenen Daten zu analysieren. In diesem Sinne kann entweder die vorgeschlagene Synchronisationsmethode erweitert und in das Multi-User-Szenario übernommen werden, oder es wird ein Matched-Filter-Ansatz entwickelt, wenn die Parameter der Signale bekannt sind. Darüber hinaus wird das vorgeschlagene System durch mehrere Messungen mit einem Demonstrator in den Labors des KIT im Bereich von 79 GHz validiert. Zu diesem Zweck wird ein System bestehend aus zwei subharmonischen Mischern, Verstärkern, Signalgeneratoren, Antennen und RFSoC in einem der Labore des KIT aufgebaut. Zusätzlich werden Simulationen mit Matlab durchgeführt, wobei ähnliche

Parameter wie bei der Messung verwendet werden, um das angenommene System zu analysieren.

Zusammenfassend lässt sich sagen, dass CS-basierte Radarsysteme mit Kommunikationsfähigkeiten eine innovative und umfassende Lösung zur Entschärfung von Interferenzen darstellen, denen Radarsensoren in gemeinsamen Umgebungen ausgesetzt sind. Durch die effektive Bewältigung des Interferenzproblems bei gleichzeitiger Erhaltung der Radarperformance wird ein System für Radarkommunikation basierend auf Chirpsequenzen (engl. *Communications-assisted Chirp Seqeucne*) entwickelt, das einen vielversprechenden Fortschritt in modernen Radarsystemen für überfüllte und dynamische Umgebungen darstellen kann.

Acknowledgement

At this significant point in my academic journey, I want to express my gratitude to the people who have been essential in facilitating this achievement. Without their help, it would not have been even possible.

I want to thank Prof. Dr.-Ing. Dr. h.c. Thomas Zwick allowed me to conduct my research work at the IHE for the last six years and has always been at my side with help and advice regarding any subject or question. Besides, I thank Prof. Dr.-Ing. Christian Waldschmidt for his helpful feedback and constructive comments, especially during the work on shared projects between KIT and Ulm University.

I am incredibly grateful to my colleague, Dr.-Ing. Benjamin Nuß, who has given me his time from day one to support me at every step of my research at IHE. I genuinely appreciate my colleague Lucas Giroto de Oliveira for all our days together at IHE and his enthusiasm for discussing technical and non-technical topics. Additionally, I would like to recognize my colleagues Dr.-Ing. Yueheng Li and Theresa Antes and my friend Thomas Haddad from the Department of Optoelectronics at the University of Duisburg-Essen for their time and feedback on my thesis. Working with Associate Professor Dr. Zsolt Kollár from the Budapest University of Technology and Economics has been a privilege during his visit to KIT.

Moreover, I want to convey my thanks to Christoph Winkler, Joel Dittmer, Jean-Pierre Messmer, and Till Hülder for participating in my research and all the discussions and investigations we have done together during their studies at IHE. I also acknowledge the partners involved in the IMIKO-Radar project for all our discussions on developing a seamless system for joint radar communication in the future. Furthermore, I would also like to thank the technical staff, especially Andreas Lipp, for supporting me with the ETIT workshop I supervised at KIT for a few years. I sincerely thank the secretaries, Marion Jentzsch, Simone Gorré,

and Angela Ziemba for their assistance in managing all the organizational issues regarding the projects, trips and courses I supervised at KIT.

I would also like to thank my Chinese-speaking colleagues, especially Dr.-Ing. Yueheng Li, Tsung-Ching Tsai, and Tai-Yu Kuo, with whom I enjoyed debating Chinese history and analyzing the story of its prosperous dynasties in which my imagination had no borders.

Finally, I thank all my close and extended family members for their love and support throughout my academic journey. They have been the source of my inspiration and strength for the past years.

Autumn 2024
Karlsruhe

Contents

Acronyms and Symbols

Lower Case Letters

a	Thresholding factor
b, o	Arbitrary points
c_0	Speed of light in vacuum ($2.997925 \cdot 10^8$ m/s)
d	Distance between points, symbols, antenna elements
f	Frequency
f_c	Carrier frequency
f_s	Sampling frequency
g	Reference signal
h^{com}	Channel vector
k_{Bl}	Boltzmann constant ($1.380649 \cdot 10^{-23}$ m^{2}kg/s^2/K)
s_m	Transmit communication symbol
s_q	Information signal in baseband
v	Velocity
w	Noise signal
x_q	transmit signal
y_q	receive signal
z_{IF}	IF radar signal

Capital Letters

A	Amplitude

AC	Correlation output
B	Signal bandwidth
$C_{cluster}$	Number of clusters
$\mathcal{CR}$	Cycle factor
$\mathcal{DR}$	Dynamic range
E	Energy
G, G_p	Gain factor, processing gain
H	Assigned threshold
K_{ric}	Rician K factor
L	Number of examined points or channels
$\mathcal{M}$	Modulation order
MC	Preamble energy
ME	Correlation metric
NF	Noise figure
N	Number of samples
N_0	Noise power spectral density ratio
N_i	Number of nodes
N_z	Number of range bins
P	Power
$\mathcal{P}$	Probability of error
P_{hop}	Hop size
PL_{com}	Path loss
P_N	Noise power
$\overline{P}_{RI}$	Average receive interference power
P_{th}	Number of trajectories in wireless channel
Q	Number of blocks in a sequence
Q_z	Number of Doppler bins
Υ_{norm}	Number of features in the normal equation
R	Range
$\mathcal{R}$	Data Rate

T	Time duration
T_p	Pause duration
T_s	Sampling time
T_{th}	Thermal temperature
U	Preamble length
Z_{tg}	Number of targets

Mathematical operators and indexes

General indexes

ant	Antenna, antenna elements, MIMO receive channels
b	Bit
com	Communication
cr	Correlation
e	Error
eff	Effective
f	Fine
fa	False alarm
frac	Fractional
in	Input
max	Maximum
min	Minimum
miss	Misalignment
mod	Modulation
rad	Radar
rc	Radar-Communication, RadCom
ref	Reference
Rx	Receiver
samp	Sample
snap	Snapshot
seq	Sequence
sync	Synchronization
symb	Symbol
tg	Target
Tx	Transmitter
um	Unmodulated

| unamb | Unambiguous |

Mathematical operators and indexes

$\lvert \cdot \rvert$	Absolute operator
$\overline{()}$	Mean operator
$(\hat{\ })$	Estimated value
$\arcsin(\cdot)$	Arcsin function
C_i	Index of correlation peaks
∂	Differential operator
Δ	Variation
$dist(\cdot)$	Distance operator
$E(\cdot)$	Estimation operator
$EPS(\cdot)$	Radius operator
$f(\mathrm{x};\theta)$	Maximum likelihood function
$\mathscr{F}, \mathscr{F}^{-1}$	Fourier transform and its inverse
$\gamma(\cdot)$	Threshold operator
$I_0(\cdot)$	Bessel operator
k	Frequency index
l	Point index
m	Symbol index
n	Sample index
$\mathcal{N}(\cdot)$	Distribution function
$O(\cdot)$	Big O notation
$P(\cdot)$	Probability operator
q	Chirp indexes
$Q(\cdot)$	Q function
$\mathrm{rect}(\cdot)$	Rectangular function
u	Windowing index

$\text{var}(\cdot)$	Variance
$w(\cdot)$	Windowing function
W_N^{kn}	Fourier operator
$W_N^{u\Lambda n^2}$	Chirp operator
x_l, y_l	Coordinate indexes
z_{tg}	Target index
ι, ν, o	Correlation substitutional variables
ξ	Segment index
$\wp$	Trajectory index

Greek and mathematical symbols

α	Attenuation factor
β	Channel index
$\Delta f_{\text{c}}^{\text{u}}, \Delta f_{\text{c}}^{\text{d}}$	Coarse up- and down-seeded frequency
Δf_{f}	Fine frequency shift
ΔR	Range resolution
Δt_{f}	Fine time shift
Δv	Velocity resolution
ϵ	Radius in DBSCAN
$c_{q_{\text{s}}}^{\gamma}$	Y-intercept
$D_{q_{\text{s}}}^{\gamma}$	Data set with $\{(x,y)_{q_{\text{s}}}^{\gamma}\}$ coordinates
$(\hat{X}, \hat{Y})_{q_{\text{s}}}^{\gamma}$	Estimated points in X-Y plane
$(\mathbf{Y}_{q_{\text{s}}})_{\xi,k}$	Receive signal after applying STFTs with thresholding
$(\mathbf{Y}_{\text{cr}})_{k,\nu}$	Receive signal after applying FQPT
ζ	Doppler variable
η	Range variable
θ_{tg}	Target angle

$\mathbf{I}(\theta)$	Fisher matrix
κ_{int}	Interference factor
λ	Wave length
Λ	Incremental step in chirp function
μ	Chirp rate
Ξ	Segment length in STFT
ρ	Correlation factor
ϱ	Arbitrary integer
σ_{awgn}	Standard deviation
σ_{tg}	Radar cross section
τ	Time delay
r_ς	Receive communication symbol
φ	Chirp phase
$\phi_{l_{\text{ant}}}$	Phase of the IF signal in MIMO scenarios
$\Delta\psi_{\text{m}}$	Phase correction factor
$\Delta\Phi(t)$	Phase different between transmit and receive signals

Acronyms

1D, 2D, 3D, 4D	One-, Two-, Three-, Four-dimensional
3GPP	3rd Generation Partnership Project
5G	Fifth Generation of Mobile Technologies
6G	Sixth Generation of Mobile Technologies
ADAS	Advanced Driver Assistance System
ADC	Analog to Digital Converter
AI	Artificial Intelligence
AOA	Angle of Arrival
APU	Application Processing Unit
AWGN	Additive White Gaussian Noise
BER	Bit Error Ratio
$CA - CFAR$	Cell-averaging CFAR
CaCS	Communication-assisted Chirp Sequence
CDF	Cumulative Distribution Function
CFAR	Constant False Alarm Rate
CFR	Channel Frequency Response
CI	Confidence Interval
CLB	Configurable Logic Block
CRB	Cramer-Rao Bound
CS	Chirp Sequence
CW	Continous Wave
DAC	Digital to Analog Converter
DBSCAN	Density-Based Spatial Clustering
DDR4	Double Data Rate Fourth SDRAM
DFT	Discrete Fourier Transform
DDS	Direct Digital Synthesizer
DOA	Direction of Arrival
DPPM	Differential Pulse Position Modulation

DR	Dynamic Range
DRFM	Digital Radio Frequency Memory
DSP	Digital Signal Processing
FDM	Frequency Division Multiplexing
FFT	Fast Fourier Transform
FLL	Frequency Locked Loop
FMCW	Frequency Modulated Continous Wave
FPGA	Field Programmable Gate Array
FQPT	Fast Quadratic Phase Transform
FT	Fourier Transform
FSK	Frequency-Shift Keying
GMSK	Gaussian Minimum Shift Keying
GNSS	Global Navigation Satellite System
GPS	Global Positioning System
HAD	Highly Automated Driving
HP	Highpass
IF	Intermediate Frequency
IHE	Institute of Radio Frequency Engineering and Electronics
I&Q	In-Phase and Quadrature
ISAC	Integrated Sensing and Communication
ISI	Intersymbol Interference
ISLR	Integrated Sidelobe Ratio
ISM	Industrial, Scientific and Medical Band
ITS	Intelligent Transportation System
ITU	International Telecommunication Union
KIT	Karlsruhe Institute of Technology
LFM	Linear Frequency Modulation
LMS	Least-mean Square
LNA	Low Noise Amplifier
LO	Local Oscillator

LoRa	Long Range Communication
LOS	Line of Sight
LP	Lowpass
LR	Linear Regression
LRR	Long Range Radar
MIMO	Multiple Input Multiple Output
mmWave	Millimetre Waves
MRR	Medium Range Radar
MSE	Mean Squared Error
OCDM	Orthogonal Chirp Division Multiplexing
OFDM	Orthogonal Frequency Division Multiplexing
OS − CFAR	Ordered Statistic-CFAR
OTFS	Orthogonal Time Frequency Space
PA	Power Amplifier
PD	Power Detection
PAM	Pulse Amplitude Modulation
PCF	Phase Correction Factor
PL	Programmable Logic
PLL	Phase Locked Loop
PM	Partial Chirp Modulation
PMCW	Phase Modulated Continuous Wave
PPM	Pulse Position Modulation
PR	Penetration Rate
PS	Processing System
PSD	Power Spectral Density
PSLR	Peak Sidelobe Ratio
PWM	Pulse Width Modulation
QPSK	Quadrature Phase Shift Keying
QuaDRiGa	QUAsi Deterministic RadIo channel GenerAtor
RadCom	Radar-Communication System

RCS	Radar Cross Section
RDM	Range Doppler Map
RF	Radio Frequency
RFSoC	RF System-on-Chip
RTS	Radar Target Simulator
RPU	Real-time Processing Unit
SCA	Schmidl and Cox Algorithm
SDR	Software Defined Radio
SER	Symbol Error Ratio
SF	Spreading Factor
SISO	Single Input Single Output
SMA	SubMiniature version A
SNR	Signal to Noise Ratio
SoC	System-on-Chip
SRD	Short Range Devices
SRR	Short Range Radar
STFT	Short-Time Fourier Transform
TDM	Time Division Multiplexing
TFSK	Time Frequency Shift Keying
Tx, Rx	Transmitter and Receiver
ULA	Uniform Linear Array
VANET	Vehicular Ad Hoc Network
V2I	Vehicle-to-Infrastructure
V2R	Vehicle-to-Roadside
V2V	Vehicle-to-Vehicle
V2X	Vehicle-to-Everything
VCO	Voltage Controlled Oscillator
WLAN	Wireless Local Area Network
ZF	Zero-forcing

1 Introduction

Since the invention of radar technology, radar sensors have been deployed in many aspects of our lives [Hü04]. Although the technology focused on military use [Rid46] at the beginning, the radar concept has been expanded to cover civil applications such as automotive scenarios [Cri57], [Ter64], [S+91] to support several functions, like parking systems and detecting objects [Mer64], [RL95], [WZ09]. This interest can be accredited to the low-cost requirements resulting from improvements in semiconductor manufacturing and the functionalities offered across various domains [CS92], [Bin92], [RL95], [WZ09]. Besides, machine learning and artificial intelligence (AI) can help radar technologies progress further in the future. This advancement enables the development of highly autonomous driving (HAD), which can significantly impact future transportation [Wil88]. However, advancing radar technologies is a social necessity, aiming to reduce CO2 emissions, conserve energy resources, and mitigate car accidents [CF20], [Wax08]. In this sense, the EU Commission has reported that more than 20,000 people perished in car accidents in EU countries in 2021 [Rob23]. Thus, active monitoring systems can minimize the impacts of accidents by facilitating vehicles to adopt HAD, which allows them to respond autonomously in different driving situations. Apart from that, the concept of autonomous driving extends beyond safety benefits. For instance, car-sharing initiatives can benefit from HAD systems by reducing private transport costs and allowing drivers to manage their time more efficiently [J+22]. Therefore, accurate environmental perception is essential, and numerous radar sensors can be integrated into vehicles for this purpose [D+21], [Chi23], [SZ21].

In automotive applications, radar sensors currently utilize frequency-modulated continuous wave (FMCW) or chirp sequence (CS) waveforms to detect various targets in the vicinity [RBK+19, HY19, WHM21], which is cost-effective and facilitates manufacturing compared to other waveforms proposed in the literature, such as orthogonal frequency-division multiplexing (OFDM) [SW11] and phase-modulated continuous-wave (PMCW) methods [G+17]. However,

the increasing number of automotive radars operating within the same frequency band $(76 - 81)$ GHz approved for such radars has resulted in interference between the transmitted signals. Therefore, numerous studies have explored various methods to mitigate interference among radars operating in the same environment, considering factors like temporal, spectral, and spatial separation of the interferers [ES01], [N+21]. Time-domain techniques, like clipping, have proven effective in reducing interference impact on radar systems by limiting the amplitude of strong interfering signals [Bro07]. However, clipping can influence the radar sensitivity in detecting weak targets since the threshold can exceed the desired level. Another approach for interference mitigation in CS-based radar systems involves randomly altering the structure of the chirp sequence in the time domain to decouple frequency ramps within the same time slot. On the other hand, in the frequency domain, frequency hopping has emerged as a prominent option for interference mitigation in automotive scenarios. This technique involves switching the frequency of radars between a predefined set of frequencies and can be implemented using methods like random frequency selection or frequency hopping based on a predetermined pattern [Kun12], [Bor22]. Additionally, compass methods that select frequencies according to the orientation of the sensors can help avoid direct line-of-sight (LOS) interference situations between the converging sensor [FGM+21]. Nevertheless, various approaches can be employed to mitigate interference events, including adapting coding schemes, detecting and repairing interference, and analyzing the time-frequency plane before measurements [Bor22].

An alternative and promising method to alleviate interference in automotive scenarios involves enhancing radar systems with communication capabilities to collaborate and prevent interference occurrences in the surroundings. Adhering to the above requirement, incorporating communication data allows the radar-centric systems to communicate effectively. This communication entails the exchange of crucial signal parameters (such as bandwidth, signal duration, and center frequency) to prevent any overlapping of radar signals in terms of time or frequency [Bor22], [KRM+16]. This thesis mainly focuses on this innovative concept for mitigating interference events alongside the previously mentioned techniques.

1.1   State of the Art

Since advanced anticipated services in the future entail a reallocation of the shared frequency spectrum, several studies have been exploring the benefits of integrating radar and communication systems. This innovative consolidation of both technologies highlights the exploitation of existing services in conjunction with the hardware, providing a potential framework for the eventual convergence in the realm of 6G networks [DL+21]. The concept of simultaneous sensing and communication features has been denoted by various names over the past decade, such as joint communication and sensing [WBV21] or integrated sensing and communication (ISAC) [L+17]. Most published studies on shared radar communication systems primarily focus on system-based models through a dedicated external system. One potential application for these systems is the utilization of HAD [WHM21], which assists vehicles in minimizing signal interference through a proper communication link. Noteworthy examples of this approach include vehicle-to-vehicle (V2V), vehicle-to-infrastructure (V2I), and vehicle-to-roadside (V2R) communication, which rely on separate communication links [IEE08, K+11, 3GP20]. In addition, intelligent transportation systems (ITS) and vehicular ad hoc networks (VANET) are significant candidates for V2V communication. In this regard, ITS and VANET involve adapting a distributed WLAN (IEEE802.11p) [IEE10] dedicated exclusively to providing communication capabilities in a dynamic vehicle environment [MX16, ETS12], [YMF06]. In this context, vehicle-to-everything (V2X) and ITS can thus achieve high data rates for various communication purposes independent of radar systems. In contrast, signal-based models adopt the communication data within the radar signals to eliminate the need for separate communication systems. This integration leads to the development of radar communication (RadCom) [GdO+21] systems that primarily support radar-centric systems for automotive applications. OFDM is a commonly adopted approach for such systems, as it offers convenient signal processing capabilities for both communication and radar sensing [SSZ+11, Bra14], [LMI16], [L+18]. Another promising alternative for RadCom systems is orthogonal chirp division multiplexing (OCDM) [GdOANZ20], [GNA+21], [OZ16], which differs from OFDM by modulating orthogonal sub-chirps instead of subcarriers. Furthermore, researchers have explored the integration of radar and communication with orthogonal time-frequency space (OTFS) [GKCC20]. These systems are primarily derived from communication systems and have been extended to meet

3

Table 1.1: Comparison of Radar-Communication Systems for Automotive Applications.

System-based		
Type	V2X-based 4G/5G	ITS based 5.9 GHz
Standard	3GPP	IEEE 802.11p
Development	Mature	Mature
Range	$\geq 1\,\mathrm{km}$	$\leq 1\,\mathrm{km}$
Hardware	4G/5G	Separate
Cost	Separate system	Separate system

(a)

Signal-based			
Type	Digital (79 GHz)	5G/6G	Analog (79 GHz)
Standard	No	No	No
Development	Research	Research	Research
Range	$\leq 1\,\mathrm{km}$	$\leq 1\,\mathrm{km}$	$\leq 1\,\mathrm{km}$
Hardware	Radar-based	Com-based	Radar-based
Cost	High	Separate	Low

(b)

the requirements of target detections. In this context, the signal for the shared spectrum is digitally generated and possesses a predetermined bandwidth that aligns with the desired range resolution for the specific application.

Alternatively, FMCW and PMCW signals are vital candidates for radar-centric systems that can integrate communication data for specific purposes. In FM-CW and PMCW, the signal can be modulated with conventional modulation schemes to achieve integration of communication data into the system [BEJ07], [SFHS15]. Furthermore, a detailed comparison in Table 1.1 highlights key performance metrics, such as communication distance between the nodes, communication latency, and the hardware integrated into the system. The aforementioned metrics have been performed for two different concepts, system-based (a) and signal-based (b), as described in detail in the upcoming chapters. Apart

from that, since most current radar systems adopt FMCW or CS waveforms, the presented thesis has focused on integrating communication data into CS-based radar systems and analyzed the limitations caused by this integration.

1.2 Structure and Objectives of the Work

CS-based waveforms with integrated communication data can be a promising solution to support radar sensors and avoid interference events in the surroundings [BEJ07], [DZB+20], [DBSF19], [FJ15b], [FJ15a], [LTAW19]. This approach is especially relevant considering the need for fast analog-to-digital converters (ADCs) in digital waveforms such as OFDM and OCDM. In this sense, the communication link between vehicles through CS waveforms can provide an appropriate data rate for specific communication purposes (e.g., mitigate mutual interference and avoid interference). Additionally, CS waveforms are economically feasible for automotive radar systems, and the required components are inexpensive [TI20]. In CS-based systems, communication data is integrated into radar systems by assigning specific communication symbols to each chirp. However, fully modulating the entire chirp with communication data can affect the radar functionality. Hence, the main goal of this thesis is to investigate the employment of CS-based communication systems to minimize interference among radar sensors in their vicinity and assess the influence of such communication on the accuracy of radar detection [K+21b], [KRM+16], [PBF20].

The thesis is divided into four sections, as illustrated in Fig. 1.1. The first part focuses on the transceiver architecture of CS-based radar systems and introduces the radar signal processing chain and several hardware components used in the measurement campaign. The second part discusses novel communication techniques based on CS-based radar systems, which differ from traditional methods investigated in the literature. These new techniques involve innovative concepts of a separate narrowband communication receiver to demodulate the assigned communication data without disrupting the radar reception cycle. This can limit the sampling rate of the ADC in radar-centric systems so that the extension with communication data in radar systems remains economically feasible. Chapter 3 of the thesis proposes two innovative communication techniques. On the one hand, the first technique assigns only a section of each chirp to communication symbols (partial modulation), minimizing the impact

5
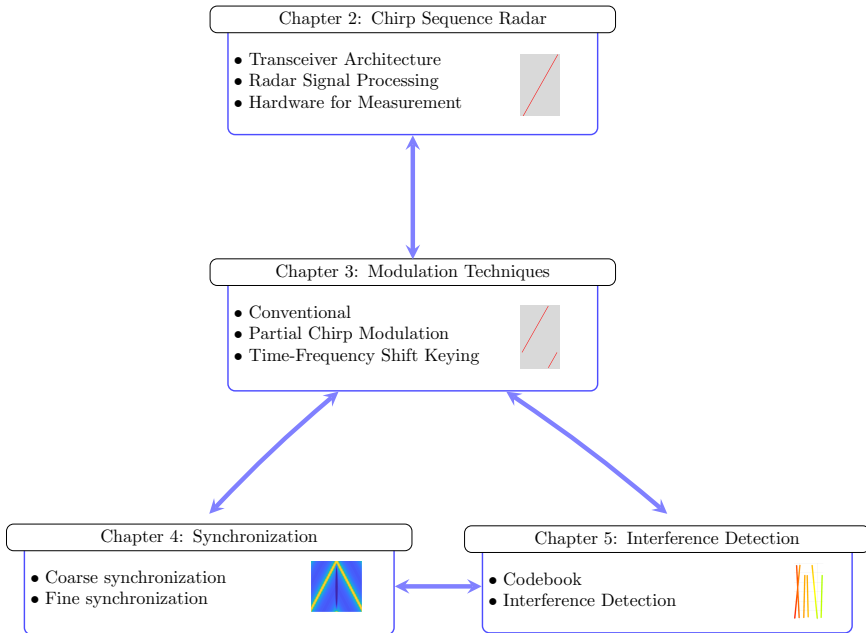
Fig. 1.1: Structure of the thesis and its objectives divided into the respective chapters.

on radar quality. On the other hand, the second method, Time-Frequency Shift Keying (TFSK), adjusts the structure of each chirp in the time-frequency plane and transmits one communication symbol per chirp based on long-range communication (LoRa). Besides, the conventional 2D-FFT required for radar signal processing is adjusted to accurately estimate the range and velocity of investigated objects in the surroundings. The thesis also includes MATLAB simulations and measurement campaigns to analyze the proposed concept and explore the effects of wireless channels on the investigated communication techniques. In Chapter 4, the study presents a novel approach for synchronization between two radar sensors that communicate employing CS-based radar systems. The proposed scheme, known as "Preamble-based Synchronization for Communication-assisted Chirp Sequence Radar", introduces a chirp-like synchronization method with coarse and fine stages [A+22b]. In the first stage, time synchronization is achieved using a sliding preamble consisting of up- and

down-chirps and time-frequency analyses of the preamble within a narrowband signal. These time-frequency analyses involve short Fourier transforms (STFT) and linear regression (LR) [Gar16] to provide rough estimates of the time and frequency deviations between the transmitter and receiver nodes. The second synchronization step addresses any remaining time and frequency variations caused by residual linear regression errors. Moreover, Chapter 5 presents a proposed method for detecting interference between radar sensors. This method can represent the pattern of each signal transmitted. However, the complexity of the approach may increase depending on the number of detected lines, as it relies on creating STFT transforms and linear regression lines. Alternatively, a correlation-based approach using a prearranged codebook can identify the desired signal amidst the interference caused by the interferer.

Throughout the investigation, appropriate hardware components suitable for a demonstrator operating at a frequency of 79 GHz were chosen. A measurement campaign was conducted with a demonstrator to compare its actual measured performance with the theoretical and simulated performance [FME18]. The results of the measurement campaign have confirmed the effectiveness of the proposed communication and synchronization methods. Besides, the achieved performance in the measurements meets the requirements for radar functionalities and provides a satisfactory data rate for vehicle communication.

In Fig. 1.2, a sketch representing an example of the investigated scenario is illustrated. Four nodes are adopted for the ease of simplicity. Each node comprises a configuration to facilitate radar and communication features. N_1 emerges as a vital example of a radar-centric system with communication abilities that involves an active radar alongside a separate communication receiver in engagement with other nodes, such as N_2. Besides, N_2, equipped with its dedicated communication receiver, operates to detect the targets in the surroundings by its radar transceiver chain and capture the signal from N_1 to extract the information sent from N_1 and enable data exchange for their signal properties and traffic status. Furthermore, N_3 and N_4 are characterized by their active radar transceivers, which detect targets in the environment. However, their signals can simultaneously be a source of interference aimed at N_2. In this context, the radar transceiver, including communication adjustments, operates based on CS-based radar architecture and encompasses essential components such as a chirp generator, amplifiers, a mixer, a phase modulator, and antennas, as depicted in Fig. 1.3(a). The chirp generator generates linear frequency-modulated (LFM)

7
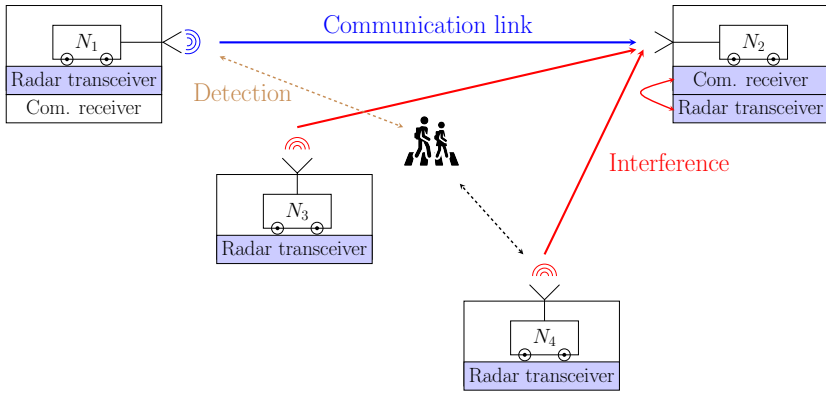
Fig. 1.2: Exemplary scenario in automotive applications. N_1 represents the node responsible for radar and communication transmission. N_2 is the node where the valuation of communication data takes place. N_3 and N_4 illustrate a possible interference events aimed at N_2. The blue line represents communication transmission, while the black and green counterparts represent the detection in the surroundings. Red lines illustrate possible interference events. This unique design represents, for the first time, a communication-assisted chirp sequence (CaCS) innovative concept [A+22b] to facilitate communication between vehicles through their employed radar sensors while preserving detection quality.

waveforms, while the mixer combines these waveforms with the received counterparts for target detection. The phase modulator $\Delta\Phi$ facilitates dynamic phase adjustment based on modulator control, enabling seamless integration of radar sensing and communication functionalities. On the other hand, the communication receiver is designed separately to grant greater degrees of freedom within the design between radar and communication functionalities. For this purpose, a direct downconverter approach is employed. This approach includes diverse components such as a low-noise amplifier (LNA), a mixer, a local oscillator (LO), and a DSP unit. Besides, a correlation approach within the DSP unit is performed to extract modulated data from received signals, enabling efficient demodulation and subsequent processing, as illustrated in Fig. 1.3(b).

The upcoming chapters analyze the aforementioned diagrams in detail to clarify the novel idea of the proposed concept, where a CaCS-based radar system is represented [A+22b], to particularly facilitate communication between vehicles through their employed radar sensors while preserving detection quality.
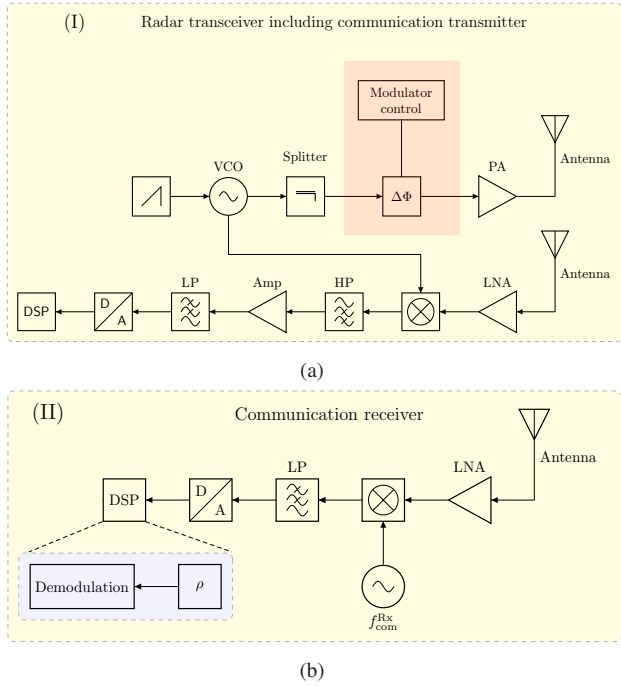
Fig. 1.3: Block diagram of CaCS nodes in automotive scenarios. (a) Radar transceiver including communication transmitter at N_1, including a voltage-controlled oscillator (VCO), a splitter, a phase modulator $\Delta\Phi$, amplifiers, filters, an ADC, and a digital processing unit (DSP). (b) Communication receiver at N_2, including an LO, an amplifier, a filter, an ADC, and a DSP for demodulation.

2 Principles of Chirp Sequence Radar and Measurement Setup

This chapter divides the primary investigation into parts for CS-based radar systems. It intends to familiarize readers with the CS-based waveform for identifying targets in the surroundings. Besides, the chapter presents a fundamental basis for advancing CaCS-based radar systems, which will be explored further through the investigation.

In this context, the chapter presents an overview of the signal model for the CS-based waveform based on the conventional block diagram of the transceiver. Subsequently, it offers a general description of the radar channel in automotive applications. Additionally, the chapter examines the range-Doppler map (RDM) and its role in visualizing detected targets in the surrounding area dependent on the maximum achievable parameters in terms of range and velocity. Finally, it briefly explains the calibration in radar systems and extends the study to cover MIMO schemes and the measurement setup employed throughout the investigation for SISO systems.

2.1 Chirp Sequence in Automotive Applications

CS-based radar systems have been adopted in wide applications for sensing and imaging tasks [S+23], [Win07] [KR14]. In contrast to radar systems that transmit continuous waveforms (CW) for velocity detection, a CS-based radar system sends a series of short frequency modulated waves, known as a chirp signal [RK14], dedicated respectively, to range and velocity detection in advanced driver assistance systems (ADAS) [MMMK12], [M+20]. One reason for adopting CS-based radar systems is the considerably low cost of the components required for further operations within the transceiver chain. Another reason is its simplicity and ease of implementation of the radar signal proces-
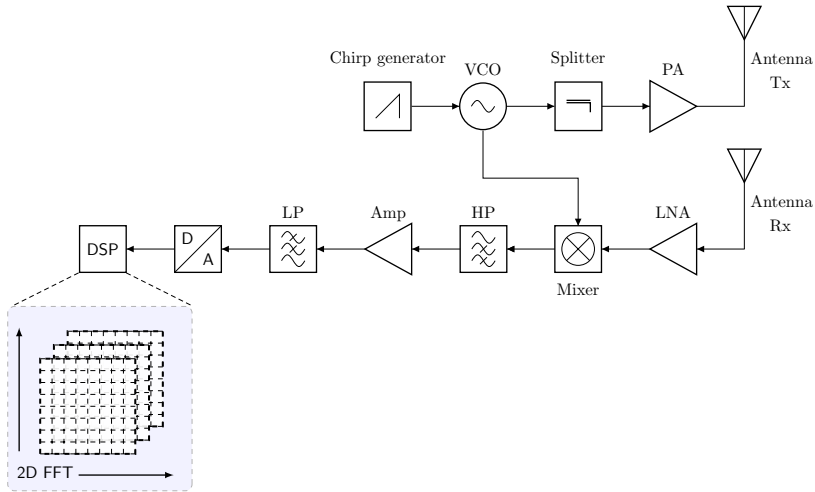
Fig. 2.1: Block diagram of a CS-based radar system

sing chain in the digital domain since CS-based radar systems sample a limited signal bandwidth after the downconversion and use a relatively known signal processing algorithm based on discrete Fourier transform (DFT).

2.2   Block Diagram and Signal Model

In this section, the block diagram of CS-based radar systems is introduced, and the signal model for the transmitter and receiver is performed and derived.

2.2.1   Block Diagram

A CS-based radar system involves several components to generate an LFM waveform based on a VCO, optionally coupled with an enhanced phase-locked loop (PLL), as shown in Fig. 2.1. After that, the signal is split and amplified by a power amplifier (PA) and transmitted further to the medium. Since the transmitter and receiver are located within the same radar system, the receiver
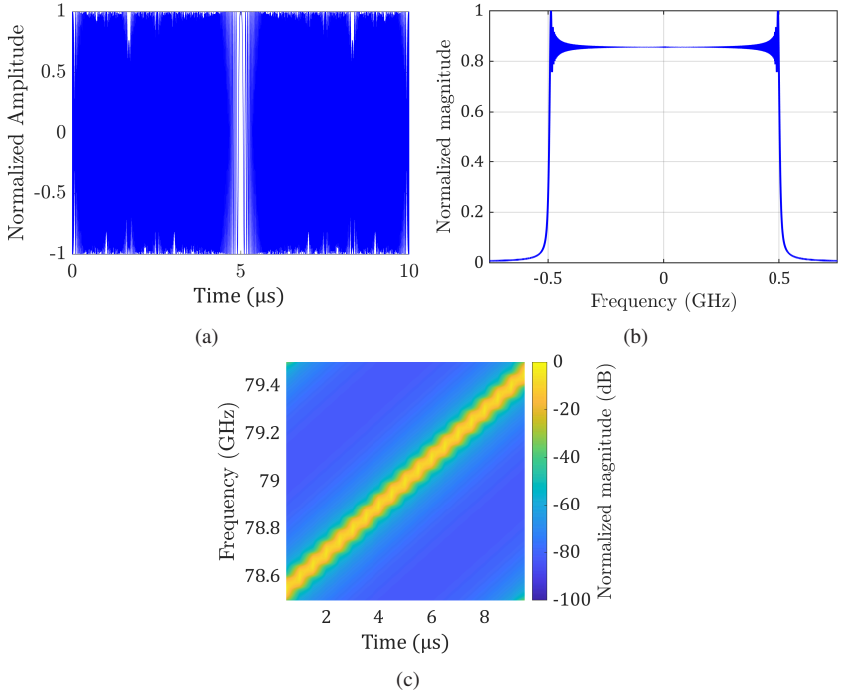
Fig. 2.2: Visualization of one chirp: $T_{\text{chirp}} = 10\,\mu\text{s}$, $f_{\text{c}} = 79\,\text{GHz}$, and $B = 1\,\text{GHz}$. (a) The representation of the signal in the time domain. (b) The representation of the signal in the frequency domain (baseband). (c) Spectrogram of the signal using STFT in the time-frequency plane.

collects the electromagnetic wave reflected by the target and mixes it with the transmit counterpart through the mixer to obtain the downmixed signal based on the desired intermediate frequency (IF). Moreover, the IF signal undergoes high-pass (HP) filtering to eliminate the echoes from the near-range cells and is amplified afterward by an LNA and filtered by a low-pass (LP) filter to limit the required sampling used in the digital domain for further signal-processing steps. The ADC converts the baseband signal and samples it at a predetermined rate and bit resolution. In this context, the DSP unit processes the digitized signal and performs algorithms for signal processing, such as fast Fourier transform (FFT) and signal detection.

Fig. 2.2 depicts a chirp signal whose frequency varies linearly with time, where the representation of the chirp in the time domain can be illustrated in Fig. 2.2(a). Besides, the formation of the chirp in the frequency domain can be derived by applying Fourier transform (FT) to the signal in the baseband, as shown in Fig. 2.2(b), where the depiction contains multiple frequency components based on the spanned bandwidth. According to both time and frequency domains, the chirp can be visualized in the time-frequency plane by taking STFTs based on an adjusted window and is called the spectrogram, as depicted in Fig. 2.2(c). The spectrogram of a chirp has a linear shape (/) that reflects the linearly increasing (or decreasing) frequency of the examined signal over time. If T_{chirp} is short enough, the IF signal encloses negative frequencies [KR14]. Therefore, In-phase and quadrature (I/Q) receivers are not required. However, if the I/Q structure is adopted at the receiver side, Fig. 2.1 should be extended by an additional channel.

2.2.2 Signal Model

In the time domain, the continuous signal $x_q(t)$ transmitted for enabling radar properties can be characterized as

$$
x_q(t) = \begin{cases} A \cos\left(\pi\mu\left(t - qT_{\text{RRI}}\right)^2 + 2\pi\left(f_{\text{c}} - \frac{B}{2}\right)t + \varphi_0\right), \\ t \in [qT_{\text{RRI}}, qT_{\text{RRI}} + T_{\text{chirp}}) \\ \\ 0, \quad t \in [qT_{\text{RRI}} + T_{\text{chirp}}, (q+1)T_{\text{RRI}}) \end{cases}
\tag{2.1}
$$

where q represents each chirp within the transmitted sequence, which is expressed for $t \in [qT_{\text{RRI}}, (q+1)T_{\text{RRI}})$, A denotes the amplitude of the transmit signal, $\mu = B/T_{\text{chirp}}$ is the chirp rate, f_{c} is the center frequency. B presents the signal bandwidth, φ_0 is the initial phase of the investigated signal. A sequence of multiple chirps Q with index $q \in \{0, 1, \ldots, Q-1\}$ combined with short spacing is designed to estimate the RDM of different objects in automotive scenarios. At the receiver of the CS-based radar system, the signal $y_q(t) \in \mathbb{R}$, which contains the output version of $x_q(t) \in \mathbb{R}$ by the channel, and additive noise, which is captured by the receive antenna.
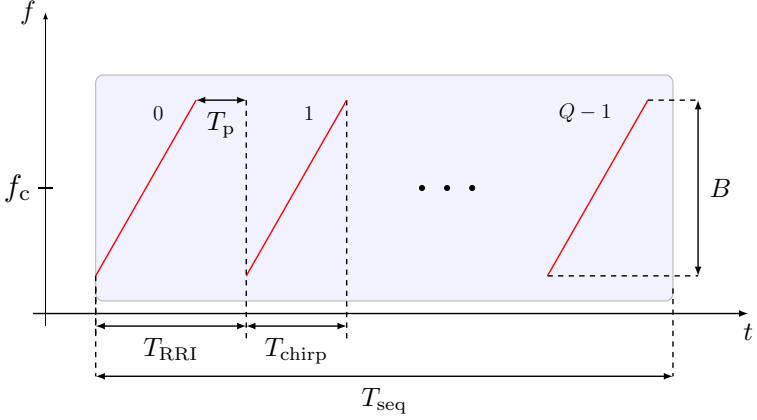
Fig. 2.3: CS-based waveform representation with the measurement duration T_{seq}. Q is the number of chirps with a time duration of T_{RRI} that encompasses a chirp with time duration T_{chirp} and a pause interval T_{P}, and it spans over bandwidth B [GdO+21].

2.2.3 Radar Channel

The radar channel in CS-based radar systems refers to all the trajectories $P_{\text{th}}^{\text{rad}} \in \mathbb{N}_+$ launched by the transmitter and follows with power $P_{\text{Tx}} \in \mathbb{R}_+$ from the transmit antenna to the targets $Z_{\text{tg}} \in \mathbb{N}_+$ and back to the receiver with an index $z_{\text{tg}} \in \{0, 1, \ldots, Z_{\text{tg}} - 1\}$ [GdO+21]. In this term, the channel includes all the imperfections caused by the environment, such as various propagation effects comprised of attenuation $\alpha_{z_{\text{tg}}}$, delay τ_{tg}, and phase shift associated with f_{tg}^{D}. All the aforementioned effects can distort the signal and affect the radar measurements. When the transmitted signal is sent through the radar channel, it can be reflected from several environmental objects. If the reflections created by the targets pass a certain threshold, the radar receiver can detect them as echoes further. In this framework, the received signal $y_q(t)$ can be expressed as

$$y_q(t) \approx \sum_{z_{\text{tg}}=0}^{Z_{\text{tg}}-1} \alpha_{z_{\text{tg}}} x_q(t - \tau_{\text{tg}}) e^{\text{j}2\pi f_{\text{tg}}^{\text{D}} t} + w(t), \tag{2.2}$$

15

where $w(t)$ represents the noise. One common approach to describe the effects of the channel on the signal is to use the radar equation, which relates the received signal power to the transmit counterpart, the distance to the target, and various factors that account for the properties of the radar channel and can be expressed as

$$P_{\mathrm{Rx}} = \frac{P_{\mathrm{Tx}} G_{\mathrm{Tx}} G_{\mathrm{Rx}} \sigma_{\mathrm{tg}} \lambda^2}{(4\pi)^3 R_{\mathrm{tg}}^4}, \tag{2.3}$$

where P_{Rx} is the received power, P_{Tx} is the transmit power, G_{Tx} and G_{Rx} are the antenna gains, $\lambda = c_0/f_{\mathrm{c}}$ is the wavelength of the transmit signal, σ_{tg} is the radar cross-section of the target, and R_{tg} is the distance to the target. In this term, the attenuation can be described as

$$\alpha_{z_{\mathrm{tg}}} = \sqrt{\frac{G_{\mathrm{Tx}} G_{\mathrm{Rx}} \sigma_{\mathrm{tg}} \lambda^2}{(4\pi)^3 R_{\mathrm{tg}}^4}}. \tag{2.4}$$

In addition to the attenuation, the range is connected with the delay assigned to (2.4) as $R_{\mathrm{tg}} = c_0 \tau_{\mathrm{tg}}/2$, while the Doppler shift caused by the motion of the target is associated with its velocity $v_{\mathrm{tg}} = \lambda f_{\mathrm{tg}}^{\mathrm{D}}/2$ and the radar cross-section of the target.

2.3 Radar Signal Processing

According to the influence of delay of one target, a shift in the time domain τ_{tg} is implied within the received signal [Win09]. Given one chirp signal at once, the occurred delay can be expressed as

$$\tau_{\mathrm{tg}} = \frac{2(R_{\mathrm{tg}} + v_{\mathrm{tg}} t)}{c_0}, \tag{2.5}$$

where R_{tg} is the distance of the target, v_{tg} its velocity and c_0 is the speed of light. Besides, the received signal reflected from the target in the vicinity can be introduced as

$$y_q(t) = A \cos\left(\pi\mu\left(t - \tau_{tg}\right)^2 + 2\pi\left(f_c - \frac{B}{2}\right)(t - \tau_{tg}) + \varphi_0\right) + w(t), \qquad (2.6)$$

where $w(t)$ is neglected from upcoming equations for simplicity. Since CS-based radar systems adopt a downconversion by the mixer at the receiver side, the intermediate signal can be given as

$$z_q^{IF}(t) = A \cos\left(2\pi\mu t\tau_{tg} + 2\pi\left(f_c - \frac{B}{2}\right)\tau_{tg} - \pi\mu\tau_{tg}^2\right), \qquad (2.7)$$

where the last term in the last equation can be neglected since CS-based radar systems generate very low range-Doppler coupling. Replacing τ_{tg} with its value in (2.4), the phase of (2.6) can be represented as

$$\Delta\Phi(t) = 2\pi\left(\frac{2f_c R_{tg}}{c_0} + \left(\frac{2f_c v_{tg}}{c_0} + \frac{2BR_{tg}}{T_{chirp}c_0}\right)t\right), \qquad (2.8)$$

where

$$f_{IF} = \frac{2f_c v_{tg}}{c_0} + \frac{2BR_{tg}}{T_{chirp}c_0}, \qquad (2.9)$$

is the IF frequency dependent on the occurred delay. The first term is related to Doppler, and the second points out the beat frequency (f_{beat}) connected with the examined range. However, since the first term (range of kHz) in the last equation can be neglected compared with the second counterpart (range of MHz), an assessment of the velocity only with one chirp cannot be accomplished. Therefore, a sequence of multiple chirps is sent to estimate both the range

and Doppler of the targets within the investigated scenario. In this context, the complex baseband signal can be written as

$$
z_{\text{IF}}(t) = \sum_{q=0}^{Q-1} e^{j2\pi \cdot \left[\frac{2f_c(R_{\text{tg}}+v_{\text{tg}}T_{\text{RRI}}q)}{c_0} + \left(\frac{2f_c v_{\text{tg}}}{c_0} + \frac{2B(R_{\text{tg}}+v_{\text{tg}}T_{\text{RRI}}q)}{T_{\text{chirp}}c_0} \right) t \right]}
$$
$$
\cdot \text{rect}\left(\frac{t - qT_{\text{RRI}}}{T_{\text{RRI}}} \right). \tag{2.10}
$$

Since the movement during one chirp can be neglected, the increment of the frequency connected with the range associated with the last term can be eliminated.

$$
z_{\text{IF}}(t) = e^{j4\pi f_c R_{\text{tg}}/c_0} \sum_{q=0}^{Q-1} e^{j2\pi \cdot \left[\frac{2f_c v_{\text{tg}} T_{\text{RRI}}q}{c_0} + \left(\frac{2f_c v_{\text{tg}}}{c_0} + \frac{2BR_{\text{tg}}}{T_{\text{chirp}}c_0} \right) t \right]}
$$
$$
\cdot \text{rect}\left(\frac{t - qT_{\text{RRI}}}{T_{\text{RRI}}} \right). \tag{2.11}
$$

Considering a sampling frequency f_s with sampling duration T_s, the aforementioned signal can be sampled and undergoes 2D-FFT to extract the range and Doppler information according to

$$
z_{\text{2D}}^{\text{IF}}(\zeta, \eta) = e^{j4\pi f_c R_{\text{tg}}/c_0} \sum_{q=0}^{Q-1} \sum_{n=0}^{N-1} e^{j4\pi \left(\frac{f_c v_{\text{tg}} T_{\text{RRI}}}{c_0} \right) q} e^{j2\pi \cdot \left[\left(\frac{2f_c v_{\text{tg}}}{c_0} + \frac{2BR_{\text{tg}}}{T_{\text{chirp}}c_0} \right) \cdot n \cdot T_s \right]}
$$
$$
\cdot e^{-j2\pi \left(\frac{q\eta}{Q_z} + \frac{n\zeta}{N_z} \right)}. \tag{2.12}
$$
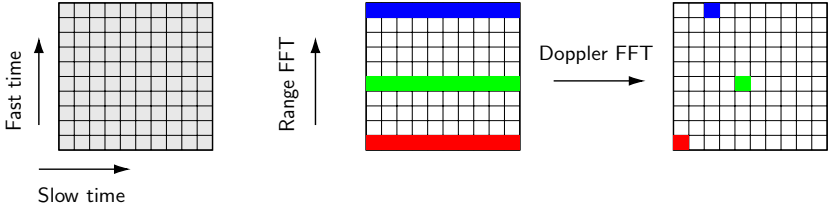
Fig. 2.4: Visualization of the 2D matrix to generate range-Doppler profiles based on the examined targets in the surroundings.

After separating the terms related to the range and Doppler, the aforementioned equation can be expressed as

$$
z_{2D}^{IF}(\zeta, \eta) = e^{j4\pi f_c R_{tg}/c_0} \sum_{q=0}^{Q-1} e^{j4\pi\left(\frac{f_c v_{tg} T_{RRI}}{c_0} q\right)} \left[\sum_{n=0}^{N-1} e^{j2\pi\cdot\left[\left(\frac{2f_c v_{tg}}{c_0} + \frac{2BR_{tg}}{T_{chirp}c_0}\right)\cdot n\cdot T_s - \frac{n\zeta}{N_z}\right]} \right]
$$
$$
\cdot\ e^{-j2\pi\left(\frac{qn}{Q_z}\right)}.
$$

(2.13)

According to the equation above, the desired information can be solved by

$$
\eta = \left(\frac{2f_c v_{tg}}{c_0} + \frac{2BR_{tg}}{T_{chirp}c_0}\right) T_s N_z,
$$

(2.14)

$$
\zeta = \left(\frac{2f_c v_{tg} T_{RRI} Q}{c_0}\right) = f_{tg}^D T_{RRI} Q_z.
$$

(2.15)

Fig. 2.4 depicts the 2D matrix in terms of the range-Doppler profiles based on the investigated targets. A 2D-FFT is employed to extract range and Doppler information, where the first FFT is applied column-wise for each chirp and the second counterpart row-wise among all the examined chirps to detect the change in Doppler.

2.3.1 Limitations of CS-based Radar

Range Resolution

By range resolution, radar systems can differentiate between two targets and classify them into two range cells based on the signal processing chain. In other words, range resolution represents the minimum distance between two detected targets that the radar can resolve as two different targets. Based on (2.15), the beat frequency resolution depends on $1/T_{\text{chirp}}$. Therefore, the range resolution can be represented as

$$\Delta R = \frac{c_0}{2B}, \tag{2.16}$$

According to this equation and based on (2.15), the unambiguous range can be derived from

$$R_{\text{unamb}}^{\text{max}} = \frac{c_0 T_{\text{chirp}}}{2B} f_{\text{beat}}^{\text{max}}, \tag{2.17}$$

where $R_{\text{unamb}}^{\text{max}}$ is the maximum distance that can be measured by the radar without ambiguity in range estimation, as it relates to the attained maximum beat frequency $f_{\text{beat}}^{\text{max}}$.

Velocity Resolution

Velocity resolution enables the radar system to differentiate between two detected targets in the environment based on the signal processing chain. In other words, velocity resolution represents the minimum velocity between two detected targets that the radar can resolve. Based on (2.15), the resolution of the beat frequency depends on $1/T_{\text{chirp}}$. Therefore, the velocity resolution can be expressed as

$$\Delta v = \frac{c_0}{2 f_c Q T_{\text{RRI}}}. \tag{2.18}$$

According to this equation and based on (2.15), the unambiguous velocity can be derived from

$$v_{\text{unamb}}^{\text{max}} = \frac{c_0}{4 f_{\text{c}} T_{\text{RRI}}}, \tag{2.19}$$

where $v_{\text{unamb}}^{\text{max}}$ is the maximum velocity that can be measured by the radar without ambiguity in velocity estimation.

2.3.2 Windowing

Windowing is an essential technique employed by signal processing approaches in several applications. In radar systems, windowing can improve the range and Doppler profiles based on suppression of the sidelobes [E+16]. Sidelobes are undesirable considerable peaks that can appear vicinal to the main lobe in the investigated profile due to various factors. An example of windowing is the Hamming window adopted throughout the thesis. Applying the windowing to the desired signal after downconversion reduces the amplitude of the sidelobes in the investigated profile. Nevertheless, windowing can also induce the broadening of the main lobe, as a significant drawback. If a windowing function is adopted, the main lobe is broadened, which lowers the ability to locate nearby targets in the range and Doppler domains. Besides, signal loss is another potential disadvantage of windowing, whereby a fraction of signal energy is inevitably lost. In general, the adoption of windowing can deteriorate the overall signal-to-noise ratio (SNR) and sophisticate the detection of weak targets. Therefore, a trade-off between the sidelobes suppression and enlarging the main lobe of the detected peaks is desired. In this work, including this section and upcoming chapters, a Hamming window function is chosen to provide better quality for range and Doppler profiles, as shown in Fig. 2.5. Fig. 2.5(a) depicts an exemplary scenario for automotive applications, where the radar node (object in blue) tries to detect the targets in the surroundings. Besides, the range profile of one detected target is presented in Fig. 2.5(b), and its corresponding radar image is visualized in Fig. 2.5(c). For the examined target at $\{R_{\text{tg}} = 44\,\text{m}, v_{\text{tg}} = 88\,\text{m/s}\}$, the two sub-figures above are shown without windowing, where the level of the sidelobes is high. On the other hand, Fig. 2.5(d) and Fig. 2.5(e) illustrate the range-Doppler profile and the radar image for the same target, but after applying

(a)

(b)

(c)

(d)

(e)
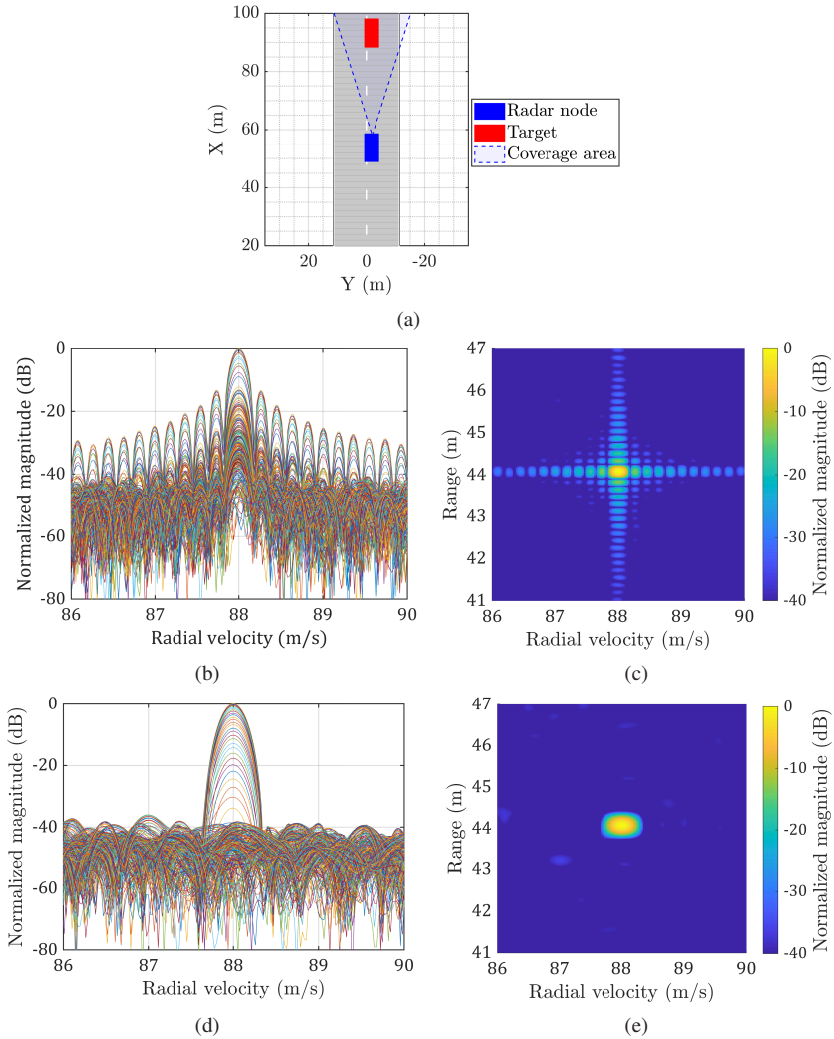
Fig. 2.5: Visualization of the investigated scenario and the radar image of a target $\{R_{tg} = 44\,\text{m}, v_{tg} = 88\,\text{m/s}\}$. (a) Exemplary sketch of the scenario. (b) Range-Doppler profile without windowing. (c) RDM for a target detected by CS-based radar without windowing. (d) Range-Doppler profile with Hamming window. (e) RDM for CS-based radar with Hamming window.

Hamming window to decrease the level of the attained sidelobes. However, in this case, the peak associated with the target is enlarged.

2.4 Impediments of Application in Real Systems

2.4.1 Nonlinear Frequency Ramps

Since CS-based radar systems employ LFM signals to detect objects in the surroundings, the signal nonlinearity impacts the estimation process of the target quantities. Consequently, it impairs the accuracy and precision of the radar measurements. Nonlinear frequency effects in CS-based radar systems can be caused by various sources, mainly the nonlinear behavior of the deployed components, such as the VCO. These nonlinearities can cause the transmit signal to deviate from its ideal linear frequency modulation and introduce distortion in the received signal if this grade exceeds a considerable limit. The effects of the nonlinearities can mainly impact the range resolution and SNR_{rad} level for radar. One example highlights the nonlinear behavior of frequency ramps in CS-based radar systems to define a periodic frequency shift within the transmit signal expressed as [Ayh16]

$$f_{\text{int}}(t) = (f_{\text{c}} - B/2) + \mu/2t + e(t), \tag{2.20}$$

where $f_{\text{int}}(t)$ represents the instantaneous frequency and $e(t) = A_{\text{e}} \cos(2\pi f_{\text{e}}t)$ is the error expressing the nonlinear effect within the chirp signal with frequency shift f_{e} and amplitude A_{e}, respectively. For a normalized A_{e} and $f_{\text{e}} = 150\,\text{kHz}$, Fig. 2.6 illustrates the effects of the frequency shift on the signal in the time-frequency plane and on the detection in the RDM after the downconversion. As shown in Fig. 2.6(a), the chirp signal occupies nonlinear components and undergoes periodic effects over the examined bandwidth. Those effects appear as a change in the intermediate frequency f_{beat} after downconversion and applying FFT, leading to ambiguity with range estimation caused by detecting multiple frequency components for each target, as depicted in Fig. 2.6(b). In this context, the uncertainty proportionally increases with the frequency shift.

Another common approach for describing the nonlinear frequency ramps is the quadratic component that might distort the linear sweep desired for radar
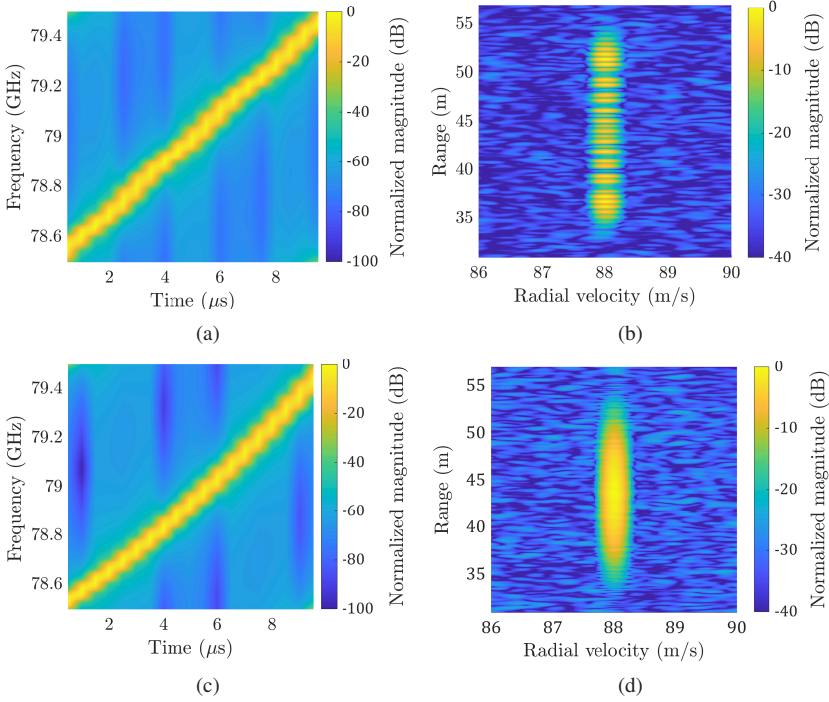
Fig. 2.6: Visualization of the effects of nonlinear frequency ramps in the time-frequency plane and in the radar image. $T_{\text{chirp}} = 10\,\mu\text{s}$, $f_{\text{c}} = 79\,\text{GHz}$, and $B = 1\,\text{GHz}$. (a) The representation of the signal in the time-frequency plane with periodic frequency shift. (b) RDM for conventional CS-based radar with nonlinear effects caused by a periodic sine signal for a target $\{R_{\text{tg}} = 44\,\text{m}, v_{\text{tg}} = 88\,\text{m/s}\}$. (c) The representation of the signal in the time-frequency plane with quadrature frequency shift. (d) RDM for conventional CS-based radar with nonlinear effects caused by a quadrature frequency shift for the same examined target as in (b).

applications. Adopting the same discussion in [Ayh16], the nonlinearity caused by a quadratic element of the chirp can be modeled as follows

$$f_{\text{int}}(t) = (f_{\text{c}} - B/2) + \mu/2t + e(t), \tag{2.21}$$

where $e(t) = 2\pi(4A_{\text{e}}/(T_{\text{chirp}}^2)t^2 - 4A_{\text{e}}/(T_{\text{chirp}})t)$ is the error expressing the nonlinear effect within the chirp signal with amplitude A_{e} that causes more dis-

tortion with higher values. The chirp signal in Figure 2.6(c) exhibits quadrature phenomena across the analyzed frequency range. These phenomena manifest as a modification in the intermediate frequency (f_{beat}) following downconversion. Consequently, the peak in range estimation becomes broader compared to the detected target, resulting in ambiguity, as shown in Figure 2.6(d).

2.4.2 Quantization Error

Due to the adoption of ADCs for analyzing the received signal in the baseband based on the required radar signal processing algorithms, CS-based radar systems may encounter a form of distortion called quantization error. Quantization error occurs when the signal is sampled at a specific sampling frequency and converted to the digital domain with a limited number of bits N_{bits}. The examined N_{bits} represents the digital signal with a finite number of levels, where the analog signal is approximated by the nearest available digital value [VTGG+14]. In this term, quantization error can cause a loss of accuracy in the examined CS-based radar systems. This error is pronounced usually in low SNR_{rad} conditions, where the signal level is close to the noise floor. To cope with this effect, increasing the number of bits enhanced by ADCs can reduce the effects of quantization noise. However, enriches N_{bits} also increases the complexity and cost of the investigated system. Therefore, a trade-off between the preferred accuracy and the constraints of designing the radar system should be adopted to achieve the desired dynamic range of the ADC. In CS-based radar systems, the effective dynamic range depends on the maximum expected σ_{tg}, the minimum expected target range $R_{\text{tg}}^{\text{min}}$, and the system parameters such as transmitter power P_{Tx}, antenna gains G_{Tx} and G_{Rx}, receiver sensitivity, noise figure NF, and adequate bandwidth B_{eff} [GdO+21]. The effective dynamic range can be calculated as

$$\mathcal{D}_{\text{dR}} = \frac{P_{\text{Tx}} G_{\text{Tx}} G_{\text{Rx}} \sigma_{\text{tg}}^{\text{max}} \lambda^2 G_{\text{p}}}{(4\pi)^3 (R_{\text{tg}}^{\text{min}})^4 k_{\text{Bl}} B_{\text{eff}} NF} \tag{2.22}$$

where k_{Bl} is the Boltzmann constant, $B_{\text{eff}} \ll B$, T_{th} represents the temperature, $P_{\text{N}} = k_{\text{Bl}} T_{\text{th}} B_{\text{eff}} NF$ is the noise power, and ($\mathcal{D}_{\text{dR}}/G_{\text{p}}$) is proportional to N_{bits} according to the factor $(1.76 + 6.02 \cdot N_{\text{bits}})$ [VTGG+14].

2.4.3 Calibration

CS-based radar systems can undergo errors and inaccuracies for several reasons during the measurements. Those errors can yield frequency offsets or phase mismatches and affect the measurement results [FJE21], [HL20]. Therefore, one of the calibration approaches should be adopted before evaluating the results to correct the measurements.

One approach adopted in this work for measuring CS-based radar systems is to employ a reference measurement before starting the actual counterpart. The measurements transmit a reference signal representing an ideal chirp that adopts the same system parameters. The measurement campaign should imitate the actual counterpart to estimate impairments that may be presented in the system. The least mean squares (LMS) algorithm can be used as an adaptive approach to calibrate the system. The LMS continuously adjusts the system parameters based on the error between the received and the desired signal, which stands for the chirp signal with no frequency offsets [CL20]. In terms of the nonlinearities of the hardware, pre-distortion algorithms can be performed, and a corrective signal approach can be applied to the CS before transmission to cope with the occurring nonlinearities presented in the system [A+13]. In addition to nonlinearities, quantization errors can also impact the accuracy of CS-based radar measurements. The limited resolution of the ADC causes quantization errors and affects the performance. As a solution, oversampling can rectify the flaws by increasing the sampling rate of the ADC, albeit at the cost of added complexity within the system [HL20].

It should be noted that the algorithms mentioned above cover solely the main aspects of conventional radar systems. However, since radar systems are desi- gned with complexity dependent on several components, hardware architectu- res, circuit topologies, and different applications, many calibration algorithms have been introduced in the last decade to address this topic in more sophistica- ted schemes, such as the calibration in MIMO-based radar systems [V+20] and the calibration of a network of radar sensors [GJSW23].

2.5   CFAR Detection

In CS-based radar systems, the RDM visualizes reflected signal strengths as a function of range and Doppler concerning the examined targets in the surroundings detected by the radar system. Constant False Alarm Rate (CFAR) is an algorithm employed to detect targets in the range-Doppler profile while minimizing false alarms based on the assumption that the background noise in the range-Doppler profile follows a known statistical distribution. The CFAR detector calculates a threshold value based on the assumed distribution and then compares the signal strength at each range-Doppler cell in the RDM to the desired threshold. The selected cell is classified as a potential target if its signal strength exceeds the threshold. One prominent model of CFAR detection adopted in this thesis is the Cell Averaging CFAR (CA-CFAR) algorithm [Wei82]. A window with a predetermined size is applied to the desired section of the investigated range-Doppler map. Since the chosen window contains both the cell of interest and surrounding cells, the average of the signal strengths in the window is calculated, and a threshold is derived based on the statistical distribution of the background noise. If the signal strength overcomes the assigned threshold, the cell is marked as a potential target [Wei82]. Another model of CFAR is the Ordered Statistic CFAR (OS-CFAR) algorithm [El 95], where the signal strengths in the window are ranked from lowest to highest, and a threshold is derived based on the statistical distribution of the lowest-ranked signals. If the signal strength surpasses the assigned threshold, the cell is marked as a potential target. Although the CFAR algorithm can help to improve target detection in the investigated environment, it undergoes some limitations. The CFAR can either miss targets weaker than the background noise or produce false targets if the background noise does not follow the assumed statistical distribution. Fig. 2.7 illustrates an example of CS-based radar systems enhanced by the CA-CFAR algorithm for range-Doppler detection. In Fig. 2.7(a), the scenario proposed for the investigation is depicted, while Fig. 2.7(b) and Fig. 2.7(c) visualize the RDMs for detecting one target and two targets, respectively.
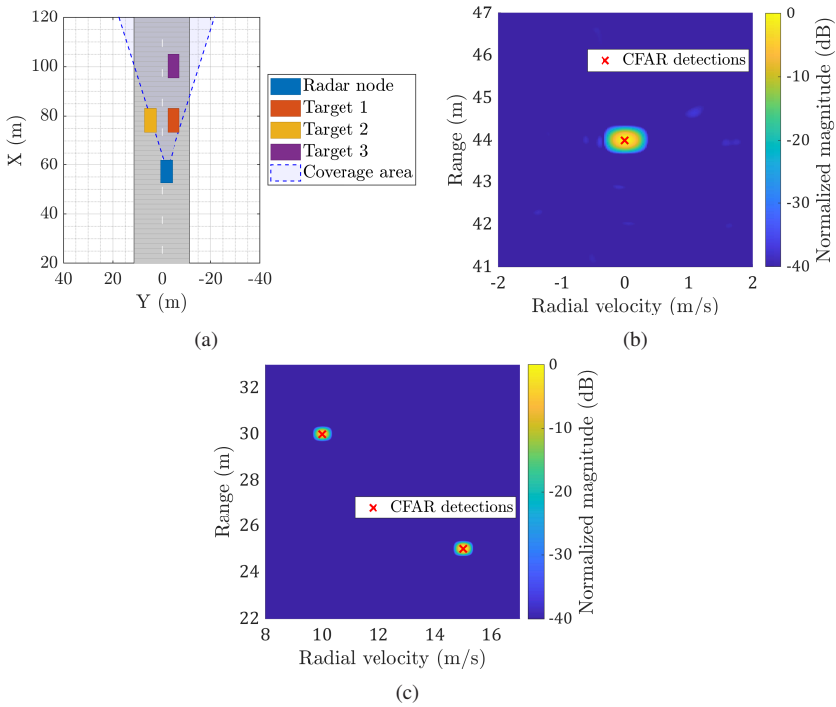
Fig. 2.7: Visualization of the examined scenario and radar image for targets at $\{R_{\text{tg}} \in \{25\,\text{m}, 30\,\text{m}, 44\,\text{m}\}, v_{\text{tg}} \in \{15\,\text{m/s}, 10\,\text{m/s}, 0\,\text{m/s}\}\}$ with false alarm ratio $P_f = 10^{-5}$. (a) The examined scenario related to automotive applications. (b) RDM for CS-based radar with zooming based on the detection of the target $\in \{R_{\text{tg}} = 44\,\text{m}, v_{\text{tg}} = 0\,\text{m/s}\}$. (c) RDM for CS-based radar detecting the remaining two targets.

2.6 MIMO

MIMO-based CS radar is an advanced form of radar that employs multiple antennas at both the transmitter and receiver ends [BJT21, BKYA13]. The employment of MIMO allows for a more precise and detailed radar image, which provides additional information connected with specifying the parameters of the targets examined in the surroundings in the azimuth and elevation domains. In MIMO-based CS radar, multiple antennas transmit uncorrelated chirp si-
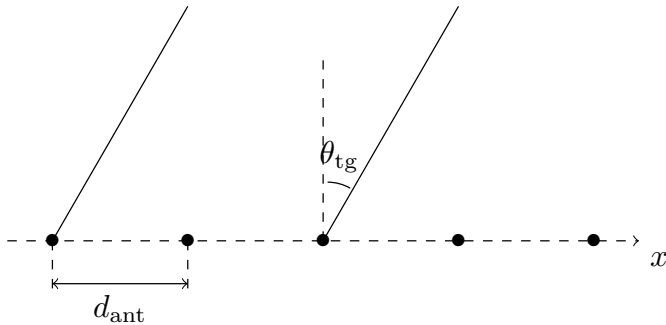
Fig. 2.8: Position of antenna elements with a distance d_{ant} between the elements and angle θ_{tg}.

gnals while their counterparts at the receiver side collect the reflected signals. Next, the received signals from all antennas at the receiver side are processed so the radar system can reconstruct detailed information about the examined targets, including their range and Doppler and their orientation in azimuth or elevation. If CS-based radar systems are extended with MIMO features, the quality of ADAS and autonomous systems can be improved since the orientation of objects in the surroundings can be determined more accurately. In this sense, the examined vehicles can navigate complex environments and avoid critical cases more effectively, enriching the scheme of autonomous driving in the approaching days.

Two popular techniques for transmitting orthogonal signals through multiple antennas in MIMO CS-based radar are Time-Division Multiplexing (TDM) [HFS22], [HT20], [LWYF21] and Frequency-Division Multiplexing (FDM) [N+20], [NHK19], [PFWS13]. In TDM, each antenna transmits a unique sequence of chirp signals during a specific interval in an interleaved pattern while the receiver processes the received signals according to the predetermined pattern to extract the desired information in azimuth and elevation. Since the pattern of MIMO-based TDM is designed in the time domain, TDM is considered a simple and effective technique for MIMO CS-based radar, which requires minimal additional hardware and provides good spatial resolution. However, TDM may undergo limitations proportional to the number of utilized antennas since each antenna occupies a predefined number of transmitting signals within the chosen sequence. This rotation of uncorrelated signals can shrink the esti-

mated maximum velocity provided by the radar system. In MIMO-based FDM systems, each antenna transmits a predetermined sequence of CS signals with different carrier frequencies according to a desired pattern. This adoption solves the reduction of the measured maximum velocity since multiple antennas can simultaneously transmit signals in different bandwidths. However, FDM can require more complex frontends to design and separate transmitted and received waveforms. Besides, FDM can also suffer from interference between the different carrier frequencies used by the antennas, which can reduce the overall system performance and impact the range resolution achieved by the radar system [S$^+$18]. Based on CS-based radar systems, multiple transmitters and receivers are employed to estimate the direction of arrival (DoA) or angle of arrival (AoA). A uniform linear array (ULA) of several elements can be selected to represent the antennas to achieve the desired purpose. According to Fig. 2.8, the aforementioned elements are separated by a distance d_{ant}. Since the virtual array concept for MIMO radar with N_{Tx} transmitters and N_{Rx} receivers by adopting orthogonal waveforms [FB08], [Roo20], the occurred delay associated with the examined target at the receiver side can be modified based on (2.6) by $\tau_{tg} = \frac{2(R_{tg}+v_{tg}t)+l_{ant}d_{ant}\sin(\theta_{tg})}{c_0}$, where l_{ant} is the index dependent on the receive antenna. In this framework, the variation of the phase at the receiver side based on the IF signal of the l_{ant} can be expressed by (2.12) and (2.12) as

$$\phi_{l_{ant}} = \frac{2\pi l_{ant}d_{ant}\sin(\theta_{tg})}{\lambda}. \tag{2.23}$$

Given (2.23), a DFT operation, as depicted in Fig. 2.9, can be applied among the receive channels L_{ant} to extract the angle information leading to

$$\frac{2\pi l_{ant}\beta}{L_{ant}} = \frac{2\pi l_{ant}d_{ant}\sin(\theta_{tg})}{\lambda}, \tag{2.24}$$

where $\beta \in \{1, \ldots, L_{ant}\}$. In this term, the angle can be derived from

$$\theta_{tg} = \arcsin\frac{\beta\lambda}{L_{ant}d_{ant}}, \tag{2.25}$$
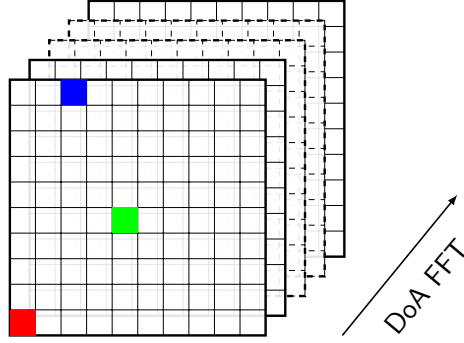
Fig. 2.9: Visualization of 3D layers of range-Doppler profiles representing the estimation of DOA using FFT.

(a)

(b)
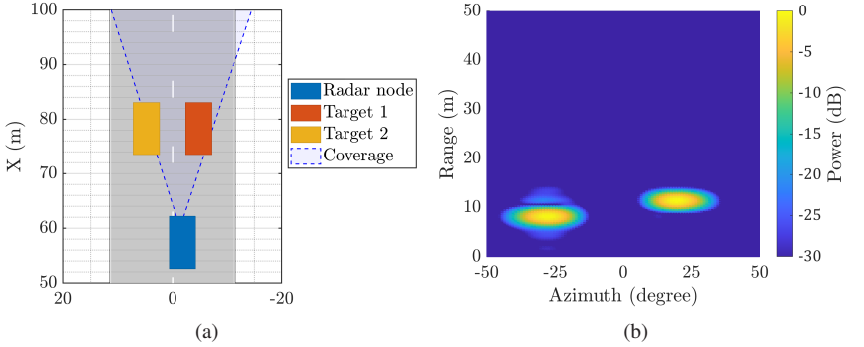
Fig. 2.10: Visualization of the radar image for targets at $R_{tg} \in \{8\,\text{m}, 11\,\text{m}\}, \theta \in \{-26°, 23°\}$. (a) The representation of the examined scenario for automotive applications. (b) Range-azimuth map for the examined targets.

If $d_{ant} = \lambda/2$, the field of view for θ_{tg} is assigned to $-90° \leq \theta_{tg} < 90°$. Besides, if $-L_{ant}/2 \leq \beta < L_{ant}/2$ and the estimated angle can be given as

$$\arcsin \frac{-\lambda}{2d_{ant}} \leq \theta_{tg} < \arcsin \frac{\lambda}{2d_{ant}}. \qquad (2.26)$$

Fig. 2.10 depicts an example of CS-based radar systems enhanced by MIMO schemes for range-azimuth detection. In Fig. 2.10(a), the scenario proposed

for the investigation is visualized, while Fig. 2.10(b) illustrates the range and angles of examined targets, respectively.

2.7 System Demonstrator and Measurement Setup

To investigate the CS-based radar systems introduced previously connected with state-of-the-art, a demonstrator with f_c = 79 GHz components is built, and proof of concept measurements are performed at the Institute of Radio Frequency Engineering and Electronics (IHE). Fig. 2.11 shows an exemplary block diagram of the hardware components employed throughout the investigation. The measurement setup consists of two subharmonic I/Q mixers, a frequency multiplier, an amplifier, two voltage sources, a signal generator, and an RF system-on-chip (RFSoC). The RFSoC can generate the transmit signal, and the received counterpart can be evaluated.

2.7.1 Hardware Components

In recent decades, researchers have been interested in millimeter-wave frequencies due to the available high bandwidth and spectrum of applications that this frequency range can represent. However, generating signals based on this can be an issue in laboratories due to the limitations of components and their expensive price. To overcome these challenges, a signal generator with a limited frequency range of up to 10 GHz is employed in combination with a frequency multiplier to extend the frequency range up to 40 GHz, as depicted in Fig. 2.11. The signal from the generator is fed into two subharmonic mixers as an LO signal, which is divided using a power divider to serve both mixers. These two mixers are used in the frequency range of 71 to 86 GHz, with a subharmonic band of 29 to 43 GHz according to the datasheets in Appendix A. Besides, a Zynq UltraScale+ RFSoC ZCU111 is employed as a platform to generate and process transmitted and received signals within the system. To reach a reasonable level of SNR_{rad}, a PA is enclosed to amplify the signal generated in the RF domain. This high-power amplifier is necessary to compensate for the high attenuation of the millimeter-wave signals at these frequencies.
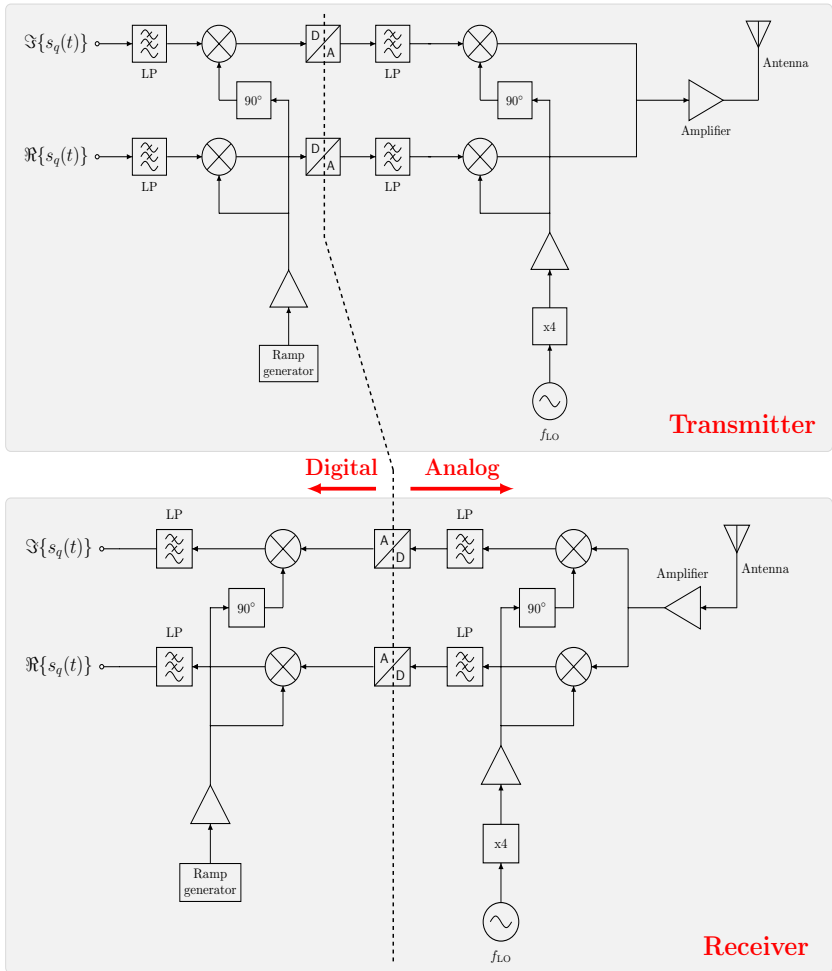
Fig. 2.11: Exemplary block diagram of the proof-of-concept transmitter and receiver employed in this thesis with two subharmonic I/Q mixers, a frequency multiplier, amplifiers, a signal generator, and an RFSoC, where $s_q(t)$ represents the information signal for CS-based radar system in the baseband.

RFSoC

The Zynq UltraScale+ RFSoC ZCU111 is a high-performance SoC developed by Xilinx. This advanced SoC simultaneously combines multiple functionalities including FPGA programmable logic, integrated ADC, and digital-to-analog (DAC) converters. Since the platform comprises several steps relative to signal processing, it has been designed for employment in large-bandwidth applications, such as wireless communications and signal processing. The ZCU111 includes 12 bit ADCs and 14 bit DACs with sampling rates up to $4.096\,\mathrm{GS\,s^{-1}}$ and $6.554\,\mathrm{GS\,s^{-1}}$, respectively [Xil23]. These high-speed converters enable the device to process extremely wideband signals, making it suitable for adoption in several applications [Xil23].

The Zynq UltraScale+ RFSoC ZCU111 SoC comprises two main sections. The former is the processing system (PS), and the latter is programmable logic (PL), as depicted in Fig. 2.12. The PS adopts Arm Cortex-A53 processors utilized in many advanced boards and devices. Furthermore, the PL involves a set of programmable logic gates responsible for reconfiguring the internal circuits based on the task requirements. In addition, the RFSoC incorporates digital RF memory (DRFM), which provides a high-speed interface between the ADCs, DACs, and the PL. The ADCs and DACs are connected to RF/IF and IF/RF interfaces, which allow for direct system design of RF signals connected with the same SoC. In addition to the processing system and programmable logic, the ZCU111 includes DDR4 memory. The DDR4 memory interface supports up to 4 GB of memory. Besides, a sync module is included within the ZCU111 to provide the required synchronization features for the entire design.

2.7.2 Measurement Setup for CS-based Radar System

Within the scope of the thesis, signal processing techniques and radar detection approaches are employed to virtualize the examined targets and estimate their assigned delays and Doppler shifts. The RFSoC generates the desired signal in the baseband at 1 GHz. Besides, the RFSoC enables precise control and modulation of the emitted signal based on its integrated mix of analog and digital capabilities through DACs and ADCs. Next, the virtual targets are constructed by a radar target simulator (RTS), which emulates the behavior of objects encountered in real-world scenarios by adopting pre-assigned delay and Doppler
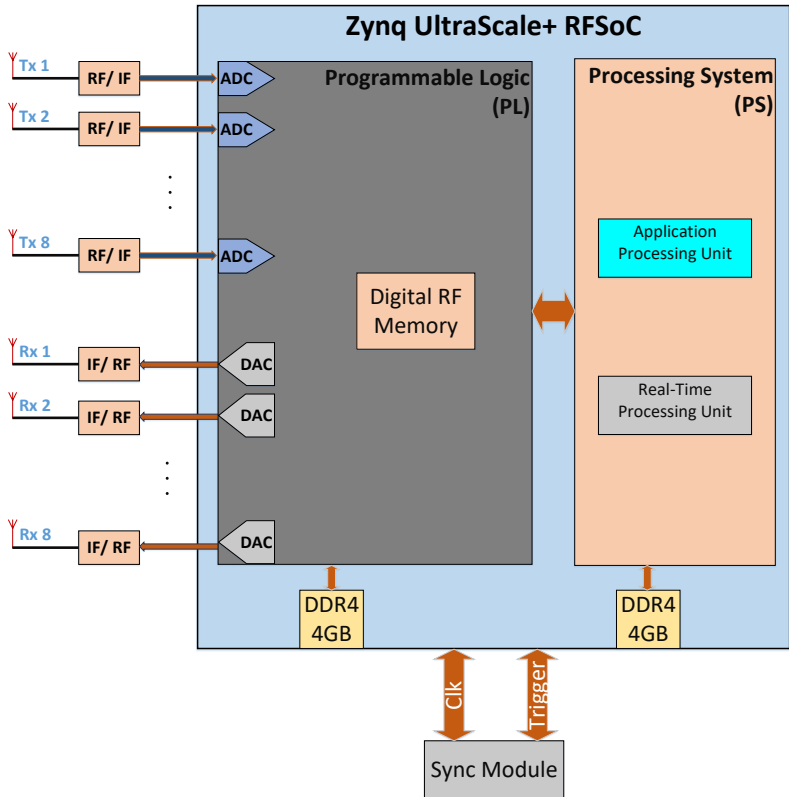
Fig. 2.12: Hierarchy of the RFSoC with PS, PL, DDR4 memory, IF/RF, RF/IF interfaces, and a sync module. Besides, PS involves both a real-time processing unit (RPU) and an application processing unit (APU). On the other hand, PL includes DSP slices, configurable logic blocks (CLBs), DRFM, as well as ADCs, and DACs.

35
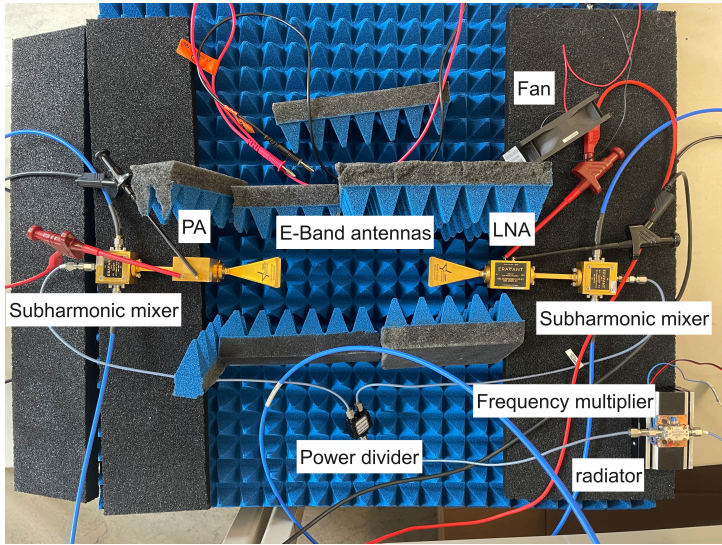
(a)
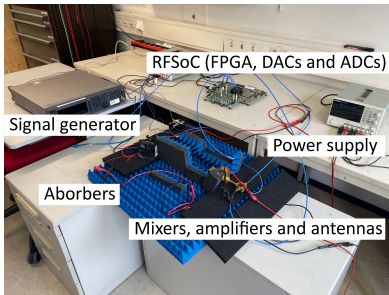
(b)
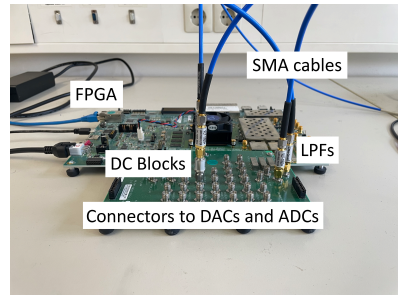
(c)

Fig. 2.13: Illustration of the measurement setup for CS-based radar systems. (a) The front end in the scale IF/RF by 79 GHz. (b) The entire measurement setup. (c) The RFSoC.

shifts. In this context, the measurement setup based on RTS can evaluate the system performance under eased and dynamic conditions without having a large hall or emulator for Doppler measurements. The generated analog signal is then directed to the RF-front end, operating at a frequency of 79 GHz to combine the effects of the virtual from RTS and physical channels. The antenna transmits the signal into space to interact with the environment and generate echoes based on the setup. The receive antenna captures these echoes, and the received signal is downconverted to the baseband by the front end. Within the RFSoC, the downconverted baseband signal undergoes further processing steps to extract the information associated with the assigned targets, such as the delay and Doppler shifts.

Fig. 2.13 illustrates the measurement setup adopted in this thesis held in one of the laboratories at IHE institute. On the transmitter side, a signal generator generates the desired LO signals at 9.75 GHz. The signal is multiplied by a frequency multiplier included in the setup to enable the generation of signals at higher frequencies 38 GHz. Since the setup adopts subharmonic mixers, the signal is generated at 79 GHz by a mixer at the transmitter chain. Besides, a PA is employed to amplify the transmit signal. Afterward, an E-Band horn antenna is incorporated to radiate the examined signal into the medium. The transmit signal is attenuated according to the adopted frequency and received by another E-Band horn antenna. An LNA is employed to enhance the sensitivity of the received signal, which is downconverted with a second subharmonic mixer into the baseband domain. The same LO signal in the transmitter is adopted into receiver chains through a power divider, which splits the LO signal into two with equal power levels (-3 dB). The RFSoC, which consists of a high-performance FPGA, fast DACs, and ADCs, is incorporated to represent the desired signal in the baseband. In addition, LPFs and DC Blocks are incorporated into the measurement setup to filter out unwanted high-frequency components and block any DC offset, respectively. For CS-based radar measurements, a sequence with Q chirps and bandwidth B is transmitted. T_{chirp} and T_{RRI} correspond to the time duration of each chirp and the interval duration, respectively, as shown in Table. 2.1. To generate the examined targets concerning the radar measurements, an RTS is integrated into the RFSoC. The RTS was also developed at the IHE and tested with different radar modulation types. In addition, radar measurements are performed and further evaluated basically with a virtual radar target generated with a distance ($R_{\text{tg}} = 15$ m) and velocity ($v_{\text{tg}} \in \{0 \, \text{m/s}, 60 \, \text{m/s}\}$) using the radar target simulator with $P_{\text{Tx}} = 0$ dBm transmitted from the RFSoC,
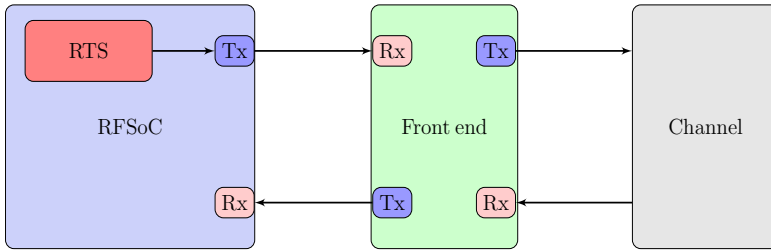
Fig. 2.14: Measurement procedure for detecting targets using CS-based radar systems. RFSoC is responsible for generating the desired signal and demodulating it after downconversion. RTS emulates the examined targets, and the front end represents the components employed at 79 GHz.

Table 2.1: Measurement parameters

Symbol	Parameter	Value
B	Chirp bandwidth	1 GHz
f_c	Radar carrier frequency	79 GHz
f_s	Sampling frequency	100 MHz
T_{chirp}	Chirp duration	10 µs
T_p	Pause duration	0.1 µs
T_{RRI}	Ramp repetion interval	10.1 µs
Q	Chirps per sequence	1024

as illustrated in Fig. 2.15. It should be noted that a similar hierarchy in Fig. 2.14 is adopted for data transmission and synchronization, which will be discussed in upcoming Chapters, dependent on the examined approach. Besides, T_{chirp} and T_{RRI} are kept short of sending many chirps, as explained later in Chapter 3. Based on Table. 2.1, $\Delta R = 0.15$ m, $R_{unamb}^{max} = 150$ m, $\Delta v = 0.184$ m/s, and $v_{unamb}^{max} = 93$ m/s.
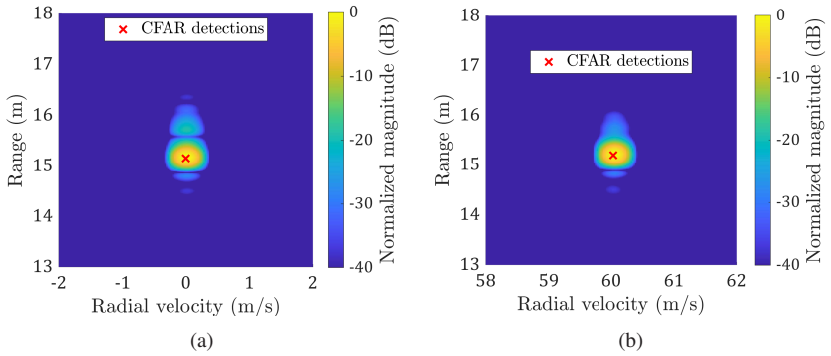
Fig. 2.15: Visualization of the radar image based on the detection achieved CS-based radar systems. (a) RDM of a target $\{R_{\text{tg}} = 15\,\text{m}, v_{\text{tg}} = 0\,\text{m/s}\}$. (b) RDM of a target $\{R_{\text{tg}} = 15\,\text{m}, v_{\text{tg}} = 60\,\text{m/s}\}$.

2.8   Conclusion of this Chapter

This chapter focuses on CS-based radar signals employed in the automotive sector for combined radar and communication systems. Besides, it has examined the effectiveness of the suggested waveform in identifying objects in the vicinity specifically. The investigation employed a preliminary measurement arrangement with an RTS emulator to evaluate the system and assumed it to be a core milestone in the upcoming chapters to investigate the integration of communication symbols within the radar signal. Finally, the outcomes have demonstrated the credibility of the CS-based waveform to detect the targets in the surroundings.

3 Communication-assisted Chirp Sequence Radar

This chapter introduces two innovative communication techniques for CaCS-based radar systems discussed in Chapter 1 (Fig. 1.2). These proposed techniques combine communication data with the transmission of radar signals and utilize a separate communication receiver structure while minimizing adverse effects on the radar functionalities. The signal structure used in this section is derived from Chapter 2, in which a CS-based radar signal consisting of several linear ramps is used for radar measurements.

The main milestones of this chapter can be summarized as follows. Initially, a traditional model of RadCom-based systems is demonstrated for combining radar signals with communication data. Then, two innovative techniques are discussed in detail for incorporating communication data into the radar signals. The first technique, partial chirp modulation (PM) [ANWZ19], involves modulating the chirp with communication symbols within a limited bandwidth. The second technique, TFSK [AdOGN+20], is derived from the LoRa scheme and modulates the information in predetermined time and frequency shifts, and both communication approaches are evaluated based on various metrics. The assessment of the CaCS-based system proposed involves evaluating the radar performance under both communication techniques using the radar RDM. The impact on target detection is also examined by assessing the peak sidelobe level ratio (PSLR) and integrated sidelobe level ratio (ISLR), which increase with modulated chirps. Regarding communication performance, the link budget is analyzed to determine the communication distance for the proposed approaches according to different SNR values. In addition, the Bit Error Ratio (BER) and constellation diagrams for QPSK symbols are compared to their theoretical counterparts for the PM communication technique. On the other hand, for TFSK, a mathematical expression for the Symbol Error Ratio (SER) is derived and introduced as an extended approach to orthogonal waveforms. Finally, the impact of the channel on the transmission of both communication methods is

evaluated and equalized. The theoretical analyses are presented throughout the chapter, and the results are illustrated at the end, incorporating simulations in MATLAB and measurements with the previously mentioned demonstrator in Chapter 2.

The aforementioned aspects are deducted for SISO-based radar systems and can be extended to retain the MIMO enhancement in CS-based radar systems. Apart from that, the carried out investigations are mainly based on the publication from [ANWZ19, AdOGN⁺20, A⁺22a] with reformed and reused texts and figures © [2019], [2020], [2021], [2022], [2023] and [2024] IEEE.

3.1   Conventional CS Modulation Schemes

The impact of interference on radar quality has recently been under investigation due to its importance in applying ADAS features and enhancing comfort and safety on the road [BBW17]. In this context, enforcing communication data between the radars in the same environment can ensure the exchange of information concerning their signal properties and enable them to avoid mutual interference. While most current automotive radars utilize FMCW signals with short durations, limited studies have explored integrating communication data into radar signals. Generally, the classical FMCW with integrated data transmission capability has been considered in previous studies [BEJ07]. Additionally, other research has investigated RadCom systems based on chirp spread spectrum (CSS) as in [XTW11] or evaluated radar communications by incorporating known digital modulation techniques as the authors presented in [S⁺17], [MBM17], [SFHS15]. However, the studies above require significant changes to the chain of the joint-radar communication system and have achieved low data rates.

One notable illustration of the traditional CaCS system can be found in the research paper [GdO⁺21], in which the transmit signal consists of multiple chirps $Q_{rc} \in \mathbb{N}_+$ with a time duration of T_{RRI}. Each interval within the signal contains a linear chirp lasting for T_{chirp}, occupying a bandwidth of B, followed by a pause interval of T_p to reset the PLL. Thus, $T_{RRI} = T_{chirp} + T_p$ and $T_{seq} = Q_{rc}T_{chirp} + (Q_{rc} - 1)T_p$. One of the conventional schemes, such as QPSK, is used to modulate each chirp in the modulated data stream, as shown in Fig. 3.1. There are two approaches to integrating the communication data
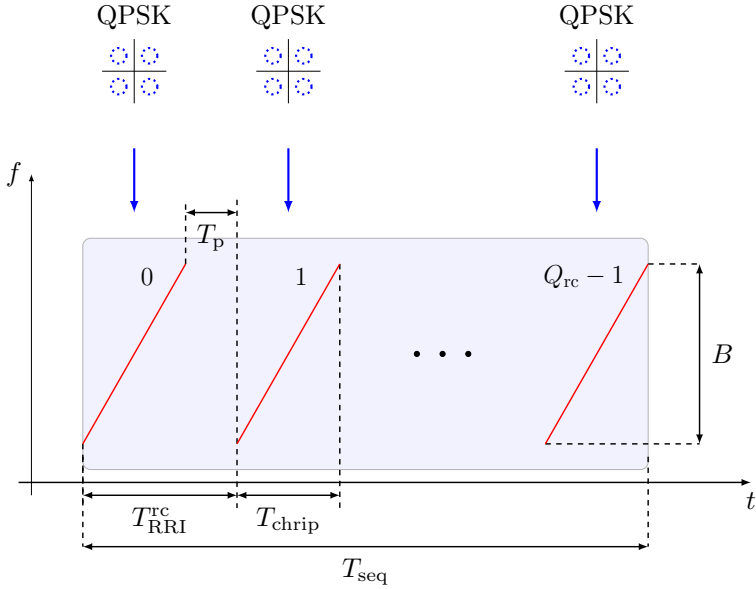
Fig. 3.1: CS representation with time duration T_{seq} and modulated with QPSK modulated. Q_{rc} is the number of intervals with a time duration T_{RRI} for each. Each interval encompasses a chirp with time duration T_{chirp} and a pause interval T_p, and it spans over bandwidth B [GdO$^+$21].

in the CS system discussed earlier. The first approach involves using an analog phase shifter as a modulator to adjust the phase of each transmit chirp, which is demonstrated in [TI20] with the AWR1843 chip from TI for MIMO-based radar applications. The second approach involves pre-programming the PLL [TI17] to introduce frequency or phase changes according to frequency-shift keying (FSK) or QPSK, as described in [GdO$^+$21]. The signal generation and processing scheme for radar applications in this scheme is similar to the one explained in Section 2.3. In this scheme, a PLL is primarily used to generate the transmit signal, and a programmable phase shifter, adopted from AWR1843, is used to modify the phase between the chirps. In the time domain, the continuous time signal $x_{q_{rc}}(t)$ transmitted for enabling both radar and communication properties can be characterized as

$$
x_{q_{rc}}(t) = \begin{cases} A \cos\left(\pi\mu\left(t - q_{rc}T_{RRI}^{rc}\right)^2 + 2\pi\left(f_c - \frac{B}{2}\right)t + \varphi_0 + \varphi_{q_{rc}}\right), \\ t \in [q_{rc}T_{RRI}^{rc}, q_{rc}T_{RRI}^{rc} + T_{chirp}) \\ \\ 0, \\ t \in [q_{rc}T_{RRI}^{rc} + T_{chirp}, (q_{rc}+1)T_{RRI}^{rc}) \end{cases} \tag{3.1}
$$

where q_{rc} represents each chirp within the transmit sequence, as explained in (2.1), A denotes the amplitude of the transmit signal, μ is the chirp rate, f_c is the center frequency. B presents the signal bandwidth, φ_0 is the initial phase of the investigated signal, and $\varphi_{q_{rc}} \in \{\pi/4, 3\pi/4, 5\pi/4, 7\pi/4\}$ represents the modulated phase. A sequence of multiple chirps Q_{rc} with index $q_{rc} \in \{0, 1, \ldots, Q_{rc} - 1\}$ combined with short spacing is designed to estimate the RDM of different objects in automotive scenarios. At the receiver of the CaCS-based radar system, the signal $y_{q_{rc}}(t) \in \mathbb{R}$, which contains the output version of $x_{q_{rc}}(t) \in \mathbb{R}$ by the channel, and additive noise, which is captured by the receive antenna. It should be noted that the influence of communication data should be removed because of the dual use of transmit chirps for radar and communication. For radar signal processing, the same procedure presented in Section 2.3 is employed to detect the information of the targets in distance and velocity. Therefore, the received sequence undergoes amplification, and after downconversion, DFTs are subsequently performed to extract the RDM for the targets in the surroundings. For communication with another CaCS node and adopting the same signal $y_{q_{rc}}$, a downconversion with a reference chirp signal is applied to extract the transmit communication data. In this term, the synchronization between the transmitter and receiver should be ensured to confirm the exact alignment of the examined signal in the time-frequency plane. Subsequently, DFTs are performed as an art of a matched-filter-like communication receiver [GdO+21], and the QPSK symbols can be extracted from the detected peaks in the frequency domain to deliver the estimated data stream.

3.1.1 Communication Channel

In CaCS-based radar systems, the communication channel encompasses all the different paths (denoted as $P_{th}^{com} \in \mathbb{N}_+$) initiated by the transmitter, carrying power $P_{com}^{Tx} \in \mathbb{R}_+$ from the transmitting antenna to the corresponding receiver.

The channel incorporates various distortions introduced by the environment, including an assortment of propagation effects like attenuation $\alpha_\wp$, delay $\tau_\wp$, and phase shift linked to $f_\wp^{\mathrm{D}}$. Besides, the objects in the vicinity can either reflect or scatter the signal, giving rise to echoes or reflections that the communication receiver can detect from greater distances. The received signal $y_{q_{\mathrm{rc}}}(t) \in \mathbb{R}$, with a time delay of τ_{shift} and frequency shift f_{shift}, can be represented as

$$y_{q_{\mathrm{rc}}}(t) \approx \sum_{\wp=0}^{P_{\mathrm{th}}^{\mathrm{com}}-1} \alpha_\wp x_{q_{\mathrm{rc}}}(t - \tau_\wp - \tau_{\mathrm{shift}}) e^{\mathrm{j}2\pi f_\wp^{\mathrm{D}} t} e^{\mathrm{j}2\pi f_{\mathrm{shift}} t} + w(t), \qquad (3.2)$$

Given G_{Tx} and G_{Rx} as the antenna gains, $\lambda = c_0/f_{\mathrm{c}}$ as the wavelength of the transmitted signal, and $R_{\mathrm{com}} \in \mathbb{R}$ as the distance between the communication nodes. In this term, the attenuation $\alpha_\wp \in \mathbb{R}$, in this case, can be described as

$$\alpha_\wp = \sqrt{\frac{G_{\mathrm{Tx}} G_{\mathrm{Rx}} \lambda^2}{(4\pi)^2 R_{\mathrm{com}}^2}}, \qquad (3.3)$$

where the noise is excluded from (3.2) for simplicity.

3.2   Novel Modulation Schemes

In the last section, two key factors are observed regarding the system level based on conventional communication methods. Initially, each chirp is assigned only one communication symbol to minimize the impact on radar functionalities [GdO+21], which leads to a lower data transmission rate. Additionally, a modulator must be incorporated into the system based on the assigned communication symbols. Consequently, this section solves one of the drawbacks above by proposing two innovative communication techniques. The first method suggests partially modulating each chirp within a narrow bandwidth, denoted as $B_{\mathrm{com}} \ll B$, to keep the impact of communication on the radar quality minimum and allow, simultaneously, for the transmission of multiple symbols. However, a separate modulator is still required to modulate the assigned communication symbols [Hü20]. Regarding the second statement, the chirps can be rearranged in the time-frequency plane to represent distinct communication symbols, where the generation is basically based on predetermined time and frequen-

cy shifts. This adaptation eliminates the necessity of incorporating a separate modulator into the system, as done in LoRa [FA18]. This modification can be implemented by programming the PLL within the radar system circuit to follow a predetermined pattern associated with the communication symbols [TI17].

3.2.1 Partial Chirp Modulation

Using multiple communication symbols to modulate the entire chirp can negatively impact the quality of detecting objects. Therefore, this section proposes to partially modulate the chirps for data exchange between vehicles to limit the impact above on the radar system. In CaCS-based radar systems, where the transmitter handles radar and communication functions, the programmed PLL can modulate the transmit chirps within specific sections based on the desired modulation [TI17]. Selecting upper or lower modulation sections may be suitable for system design if the communication segment is disregarded before radar processing. A programmable complementary phase shifter can be employed to modulate the chirps by adjusting the phase of each chirp using the predetermined communication symbols typically used for MIMO constellations in CS-based radar systems. In this term, the communication symbols can be differentially detected at the receiver side by extracting the phase between successive chirps within a sequence corresponding to each chirp phase [Hü20]. However, these phases should remain coherent on the receiver side to ensure accurate decoding of the desired modulation symbols. Additionally, any modulation technique, such as PSK, can be chosen for CaCS-based radar systems with necessary adaptations made through PLL programming at the transmitter side to generate the desired communication data based on the selected modulation [TI17]. Fig. 3.2 shows a partially modulated chirp signal that experiences a linear frequency change over time. The representation of the modulated part of the chirp in the time domain can be seen in Fig. 3.2(a). Furthermore, the creation of the chirp in the frequency domain can be obtained by applying FT to the signal, as indicated in Fig. 3.2(b), where multiple frequency components are present based on the bandwidth covered and the communication symbols affecting the end of the spectrum. Considering both time and frequency domains, the chirp can be observed in the time-frequency plane by utilizing STFTs on the signal, as depicted in Fig. 3.2(c). However, it is essential to note that the
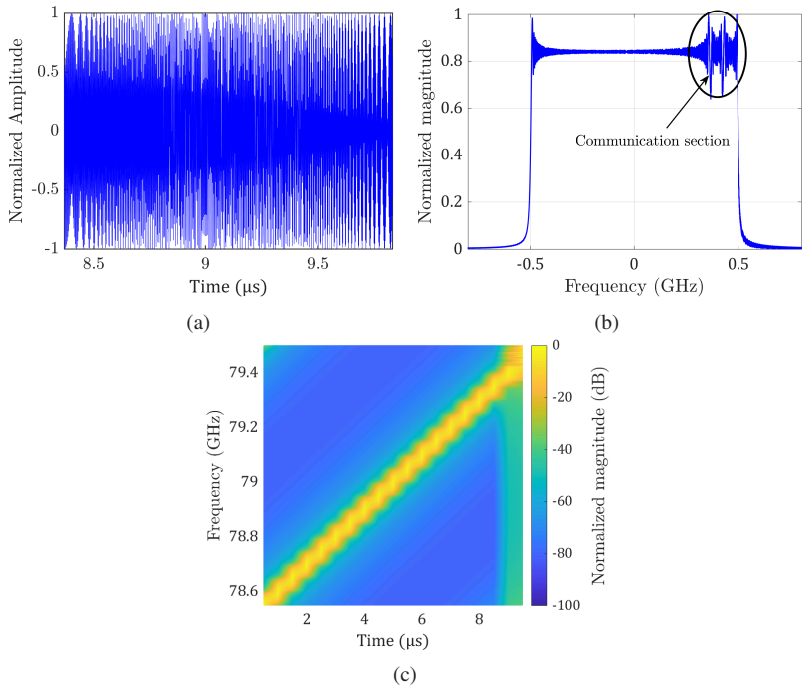
Fig. 3.2: Visualization of one chirp based on PM modulation for the same parameters introduced in Fig. 2.2: $T_{chirp} = 10\,\mu s$, $f_c = 79\,GHz$, and $B = 1\,GHz$. (a) The representation of the communication section in the time domain. (b) The representation of the whole signal in the frequency domain (baseband). (c) Spectrogram of the proposed signal using STFT in the time-frequency plane.

vertical region beyond $8\,\mu s$ appears in vibrant colors due to the constraint in resolution within the relatively short time duration of $T_{chirp} = 10\,\mu s$.

Waveform Structure

In the time domain, the continuous time signal $x_{q_{rc}}(t)$, which serves the dual purpose of facilitating radar and communication properties can be characterized as

$$x_{q_{rc}}(t) = \begin{cases} A\cos\left(\pi\mu\left(t - q_{rc}T_{RRI}^{rc}\right)^2 + 2\pi\left(f_c - \frac{B}{2}\right)t + \varphi_0\right), \\ t \in [q_{rc}T_{RRI}^{rc}, q_{rc}T_{RRI}^{rc} + T_{um}) \\ \\ A\cos\left(\pi\mu\left(t - q_{rc}T_{RRI}^{rc}\right)^2 + 2\pi\left(f_{com}^{Tx} - \frac{B_{com}}{2}\right)t + \varphi_0 + \varphi_{q_{rc}}\right), \\ t \in [q_{rc}T_{RRI}^{rc} + T_{um}, q_{rc}T_{RRI}^{rc} + T_{chirp}) \\ \\ 0, \\ t \in [q_{rc}T_{RRI}^{rc} + T_{chirp}, (q_{rc} + 1)T_{RRI}^{rc}) \end{cases} \quad (3.4)$$

where T_{chirp} represents the chirp duration, T_{um} is the duration of the chirp section without modulation related to one chirp interval within the time duration T_{RRI}^{rc} and other parameters are maintained as in the previous section. According to the second part of (3.4), f_{com}^{Tx} represents the carrier frequency of the communication section at the transmitter side, and B_{com} is the bandwidth occupied in the design for the communication section. A sequence made up of successive chirps Qrc labeled as q_{rc} where $q_{rc} \in \{0, 1, \ldots, Q_{rc} - 1\}$, and has a time duration of T_{seq} and short time spacing T_p, is created to estimate the RDM of different objects in automotive scenarios as explained in Section 2.3 and shown in Fig. 3.3. Each chirp in the sequence represents one or multiple communication symbols at the upper part of the chirp. Apart from that, Fig. 3.4 visually represents the detailed structure of the communication section in one of the CaCS nodes. The communication bandwidth B_{com} incorporates various subbands, including the upper guard band B_g^u, the modulated section B_{mod}, the lower guard band B_g^l, and the preamble bandwidth B_{pre}. It is important to note that all subbands except the modulated section B_{mod} remain unmodulated. The purpose of B_g^u is to account for mismatched symbols during demodulation, as the communication section is situated at the edge of the modulated chirp. On the other hand, B_g^l is specifically designed to counteract the impact of the modulation mechanism on the preamble, ensuring that demodulation does not affect the detection of
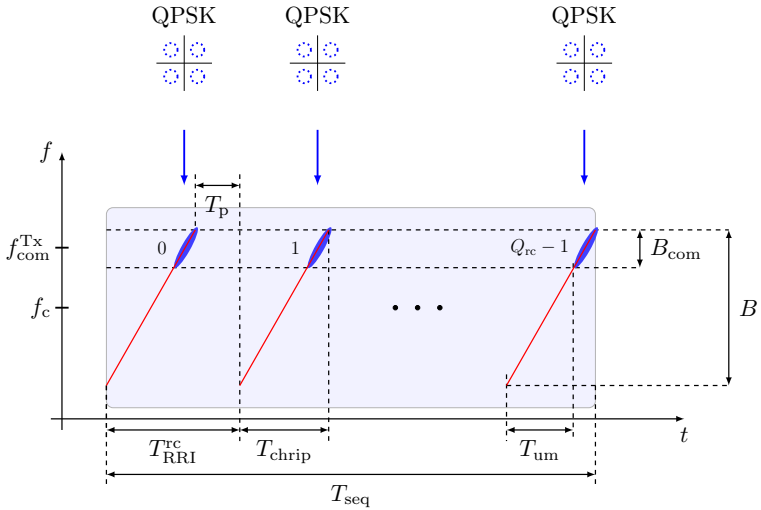
Fig. 3.3: CS representation with time duration T_{seq} and modulated with QPSK modulated. Q_{rc} is the number of intervals with a time duration T_{RRI} for each. Each interval encompasses a chirp with time duration T_{chirp} and a pause interval T_P and spans over bandwidth B. B_{com} is the bandwidth utilized for communication, and T_{um} is the time duration of the chirp section without any communication data [GdO+21].

the communication section. Although the communication receiver occupies the bandwidth B_{com}, the effects on the radar detection are solely determined by the modulated section B_{mod}, which is a trade-off with the efficiency rate $\mathcal{R}_{eff} = B_{mod}/B_{com}$. The maximum achievable $\mathcal{R}_{eff}$ is 1 when $B_{mod} = B_{com}$, and all other subbands have a value of 0.

Radar Functionality

The block diagram for radar signal processing, shown in Figure 2.1, is adopted from the previous chapter for target detection in terms of range and Doppler. The only difference is that the proposed signal is modulated using communication symbols. Once the transmit signal is generated by the selected hardware components (e.g., PLL and phase modulator), it can be transmitted through the transmit antennas in the surroundings. As the signal travels, it experiences de-
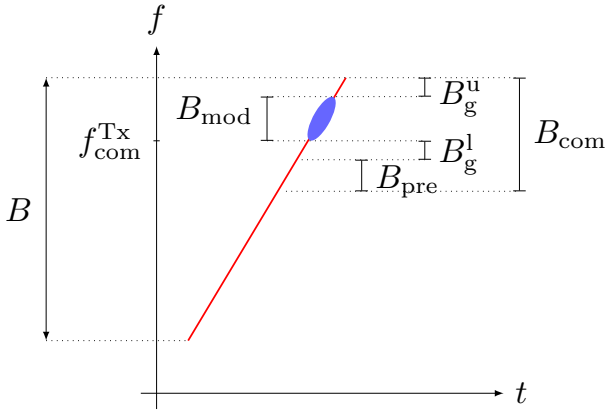
Fig. 3.4: Time-frequency plane of the signal with partial chirp modulation. Here, the condition $B \gg B_{\text{com}} = B_{\text{g}}^{\text{u}} + B_{\text{mod}} + B_{\text{g}}^{\text{l}} + B_{\text{pre}}$ should be fulfilled. B is the entire bandwidth employed for both radar and communication. B_{com} is the utilized bandwidth for communication, B_{g}^{u} is the upper guard band, B_{g}^{l} is the lower guard band, B_{pre} is the bandwidth of the preamble and B_{mod} represents the modulated bandwidth [Win18].

lays and Doppler shifts based on the range and velocity of the examined objects. The radar channel is the same as the one analyzed in Chapter 2, where the RTS has been adjusted to generate virtual objects in the surrounding area. If only a segment of the chirp in the upper or lower section is modulated by the radar transmitter at one CaCS node, this modulated part can be easily maintained in the radar receiver. This analysis only considers the modulation of the upper section, but similar studies can be done for the modulation of the lower part of the chirp. One advantage of modulating the upper part is that the receiver can use an unmodulated part of the chirp below the modulated section as a preamble. If the lower part is modulated, a postamble can be used [Win18]. If the modulated segment is eliminated, the sampled IF signal can be discarded after downconversion at the beginning of the modulated part. However, truncating the examined upper part reduces the utilized bandwidth B of the application. This reduction leads to a worse range resolution ΔR, according to the investigation in Chapter 2. Even though the maximum distance $R_{\text{unamb}}^{\text{max}}$ remains unchanged when discarding the modulated section, the chirp rate μ stays constant relative to the sampling frequency. While the discard does decrease the chirp duration T_{chirp}, the interval time $T_{\text{RRI}}^{\text{rc}}$ remains the same. Therefore, this approach does

not affect the velocity examination discussed in Chapter 2. Apart from that, two procedures can be followed in the radar signal processing chain for chirps with PM modulation. If the modulated section in each chirp is discarded, the radar quality is preserved without being affected by the modulation. However, the estimated range resolution ΔR is worse by the factor $(B - B_{\mathrm{com}})$ than the modulated part in each chirp. On the other hand, if the entire chirp is analyzed, there is a slight deterioration in the ISLR while keeping the parameterization unchanged. The received signal is mixed with its transmitted counterpart upon reaching the receiver. Since the radar receiver is designed to place the output signal after the mixer in the intermediate frequency domain, an LP filter is employed to limit the sampling frequency. Subsequently, an ADC is chosen to convert the signal into a digital format and sample it for further analysis. It should be noted that only the chirps without any gaps in between are considered, resulting in raw data that forms a 2D matrix once sampled. Following this, a process known as a 2D-FFT operation is carried out for each transmit sequence, as explained in Section 2.3. Column-wise FFTs extract the delay information, while row-wise FFTs are applied to obtain the Doppler information. Furthermore, the data obtained can be converted from delay, which corresponds to the range, and Doppler to the radial velocity of the targets being examined. Since the chirps are modulated, the impact of modulating the signal has been analyzed with simulations and measurements. The simulations are investigated and evaluated in MATLAB according to the parameters introduced in Chapter 2, whereas the measurement setup is employed by adopting the same hardware components presented in Section 2.7.

First, the radar image is adopted to visualize the identified targets on a two-dimensional or multidimensional grid [Win07]. In this context, the RDM represents the desired radar image, which captures the information of the targets in the surroundings and presents it on a 2D plane based on the distance and velocity of the detected objects. As explained in Chapter 2, a significant advantage of CS-based radar is its ability to detect pairs of delay and Doppler shifts corresponding to each target without transmitting an additional signal. This approach is different from the FMCW waveform, which fails to accurately estimate the velocity of multiple targets and requires modifications to the structure of the transmit signal. Although the proposed communication technique incorporates the CS waveform with communication data, it still accurately estimates target parameters without a considerable impact on examined radar systems. Additionally, PSLR and ISLR are essential metrics commonly employ-

ed in radar applications to assess the signal processing chain. These metrics can particularly help the radar system classify desired objects from unwanted interference. In this sense, PSLR is a metric that quantifies the ratio between the peak, representing the desired target, and the first maximum peak of the sidelobes [LMI16]. After analyzing the information provided in the preceding section, it can be deduced that the quality of the range profile z_η^{IF} is contingent upon the Doppler shift that has occurred within the profile under evaluation [LMI16]. Consequently, the PSLR level can be expressed as follows

$$PSLR = \frac{\max\limits_{\eta \neq 0}\left|z_\eta^{IF}\right|}{\left|z_0^{IF}\right|}, \tag{3.5}$$

where z_η^{IF} represents the discrete form of the range profile introduced in Chapter 2 as $z_{2D}^{IF}(\zeta, \eta)$ in two dimensions, and the maximum value of η is equivalent to the length of the range profile. ISLR, on the other hand, is a metric that characterizes the integrated energy within the sidelobes of an examined signal. It provides a measure of the unwanted energy or interference present in the sidelobes, which can affect the detection performance and accuracy of the radar system [LMI16].

$$ISLR = \frac{\sum\limits_{\eta \neq 0}\left|z_\eta^{IF}\right|}{\left|z_0^{IF}\right|}, \tag{3.6}$$

If the communication section within the transmitted chirp is not discarded, the signal suffers some loss in dB relative to the PSLR and ISLR levels, as shown further in Section 3.2.3.

Communication

This section delves into the design and verification of the communication receiver for the PM-based modulation method introduced to extend the radar signal with communication data. First, the general structure of the communication receiver is performed. Next, the influence of the channel on the communication symbols is experimentally analyzed.

- *Communication Receiver*

  In practical scenarios, the commonly used bandwidth B employed by CS waveforms can often reach scales of GHz. Given this, if the entire chirp is to be modulated, two options arise. Either entirely digital sampling of the chirps must be implemented, or the receiver needs to incorporate a Frequency Locked Loop (FLL), which necessitates precise synchronization of the start points in each chirp. Furthermore, the impact on radar quality decreases proportionally with the width of the communication section modulated in each chirp signal [Win18]. To cope with this, an innovative technique proposed in this chapter is to modulate each chirp only partially with the communication symbols, based on a receiving frequency f_{com}^{Tx} as depicted in Fig. 3.4. The choice of f_{com}^{Tx} ensures that it falls within the bandwidth B_{com} of the communication receiver, which comprises the upper guard band B_g^u, the modulated section B_{mod}, the lower guard band B_g^l, and the preamble bandwidth B_{pre}. One of the foremost contributions of this study involves introducing a new concept for receiving communication data based on CaCS-based radar systems. In this context, a separate receiver is dedicated to demoduate communication symbols within a significantly smaller bandwidth B_{com}, compared to the overall system bandwidth B. The received signal is then sampled and processed digitally to meet the requirements adopted in the automotive domain. By implementing this approach, the demand for fast ADCs decreases proportionately to the ratio B/B_{com} while maintaining the same number of transmit communication symbols. Figure 3.3 and Figure 3.4 illustrate the specific section of the received signal (highlighted by blue ellipses), which is occupied by communication symbols. It is important to note that the location of this section can be defined anywhere relative to the proposed design. In the communication receiver of the CaCS-based radar system, the reflected signal is amplified by a low-noise amplifier (LNA) and mixed with the receiver communication frequency f_{com}^{Rx}, as depicted in Figure 3.5. The signal then undergoes LP filtering to limit the required sampling rate in the digital domain. If an IQ-mixer is used (as shown in Figure 3.5), it is essential to assign the cutoff frequency of the low-pass filter to be $B_{mod}/2$. For demodulation, the upper portion of the transmit signal is correlated with a reference chirp based on B_{pre} to detect the start of the modulated section. The specific demodulation technique depends on the assigned modulation scheme, which has been extensively studied and evaluated for its robustness in the proposed system, as described in [ANWZ19].
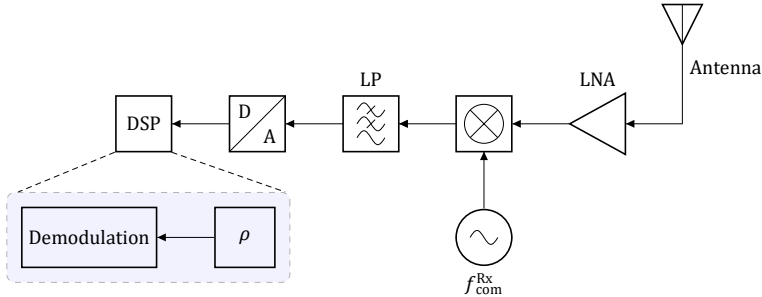
Fig. 3.5: Illustration of the block diagram of the communication receiver at one CaCS-node for PM-based modulation, where $f_{\text{com}}^{\text{Rx}}$ the receiver frequency based on the front end in Chapter 2, where the frequency shift can be directly applied to $f_{\text{LO}}^{\text{Rx}}$ [AGdON+24].

Before the demodulation stage, the receiver should correctly anticipate the beginning of the modulated part of each chirp; otherwise, that can yield an error during the decoding process. The procedure depicted in Fig. 3.6(a) is adopted to demodulate the transmit communication symbols within the communication receiver [Win18]. At the beginning, the start position of the communication section is detected by employing a cross-correlation between the sampled received signal and a reference preamble. Hence, the start of the preamble generates a peak pointing out the location of the communication symbols. Next, after detecting the starting point of the communication section, the modulated chirp signal is downconverted, and potential frequency and phase offsets that can occur during the mixing process can be estimated and corrected. For a sequence of multiple chirps, Fig. 3.6(b) illustrates the peak generated by the correlation function and a series of peaks in Fig. 3.6(c), where each detected point within $T_{\text{RRI}}^{\text{rc}}$ determines the start of the communication section in each chirp. In the scale of demodulation, the individual excised chirps are down-mixed by point-wise multiplication of the received chirps with the complex conjugate of a reference chirp, where the reference chirp spans the bandwidth B_{com}. After this step, the downconverted communication signal is no longer on a carrier of increasing frequency but ideally on a frequency carrier relative to the employed baseband. Since some frequency and phase offsets might have existed during the mixing process, DFT and averaging procedures on the examined preamble can be applied to compensate for the aforementioned offsets [Win18]. After

54

(a)

(b)

(c)
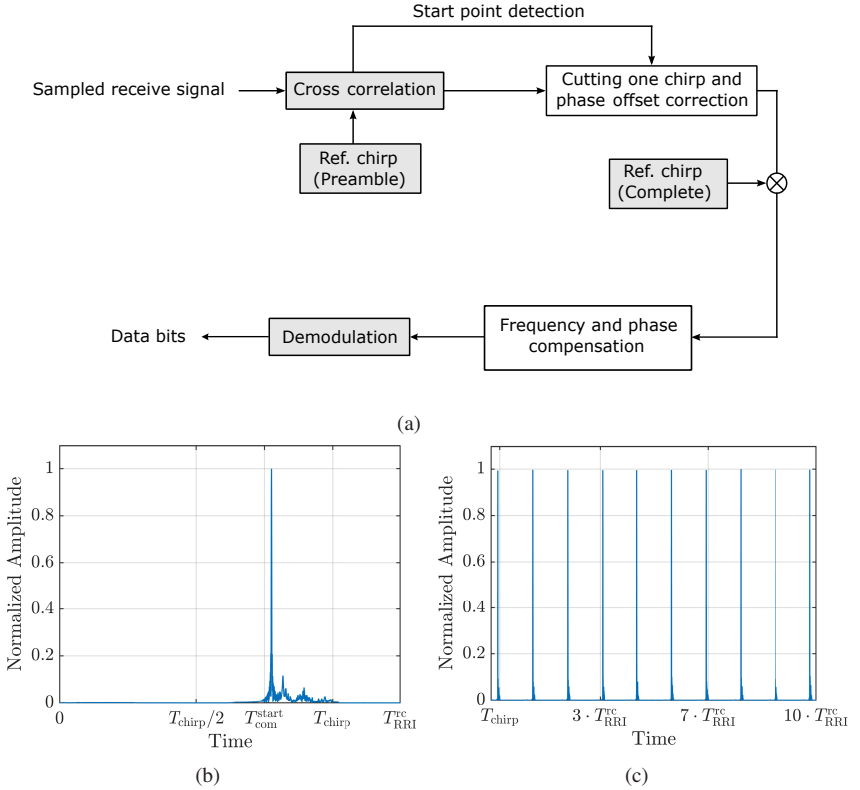
Fig. 3.6: Demodulation procedure of the communication data for PM-based modulation. (a) Demodulation block diagram, including start point detection, frequency, and phase offset compensations. (b) A significant peak according to the detection of the beginning of the communication section $T_{\text{com}}^{\text{start}}$ in an individual chirp. (c) A sequence of ridges at the output of the correlator, where each peak belongs to one preamble section within the examined chirp [Win18].

applying the detection procedure, the performance of the proposed communication method can be verified by two metrics. The achieved symbol rate can reflect the efficiency relative to the data transfer between communicating nodes. In this context, $N_{\text{com}} = N_{\text{samp}}$ represents one communication symbol per

sample within the modulated section of B_{com}. The symbol rate ($\mathcal{R}_s \in \mathbb{R}_+$) as well as the bit rate ($\mathcal{R}_b \in \mathbb{R}_+$) are given w.r.t the modulation order $\mathcal{M}$ by

$$\mathcal{R}_s = \frac{N_{com}}{T_{RRI}^{rc}} \tag{3.7}$$

$$\mathcal{R}_b = \log_2(\mathcal{M}) \cdot \mathcal{R}_s \tag{3.8}$$

For $N_{com} = 64$, $T_{RRI} = 10.1\,\mu s$ and QPSK modulation scheme with $\mathcal{M} = 4$, the $\mathcal{R}_s \simeq 6.34\,\text{MBd/s}$, and $\mathcal{R}_b \simeq 12.68\,\text{Mbit/s}$. However, the radar sensors do not send for the whole time cycle. Therefore, the achieved data rates can be reduced by the cycle factor. If $C\mathcal{R} = 50\,\%$ is adopted, the rates are halved.

Furthermore, the BER is an essential metric for evaluating the performance of communication systems in terms of the number of transmitted bits. For this purpose, BER has been presented in terms of the QPSK modulation scheme but can be employed by other modulation schemes for the same evaluation. The BER for QPSK can be calculated by computing the probability of error for each symbol over all possible symbols. The probability for each symbol depends on the distance between the decision boundaries and the noise level. If d_{dist} is the distance between the decision boundaries for QPSK modulation, and σ_{awgn} is the standard deviation of the Gaussian noise. Then, the probability of bit error for a given symbol state can be expressed as [PS07]

$$\mathcal{P}_s = Q\left(\frac{d_{dist}}{\sigma_{awgn}}\right), \tag{3.9}$$

where $Q(x)$ is the cumulative distribution function (CDF) of the standard normal distribution, which gives the probability that a random variable takes a value greater than x. Since QPSK has four equally probable symbol states, the average probability of bit error can be expressed as:

$$\mathcal{P}_b = (1/2) \cdot \mathcal{P}_s = Q\left(\frac{2E_b}{N_0}\right) \tag{3.10}$$

The results concerning BER and QPSK constellation diagram are shown further in Section 3.2.3.

- *Channel Equalization*

Millimeter wave (mmWave) technology has been acknowledged by the International Telecommunication Union (ITU) and the 3rd Generation Partnership Project (3GPP). Both organizations have designated specific frequency bands for mmWave communication, as outlined in ITU-R M.2412 [IT17], and 3GPP TR 38.901 [3GP22] within the frequency range of $(0.5 - 100)$ GHz. Simulation tools are necessary to develop communication systems to evaluate performance and adjust suitable parameters. QuaDRiGa (Quasi Deterministic Radio Channel Generator) has emerged as a recommended simulation tool concerning its ability to generate practical channel models in mmWave bands, wherefore a dual mobility scenario is adopted to emulate real-world scenarios [BJEPC14]. In addition, empirical measurements offer an opportunity to capture the actual characteristics of real-world channels. Therefore, the measurement setup from Chapter 2 is modified to support the investigation in this chapter.

Apart from that, the modulation of communication symbols is accomplished within a limited transmit signal bandwidth, utilizing the CS-based signal outlined in this chapter and detailed in previous subsections. Despite the narrow bandwidth employed for communication, the channel can influence the signal, resulting in time and frequency shifting of the received signal. Hence, estimating and equalizing the channel to guarantee reliable vehicle communication is crucial. For instance, pilot signals are traditionally included in OFDM systems to equalize the payload data using the same transmit sequence to equalize the channel effects [CEPB02], [HW98]. Based on the chirp signals discussed in this chapter, this section proposes a preamble-based method for estimating the impact of channel effects on CaCS-based systems using a single-carrier scheme [KKI08]. A preamble consisting of multiple chirps is sent beforehand, without any communication data, where the initial chirps serve for synchronization purposes, as explained in the subsequent chapter, and the final two chirps are utilized for analyzing the behavior of the channel. Consequently, the channel effects are equalized through a correlation-based approach, and the performance is evaluated in detail based on BER in Section 3.2.3.

For evaluation, a set of unmodulated chirps are sent at the beginning of the transmit sequence as a preamble to estimate the behavior of the channel and compensate it in the equalization step further. The received signal is filtered according to the allocation of the blue section in Fig. 3.3 and 3.4, where $t \in [T_{\text{um}}, T_{\text{chirp}})$. Next, the filtered signal is converted to the digital domain and sampled, and its nth element can be written as

$$y_{q_{\text{rc}},n}^{\text{com}} = \sum_{\iota=0}^{N-1} s_{q_{\text{rc}},\iota}^{\text{com}} \, h_{\langle n-\iota \rangle_N}^{\text{com}} + w_n^{\text{com}} \tag{3.11}$$

where $n, \iota \in \{0, 1, \cdots, N-1\}$, N is the number of samples, $\mathbf{y}_{q_{\text{rc}}}^{\text{com}} \in \mathbb{C}^{N \times 1}$ is the received signal vector related only to the communication section, and $\mathbf{s}_{q_{\text{rc}}}^{\text{com}} \in \mathbb{C}^{N \times 1}$ is the digital representation of the transmit signal vector after filtering it relying on (3.11). $\mathbf{h}^{\text{com}}$ is the channel impulse response vector related to the transmission, and $\mathbf{w}^{\text{com}}$ represents the noise vector. Furthermore, the behavior of the channel can be estimated using a bank of correlators, as shown in Fig. 3.7(a). The nth element of the correlator output, in this case, can be described as

$$\hat{h}_n^{\text{com}} = \sum_{\nu=0}^{N-1} y_{q_{\text{rc}},\nu}^{\text{com}} \, g_{\langle n-\nu \rangle_N}^{\text{ref}} \tag{3.12}$$

where $\nu \in \{0, 1, \cdots, N-1\}$, $\hat{\mathbf{h}}^{\text{com}} \in \mathbb{C}^{N \times 1}$ is the estimated channel vector related to the communication section, and $\mathbf{g}^{\text{ref}} \in \mathbb{C}^{N \times 1}$ represents the reference signal vector, which has been used by the correlator according to the upper part of the modulated chirp. As soon as the channel impulse response is estimated, the influence of the channel on the communication section can be equalized w.r.t $\hat{\mathbf{h}}^{\text{com}}$ by applying a correlation operation to the next transmit chirps transmitted after the preamble. Assuming the same signal to represent the received signal that carries the communication symbol, the equalization process is equivalent to the following equation

$$\rho_n^{\text{com}} = \sum_{o=0}^{N-1} y_{q_{\text{rc}},o}^{\text{com}} \left(\hat{h}_{\langle n-o \rangle_N}^{\text{com}} \right)^* \tag{3.13}$$

(a)   (b)
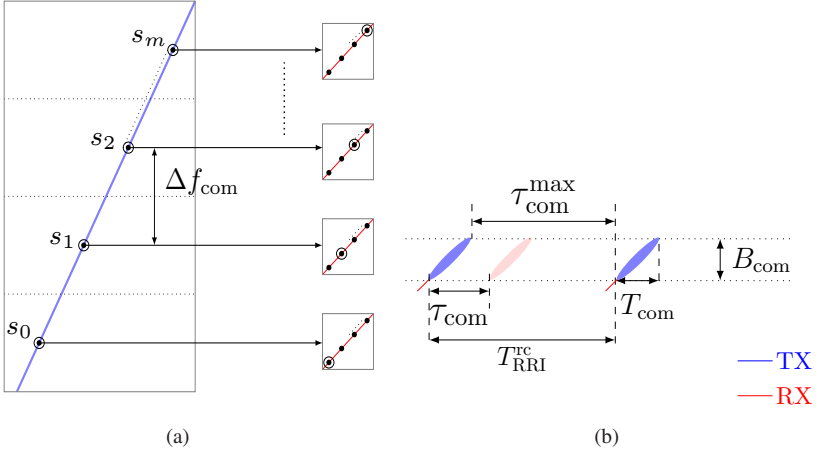
Fig. 3.7: Communication signal in the time-frequency plane for channel equalization. (a) Partially
modulated chirps of the proposed scheme with an exemplary distance between communi-
cation symbols Δf_{com}, where s_m represents the investigated communication symbol w.r.t
the correlation procedure. (b) Illustration of the maximum delay $\tau_{\text{com}}^{\text{max}}$ allowed during the
transmission compared to τ_{com}, T_{com} and $T_{\text{RRI}}^{\text{rc}}$ [AGdON+24].

where $o \in \{0, 1, \cdots, N-1\}$, ρ_n^{com} is nth element of the output of the correlator
relative to the transmit communication symbols, and the correlation, in this
case, is equivalent to a zero-forcing (ZF) equalizer in the frequency domain.
Furthermore, concerning the effects of the channel length, Fig. 3.7(b) illustrates
the distribution of the communication symbols based on the PM scheme [AN-
WZ19]. Given four communication symbols with a complete duration of T_{com},
the distance between the center frequencies of neighboring modulated sub-
sections of the communication section of the transmit signal in the frequency
domain is Δf_{com} and their distribution is depicted in Fig. 3.7(b). Besides, the
number of samples concerning the length of the channel impulse response ap-
plied during the transmission is given by $N_{h^{\text{com}}} = \tau_{\text{com}}^{\text{max}}/T_{\text{s}}$. In this term, τ_{com} is
the delay of the communication channel h^{com}, and T_{s} is the sampling duration.
As shown in Fig. 3.7, the equivalent channel length in samples $N_{h^{\text{com}}}$ can not
exceed $\tau_{\text{com}}^{\text{max}}/T_{\text{s}}$, which represents the distance between two successive chirps in
samples, otherwise, intersymbol interference (ISI) between the communication
symbols transmitted from different chirps can occur and affect the performance

of the transmission. For the QPSK modulation scheme, the BER can be derived relative to the channel influence on the communication symbols from the equation

$$
\mathrm{BER}_{\mathrm{QPSK}} = Q\left(\sqrt{2(Eb/N_0)_{\mathrm{QPSK}}}\right), \tag{3.14}
$$

where E_{b} is the bit energy and N_0 is the noise power density. Based on the correlational method derived from ZF equalizer, the equalization pursues to minimize the effects of the channel [GdO$^+$21], [LP03a], [LP03b], [OM21]. Therefore, the equivalent $(E_{\mathrm{b}}/N_0)_{\mathrm{QPSK}}$ can be calculated as

$$
(E_{\mathrm{b}}/N_0)_{\mathrm{Corr,QPSK}} = \frac{P^{\mathrm{Tx}}_{\mathrm{symb}}\, N_{\mathrm{symb}}}{\frac{1}{(N_{\mathrm{symb}})^2}\sum_{n=0}^{N_{\mathrm{symb}}-1}\frac{N_0}{|h^{\mathrm{com}}_{n,\mathrm{symb}}|^2}}, \tag{3.15}
$$

where $P^{\mathrm{Tx}}_{\mathrm{symb}}$ and N_{symb} are the transmit power for the transmit communication symbol and the number of samples per bit respectively, and $h^{\mathrm{com}}_{\mathrm{symb}}$ is the channel response at the transmit communication symbol.

3.2.2 Time Frequency Shift Keying

Another possible solution to modulate the communication symbols within radar signals without additional hardware is to employ LoRa communication schemes based on the CSS approach. This scheme is adopted in several systems due to its energy efficiency based on regional standards, such as the ISM band $(433.05\,\mathrm{MHz} - 434.79\,\mathrm{MHz})$) and the SRD band $(863\,\mathrm{MHz} - 870\,\mathrm{MHz})$) in Europe. In LoRa, the chirps can be divided into two sub-chirps based on predetermined time and frequency shifts in the time-frequency plane. Each unique combination of time-frequency shifts represents a distinct communication symbol. A spreading factor, similar to CSS, determines the number of individual communication symbols formed through various pair shifts. For CaCS-based radar systems, a novel technique inspired by the LoRa scheme is used for radar and communication integration. However, this technique is derived independently from the spreading-factor theory mentioned above [AdOGN$^+$20], [A$^+$22a]. In this sense, if the transmitter employs a chirp, the same signal can be used for radar detection and communication with nearby sensors. The PLL mentioned
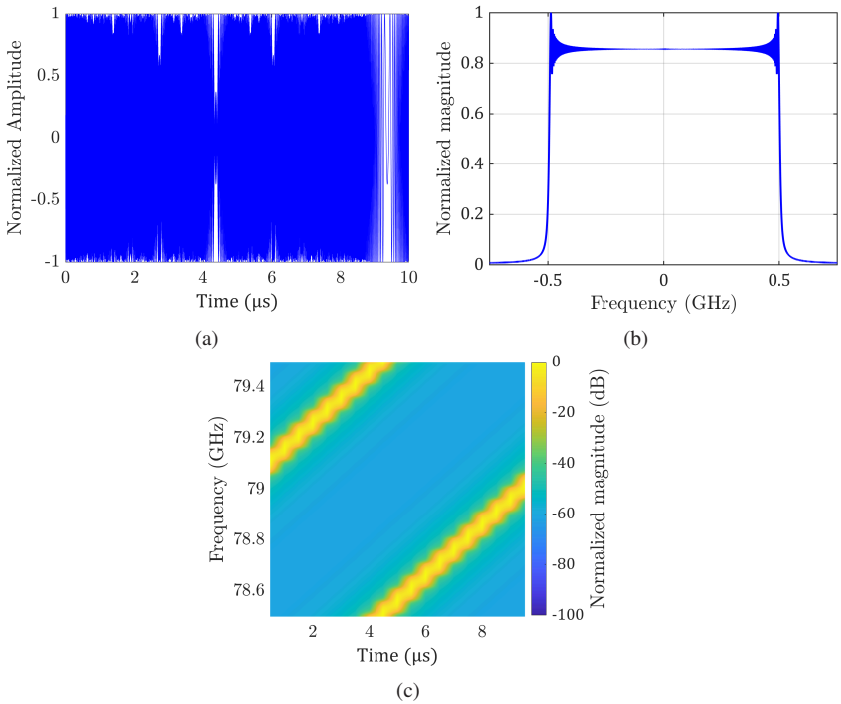
Fig. 3.8: Visualization of one interval of TFSK-based modulation according to the following parameters: $T_{\text{chirp}} = 10\,\mu s$, $f_c = 79\,\text{GHz}$, and $B = 1\,\text{GHz}$. (a) The representation of the signal (baseband) in the time domain. (b) The proposed signal in the frequency domain. (c) Spectrogram of the proposed waveform using STFT in the time-frequency plane.

in Chapter 2 to generate the signal at the transmitter side can be programmed to create communication symbols by dividing each chirp into two sub-chirps based on the communication data required for transmission.

Fig. 3.8 shows a chirp signal with a frequency that changes linearly over time and is divided into two sections using LoRa techniques. The time domain representation of the chirp can be seen in Fig. 3.8(a). Additionally, the formation of the chirp in the frequency domain can be obtained by applying Fourier Transform (FT) to the signal, as demonstrated in Fig. 3.8(b). This depiction contains multiple frequency components based on the bandwidth covered, and

it is equivalent to the one shown in Fig. 2.2 due to the specific characteristics of the chirp signal. Considering the time and frequency domains, the chirp can be visualized on a time-frequency plane by applying STFTs with an adjusted window. This visualization is called the spectrogram, as shown in Fig. 3.8(c). The spectrogram of a chirp exhibits a characteristic ($\backslash\!\!/$) shape that represents the linear increase in frequency over time in the two separate sections.

Waveform design

In the time domain, the continuous time signal $x_{q_{rc}}(t)$ transmitted for enabling both radar and communication properties can be characterized as

$$
x_{q_{rc}}(t) =
\begin{cases}
A \cos\left(\pi\mu\left(t - q_{rc}T_{RRI}^{rc}\right)^2 + 2\pi\left(f_c - \frac{B}{2} + f_1\right)t + \varphi_0\right), \\
\quad t \in [q_{rc}T_{RRI}^{rc}, q_{rc}T_{RRI}^{rc} + t_1) \\[2mm]
A \cos\left(\pi\mu\left(t - q_{rc}T_{RRI}^{rc}\right)^2 + 2\pi\left(f_c - \frac{B}{2}\right)t + \varphi_0\right), \\
\quad t \in [q_{rc}T_{RRI}^{rc} + t_1, q_{rc}T_{RRI}^{rc} + T_{chirp}) \\[2mm]
0, \\
\quad t \in [q_{rc}T_{RRI}^{rc} + T_{chirp}, (q_{rc} + 1)T_{RRI}^{rc})
\end{cases}
\tag{3.16}
$$

The desired communication symbol is represented by a frequency shift f_1 in one chirp within the time duration T_{RRI}^{rc}, while all other chirp parameters remain the same as in (3.7). Furthermore, the time shifts concerning the desired communication symbols are given by $t_1 = m \cdot T_{chirp}/f_1$, where $m \in 0, 1, \ldots, \mathcal{M}$ is the fractional factor of the modulated chirp and $\mathcal{M}$ is the number of unique assigned communication symbols for the transmission (modulation order). In automotive scenarios described in Section 2.3, a sequence consisting of multiple chirps Q_{rc} with index $q_{rc} \in \{0, 1, \ldots, Q_{rc} - 1\}$ and time duration T_{seq}. These chirps are combined with short time spacing T_p, whereby chirp in the sequence represents a communication symbol, determined by the assigned time and frequency shifts $\{(t_1, f_1)\}$ within the analyzed bandwidth B, as shown in Fig. 3.9.
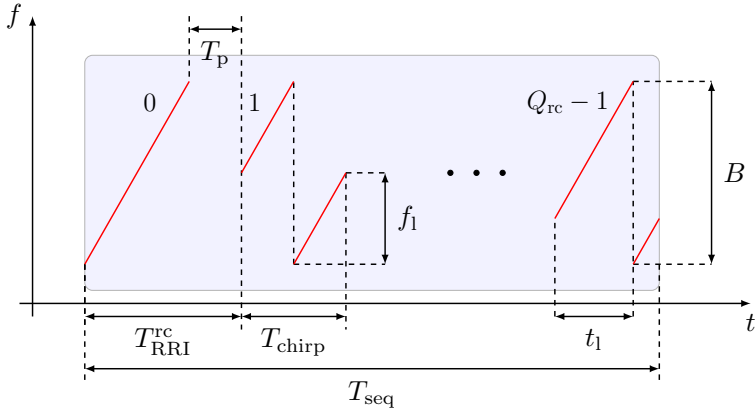
Fig. 3.9: CS representation with time duration T_{seq}. Q_{rc} is the number of interval with a time duration T_{RRI} for each. Each interval encompasses a chirp with time duration T_{chirp} and a pause interval T_P, and it spans over bandwidth B. t_l and f_l are the time and frequency shifts utilized for communication symbols [A$^+$22a].

Radar Functionality

A conventional 2D-FFT scheme is utilized in Section 2.3 to calculate the range and Doppler of the targets in the surrounding area. Nevertheless, the conventional 2D-FFT scheme fails to meet the accuracy criteria for estimating target parameters due to the radar signal modulation illustrated in Fig. 3.9, where the division of each chirp leads to a reduction in the beat frequency f_{beat} based on the transition between the two sub-chirps. Consequently, to ensure accurate range estimation, this section must be eliminated concerning the maximum estimated range R_{unamb}^{max} in the system. Besides, the phase of the downconverted chirps can become distorted due to the exchange of Doppler frequencies between the two sub-chirps, resulting in degraded Doppler estimation. Therefore, a novel adaptation of the 2D-FFT scheme is conducted within this framework to address the distortion in the analysis of ranges and velocities of the investigated targets.

The structure of the radar signal processing scheme is explained in Fig. 3.10. The upper part of the illustration shows the transmitting and receiving chirps in red and blue, respectively. The middle part depicts the maximum beat frequency
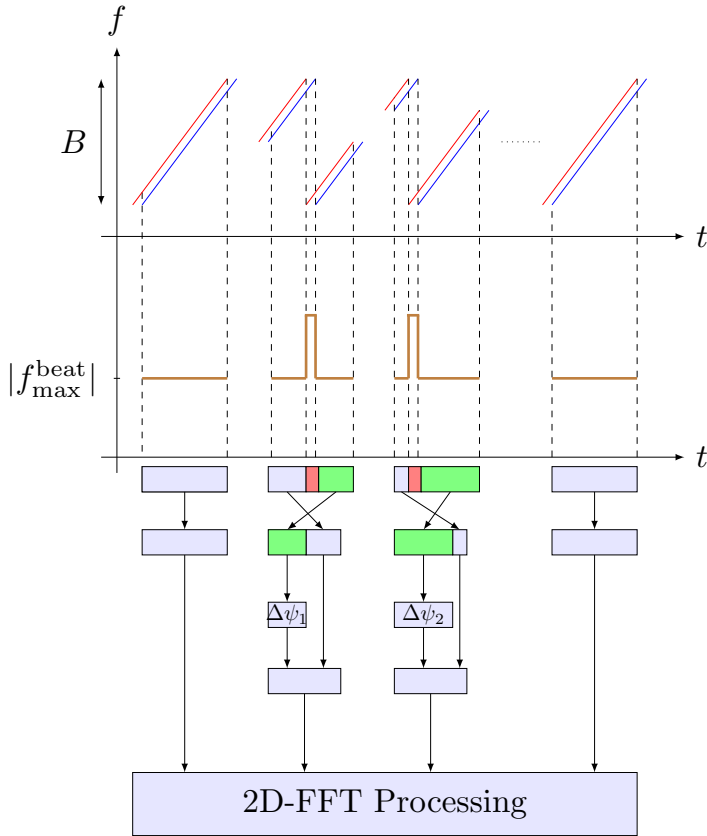
Fig. 3.10: Modified radar signal processing approach for TFSK modulation. Red-colored chirps represent the transmit signal, while blue-colored are the received counterparts. After downconversion, Blue sections involve no phase distortion, in contrast to the green. $\Delta\psi_m$ is the phase correction applied to the green sectors. Red-colored sections should be eliminated because of the transition between the two sub-chirps [AdOGN+20].

$f_{\max}^{\text{beat}}$ based on the evaluated range $R_{\text{unamb}}^{\max}$ after downconversion. In Fig. 3.9, the proposed waveform structure is shown, where a specific part of the signal cannot be accurately estimated within the time duration $\tau_{\max}$, resulting in a

phase distortion due to the transition swap. To address this phase misalignment, a correction method involving the rearrangement of the two contributive beat frequencies based on the sampling frequency and a phase correction factor (PCF) has been implemented on the radar IF signal [NKY17], [AdOGN+20]. When multiple communication symbols with unique time and frequency shifts are present, $\mathcal{M}$ correction factors must be used in the 2D-FFT, as demonstrated in Fig. 3.10. The lower part of Fig. 3.10 illustrates the proposed scheme after downconversion using an ADC. The blue sections represent accurate samples that do not require corrections, while the green sections suffer from misalignments due to different time shifts. The red sections, on the other hand, should be eliminated due to their biased beat frequency. The discrete mathematical expression of the pre-processing mentioned above in the baseband can be defined as

$$z_n^{\text{corr}} = \mathcal{F}^{-1}\left(\mathcal{F}\left[z_n^{\text{IF}}\right] \cdot \exp\left\{-\mathrm{j}\left[\Delta\psi_m T_{\text{chirp}}\right]\right\}\right), \tag{3.17}$$

where $\Delta\psi_m \in \{\psi_1, \psi_2, \cdots, \psi_{\mathcal{M}}\}$ denotes the phase correction factor depending on the various communications symbols, s_{IF} represents the intermediate frequency signal after the downconversion, and $\mathcal{F}(\cdot)$, $\mathcal{F}^{-1}(\cdot)$ refer to Fourier transforms and its inverse, respectively.

According to the structure of the suggested waveform in the previous section, a disadvantage relevant to the PLL features arises. The transition between the two parts of one communications symbol (within a single chirp) might not be precise, leading to some distortion in phase for the signal processing hereafter, which is exhibited as disparate pauses between successive chirps [AdOGN+20]. However, using direct digital synthesis (DDS) to generate the signal can preserve the specifications of the proposed CaCS-based waveform. Another drawback concerns the maximum detectable unambiguous range $R_{\text{unamb}}^{\text{max}}$ of the radar, which is relative to the duration of the chirp. In this case, the $R_{\text{unamb}}^{\text{max}}$ decreases compared to its counterpart regarding the traditional CS-based waveform as follows

$$R_{\text{unamb}}^{\text{max}} = \frac{c_0(T_{\text{chirp}} - \tau_{\text{tg}}^{\text{max}})}{2}, \tag{3.18}$$

where c_0 is the speed of light in vacuum and

$$\tau_{\text{tg}}^{\text{max}} = \frac{2R_{\text{unamb}}^{\text{max}}}{c_0}. \tag{3.19}$$

However, the aforementioned limitation can be critical in the case of long range radar (LRR) sensors and less crucial for short (SRR) and medium (MRR) sensors.

As explained in the last section, based on PM techniques, the RDM is a straight factor in evaluating the quality of radar detection. As presented in Chapter 2, the CS-based radar system with SISO architecture can estimate the range and velocity of the objects in the surroundings. From a signal-processing perspective, a 2D-grid map represents the delays and Doppler shifts caused by each target. In contrast to the PM technique, a transition in almost every chirp exists, which yields a distortion of the IF signal during the processing. Therefore, it is essential to consider the deteriorations that can occur in terms of RDMs and propose emending solutions for them, as shown further in Section 3.2.3. Moreover, based on the chirp division, this splitting disrupts the phase of the IF signal. By utilizing the adjusted 2D-FFT scheme to establish the RDM concerning the entities of the surroundings, the degree of inspected sidelobes grow in correlation with the phase disturbance that transpired at the IF stage. To accomplish this objective, PSLR and ISLR have been explored, as the elevation of both significant and minor sidelobes are evaluated in a single sample assessment.

Apart from that, although phase correction can rearrange the downconverted signal and reconstruct the phase of the two sub-chirps, the phase distortion can be intense in very high-velocity scenarios. In this framework, the phase at the edges of the two sections of the IF signal should be more examined to make the alignment in the time-frequency plane accurate. For this purpose, an additional scheme has been applied to cope with the intense phase distortions. For instance, the distorted signal part within the examined time interval can be eliminated and extrapolated to fix the flow between the two sections of the examined chirp [NUKY19]. Another approach adopted in this work is to extend the transmit signal with an additional part at the end to imitate the phase at the beginning due to the circular shift specification of the chirp in the time domain, as depicted in Fig. 3.11. If a section of the signal is sent at the end of the transmitted chirp, the phase of the desired IF signal can almost be preserved after downconversion without any distortion. In this context, the additional part
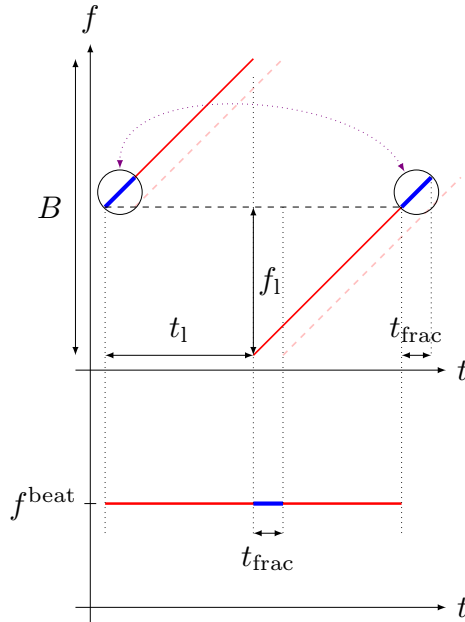
Fig. 3.11: The proposed method w.r.t very high-velocity scenarios. The transmit signal is extended by an additional section at the end of the chirp to imitate the phase at the beginning of the transmission. The transmit signal is marked with straight red, while the received counterpart is in dashed red and the additional parts are in blue.

should be eliminated from the processing scheme before applying FFTs to avoid distortions in the signal, which is adopted through the thesis.

Communication

This section delves into the design of the communication receiver for the TFSK method introduced to extend the radar signal with communication data. The communication receiver is designed to be dependent on the LoRa scheme. In this sense, the communication symbols are demodulated based on their assigned unique frequency shifts, similar to FSK. Besides, an adaptation for narrowband receiver systems is introduced based on pulse position modulation (PPM). The
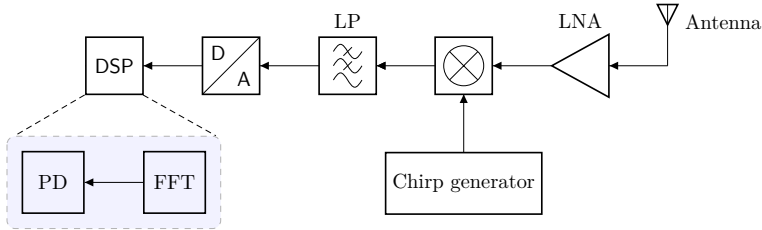
Fig. 3.12: Block diagram of the communication receiver at one CaCS node for TFSK-based modulation dependent on power detection (PD) [AdOGN+20].

latter architecture preserves the simplicity of the communication receiver and is identical to its counterpart for PM-based modulation in the analog domain.

- *LoRa-based Receiver*

LoRa modulation was initially developed for communication applications, but it has recently been adopted in radar applications, particularly in the 79 GHz frequency band [AdOGN+20], [A+22a]. This adoption has been commonly employed due to the similarities between LoRa and chirp signals used in radar systems. By merging the structure of LoRa waveforms in radar applications, it is possible to accomplish a dual-function capability, where the same signal can be appointed for communication and sensing purposes. In this context, the chirp can be transmitted to measure the specifications of the objects in the surroundings, besides representing communication symbols, which can be detected and demodulated by another CS-based radar system that occupies communication facilities. LoRa symbols can be received using various receiver architectures. Nevertheless, dependent on the hardware components in Chapter 2, a direct conversion approach is adopted, where the LoRa signal is directly downconverted to the baseband using a local oscillator and undergoes LP filtering to extract the LoRa communication symbols. According to the detection of LoRa symbols in [FA18], the demodulation method of the proposed CaCS-based waveform depends on the detection of distinctive peaks generated in the frequency domain. In Fig. 3.12, the processing chain of the communication receiver is shown. The modulated signal is initially downconverted by an unmodulated reference chirp to the IF domain. This approach is equivalent to the structure of the radar receiver applied for the detection. Next, the signal

is filtered and converted to be processed digitally using an ADC. After that, a DFT scheme is applied to distinguish every received symbol w.r.t the unique frequency index in the spectrum of every distinctive communication symbol based on its power. For the sake of simplicity, just four communications symbols based on the modulation order $\mathcal{M} = 4$ have been introduced throughout the study in [AdOGN+20], which supports the realization of the investigated concept using analog PLLs. According to [AdOGN+20], radar and communication measurements have been carried out for multiple targets and $\mathcal{M} = 4$ in an anechoic chamber at IHE to verify the proposed concept.

- *PPM-based Receiver*

PPM is an efficient modulation scheme for encoding digital information. It conveys information dependent on the position of the pulses in the time domain rather than their amplitude (PAM) or width (PWM) to send the desired information. Since the proposed TFSK method introduced in the previous section requires a high sampling rate at the receiver side if the communication symbols are adopted to spread among the whole transmit signal bandwidth as in the LoRa scheme $B = 1$ GHz. Therefore, the adjusted receiving procedure for PPM mainly depends on evaluating only a part of the received signal based on a correlation with a short reference chirp to reduce the costs. In this framework, a modified version of PPM regarding the study in [A+22a] to demodulate the communication data without adopting fast ADCs in the system (e.g., $B_{com} = B/10$) is assumed. Fig. 3.13 shows an exemplary adaptation of the CS-based frame dedicated to radar functionality to be received within a narrow bandwidth at the communication receiver of another CaCs node for PPM-based modulation. As shown in Fig. 3.9, A sequence of multiple chirps is sent within the duration T_{seq} consisting of Q_{rc} chirps with time repetition interval T_{RRI}^{rc}. The chirps are split and rearranged so that every chirp represents a communication symbol. The symbol detection at the CaCS-based receiver relies on the assigned frequency and time shifts f_l and t_l, which are specifically associated with the investigated communication symbol, as depicted in Fig. 3.13. In this context, the demand of the ADCs decreases proportionally with the factor B/B_{com} without reducing the number of the transmit communication symbols. Due to the modified receiving procedure within a limited bandwidth B_{com} compared with its counterparts in [AdOGN+20], the ADC applied at the receive side for this modulation scheme does not require identical specifications of the ADC adopted in [AdOGN+20], where the detection of the communication symbols is
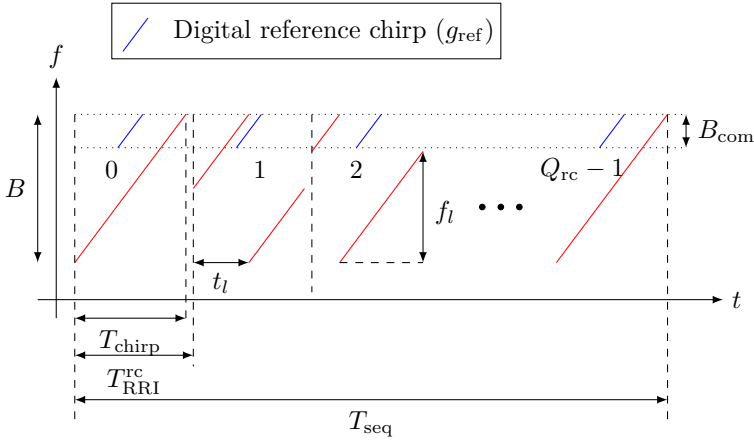
Fig. 3.13: The utilized signal applied for demodulating the data at the communication receiver: t_l and f_l represent the time and frequency shifts applied according to the investigated communication symbols, respectively. B is the bandwidth utilized for the complete signal, and B_{com} the bandwidth for communication. Red-colored chirps represent an example of the transmit signal, while the blue counterpart is the digital reference chirp g_{ref}, which the sampled communication signal is correlated with at the receiver [A⁺22a].

enforced in the frequency domain. In Fig. 3.13, the extracted signal is assumed to be localized in the upper part of the received signal (marked with black dashed lines). It is worth highlighting that the investigated signal for the communication can be defined at any position of the received signal except where it undergoes the transition. Apart from that, at the communication receiver of the CaCS system, the reflected signal, in its turn, undergoes amplification by an LNA and is mixed with the receiver communication frequency, as shown in Fig. 3.14. Next, the signal undergoes LP filtering to limit the required sampling rate used in the digital domain for detecting and demodulating the transmit symbols. If an IQ-mixer is adopted in Fig. 3.14, the cutoff frequency assigned to the filter should be $B_{com}/2$. After correlating the upper part of the transmit signal with a reference chirp with bandwidth B_{com}, the demodulation of the communication data relies mainly on the position dedicated to the pulses caused by the correlation. Fig. 3.15 depicts a simplified correlator implemented at the receiver side of the tested CaCS-node. The received signal $y_{q_{rc},n}^{com}$ is multiplied by its reference counterpart g_n^{ref} and integrated over the duration Δt_{ref},
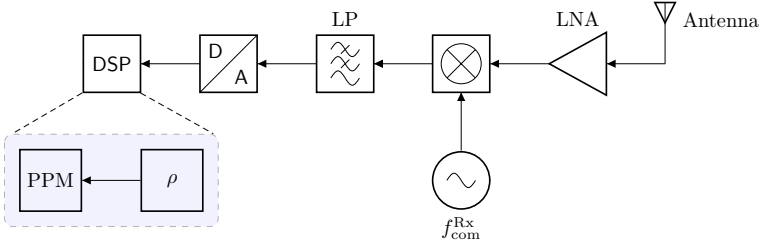
Fig. 3.14: Illustration of the block diagram of the communication receiver at one CaCS node for TFSK-based modulation dependent on PPM [A$^+$22a].

which distinguishes the employed communication symbols. Next, the absolute value of the signal is calculated to estimate the power of the attained pulses and decide to which symbol they belong. Finally, the obtained peaks are compared to the pulse position scheme proposed through the investigation.

The demodulation is presented by the pulse position detection corresponding to the unique position created from each communication symbol, which follows the concept of orthogonal signals. Orthogonal signaling is a type of modulation where the basis functions used for modulation are orthogonal to each other. This property enables efficient demodulation because of the orthogonality characteristics of the examined symbols. If noncoherent detection is adopted, the receiver can be designed flexibly but does not know the phase of the carrier signal [PS07]. In this term, the desired symbol follows Rician distribution and the other as interferer Rayleigh counterpart, where the distributions can be given as

$$P_{R_1}(r_1) = \frac{r_1}{\sigma_{\text{awgn}}^2} e^{-\frac{r_1^2}{2\sigma_{\text{awgn}}^2}}, \quad r_1 > 0 \tag{3.20}$$

$$P_{R_m}(r_m) = \frac{r_m}{\sigma_{\text{awgn}}^2} e^{-\frac{r_m^2 + K}{2\sigma_{\text{awgn}}^2}} I_0\left(\frac{r_m \sqrt{K_{\text{ric}}}}{\sigma_{\text{awgn}}^2}\right), \quad r_m > 0 \tag{3.21}$$

where $R_m = |r_\varsigma \cdot s_{m,\varsigma}|$, s_m is the m-th transmit symbol, r_ς is the received symbol, σ_{awgn}^2 is the noise power, K_{ric} is the Rician K-factor, and $I_0(\cdot)$ is the modified Bessel function of the first kind and order 0. If the symbol (1) is

71
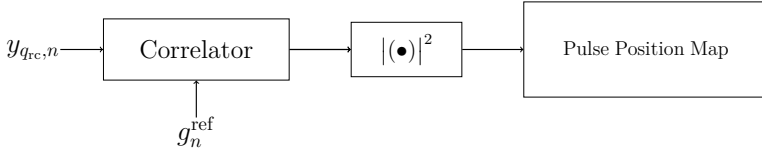
Fig. 3.15: Simplified structure of the correlator at the communication receiver of one CaCS-node [A$^+$22a].

tranmistted, $\mathcal{P}_c = P[R_2 < R_1, R_3 < R_1, \ldots, R_M < R_1]$ should be fulfilled to consider the events independent. After some mathematical manipulations as presented in [PS07]

$$\mathcal{P}_s = \sum_{m=0}^{M-1} (-1)^m \binom{M-1}{m} e^{-\frac{ms^2}{2(m+1)\sigma_{\text{awgn}}^2}} \int_0^\infty \frac{r_m}{\sigma_{\text{awgn}}^2} e^{-\frac{(m+1)r_m^2 + \frac{K_{\text{ric}}}{m+1}}{2\sigma_{\text{awgn}}^2}} I_0\left(\frac{r_m\sqrt{K_{\text{ric}}}}{\sigma_{\text{awgn}}^2}\right) dr_1 \tag{3.22}$$

Since the integral in the equation above can be represented as $1/(n+1)$, the probability of a correct decision can be

$$\mathcal{P}_s = \sum_{m=0}^{M-1} \frac{-1^{(m+1)}}{m+1} \binom{M-1}{m} e^{\frac{-m}{m+1}\frac{E_s}{2\sigma_{\text{awgn}}^2}}. \tag{3.23}$$

In this context, the probability of a correct decision of symbol error $SER = \mathcal{P}_{\text{err}}$ can be adopted as

$$\mathcal{P}_{\text{err}} = \sum_{m=1}^{M-1} \frac{-1^{(m+1)}}{m+1} \binom{M-1}{m} e^{\frac{-m\log_2(M)}{m+1}\frac{E_b}{2\sigma_{\text{awgn}}^2}}. \tag{3.24}$$

Apart from that, if Rayleigh multipath channel is adopted [SA05] based on (3.24), the channel effects can be merged in similar behavior in (3.15) as

$$\mathcal{P}_{\text{err}} = \sum_{m=1}^{M-1} \frac{-1^{(m+1)}}{m+1} \binom{M-1}{m} \frac{1}{1 + m\left(1 + \frac{\log_2(M)E_b|h_{\text{symb}}^{\text{com}}|^2}{2\sigma_{\text{awgn}}^2}\right)}. \tag{3.25}$$
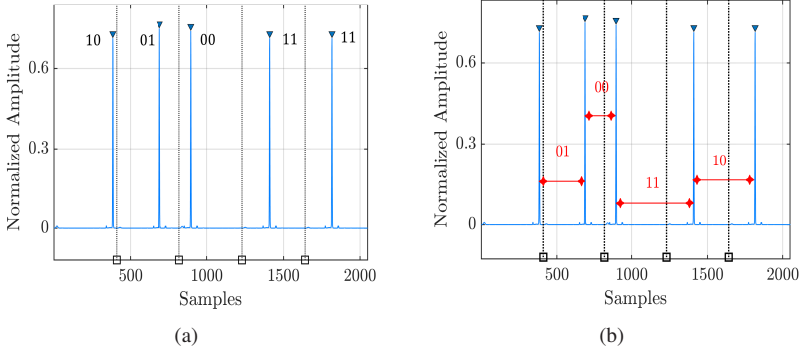
Fig. 3.16: Exemplary pattern of the peaks after applying the correlation at the communication receiver. (a) Conventional 4-PPM. (b) Differential 4-DPPM [A+22a].

After correlating the received signal with a reference chirp, a threshold level might be implemented to choose the pulse at the exact position. An exemplary pattern for the peaks at the receiver side and their equivalent communication data are shown in Fig. 3.16(a). However, detecting the absolute pulse position requires accurate time synchronization features. Therefore, differential detection can be applied, whereby the data are mapped to the distance between the pulses to represent each communication symbol by a unique interval between two received pulses. In this term, an exemplary pattern of the peaks at the receiver side is shown in Fig. 3.16(b).

3.2.3 System Verification and Results

This section presents a comprehensive evaluation of the CaCS-based radar system is verification process, which includes both simulations and measurements. The radar system operates at a frequency of 79 GHz and incorporates the innovative communication techniques and demodulation architecture described in previous sections for accurate target detection and data transmission. These assessments are carried out under well-defined conditions specified in Section 2.7 and with the adjusted parameters listed in Table 3.1. For this purpose, practical measurements are conducted in the laboratory of IHE, adhering to the specified setups based on the desired investigation for radar or communication and consi-

dering environmental factors in the surroundings (e.g., channel effects). These measurements encompass crucial radar performance metrics, including RDM plots and BER or SER curves with QPSK-constellation diagrams for PM-based modulation.

Table 3.1: System parameters of the proposed CaCS-based radar system.

Func.	Symbol	Parameter	Value
Radar	B	Chirp bandwidth	1 GHz
	f_c	Radar carrier frequency	79 GHz
	T_{chirp}	Chirp duration	10 µs
	T_p	Pause duration	$(0.1 - 10)$ µs
	T_{RRI}^{rc}	Ramp repetion interval	$(10.1 - 20)$ µs
	Q_{rc}	Chirps per sequence	1024
PM	B_{com}	Communication bandwidth	100 MHz
	B_{mod}	Modulated section	64 MHz
	B_g^u	Upper guard band	9 MHz
	B_g^l	Lower guard band	9 MHz
	B_{pre}	Preamble bandwidth	18 MHz
	f_{com}^{Rx}	Communications frequency	79.45 GHz
	N_{com}	Symbols per chirp	$\{8, 32, 64\}$
TFSK	N_{com}	Symbols per chirp	1

Range-Doppler Map

Fig. 3.17 depicts the radar images for conventional CS and its counterpart when the communication symbols are integrated. As shown in Chapter 2, CS-based

radar systems can simultaneously detect multiple targets in the environment in range and Doppler without any ambiguity as in FMCW-based radar systems. Although the communication data is integrated into the radar signal, it does not impact the detection of the targets examined in the scenario. In this term, Fig. 3.17(a) and Fig. 3.17(b) illustrate the RDM of multiple objects detected by the CS-based radar system. However, other figures visualize individual targets from the same RDM to precisely explore the impact of integrating communication data on the quality of the radar functionalities. Fig. 3.17(c) and Fig. 3.17(e) illustrate the detection of the targets based on conventional CS-based waveform without communication data. On the other hand, Fig. 3.17(d) and Fig. 3.17(f) depict the detection of the targets based on PM. In this term, the radar images are nearly identical, where the communication section has been discarded to increase the quality of the radar detection. However, the range resolution according to this condition decreases proportionally to the length of the discarded section, where $\Delta R = c/(B - B_{\mathrm{com}})$. It should be noted that other minor echoes exist around the target on the RDMs, as influenced by the measurement setup in the laboratory, which can cause multiple reflections of the desired signal (same Doppler bin) after propagation from the transmit antenna enacting several echoes with the same velocity but in different range bins. Therefore, two targets are detected according to the CFAR algorithm introduced in Section 2.5, and the additional reflection appears in both RDM for CS-based systems with and without communication symbols.

Furthermore, Fig. 3.17(g) to Fig. 3.17(j) depict the RDM for the TFSK-based waveform. According to the investigation held in Section 3.2.2, without adopting the PCF approach, the detected target appears as two peaks, which yield a loss in $\mathrm{SNR_{rad}}$ level that is partitioned and deteriorates the resolution in separating two targets, as illustrated in Fig. 3.17(g). Besides, one target emerges as two, which can be translated to false detection with proper levels of sensitivity of the radar system. On the other hand, as soon as the correction is implemented, the phase of the two sections of each chirp can be reconstructed, and the examined target emerges as one reflection in Fig. 3.17(h) compared to its counterpart in Fig. 3.17(g) so that the $\mathrm{SNR_{rad}}$ level can be preserved. However, the level of sidelobes increases due to the partition within the chirp. Moreover, Fig. 3.17(i) depicts the RDM in high-velocity scenarios. Although the PCF correction is adopted dependent on Fig. 3.10, the detected target also appears as two peaks, which yield a loss in $\mathrm{SNR_{rad}}$ level, that is partitioned and deteriorates the resolution in separating two targets. As soon as the adjustment of the scheme
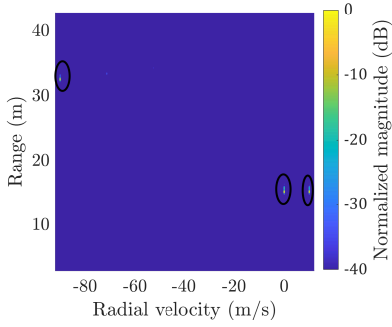
(a)
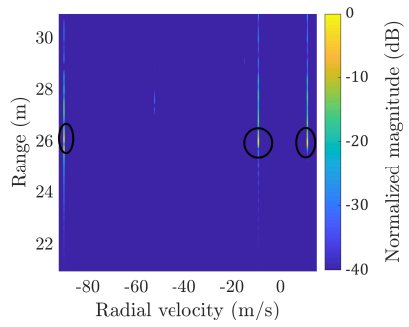
(b)
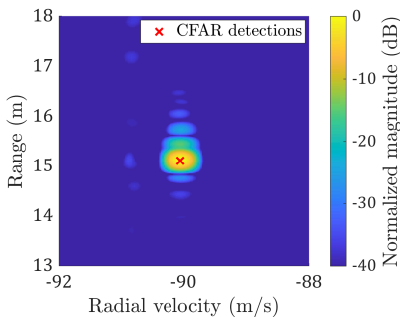
(c)
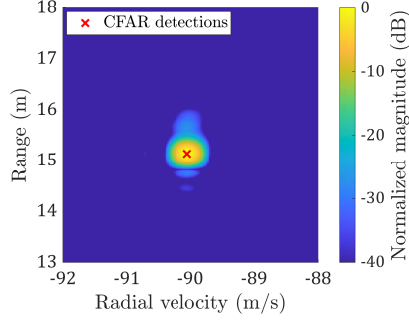
(d)
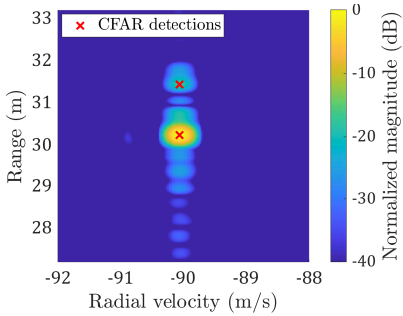
(e)
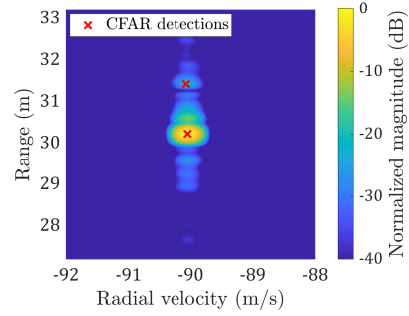
(f)
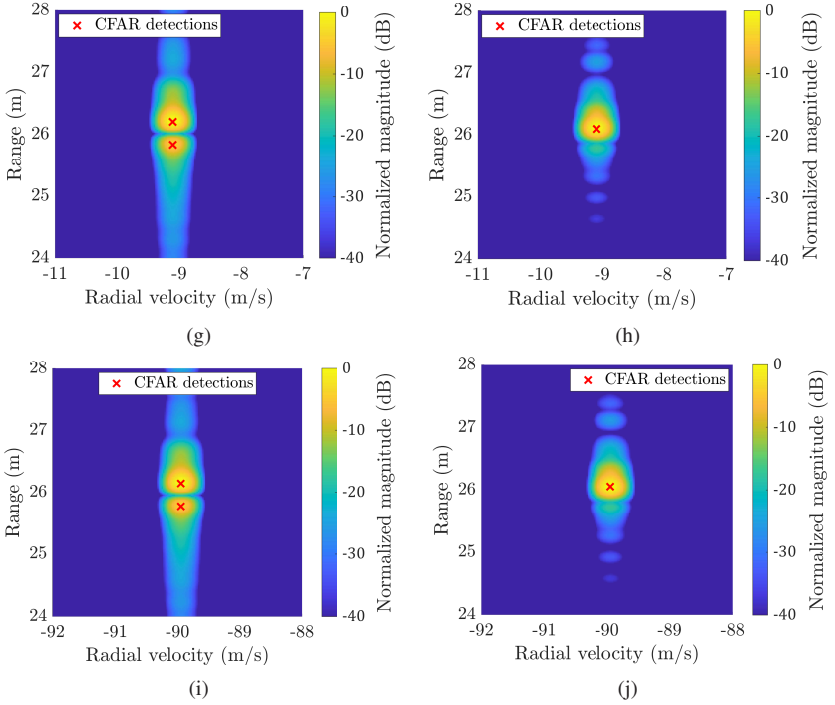
Fig. 3.17: The radar images of several targets with $P_f = 10^{-5}$ based on CFAR algorithm, as presented in Chapter 2. (a) RDM of a target $\{R_{\text{tg}} \simeq 15\,\text{m}, v_{\text{tg}} \simeq -90\,\text{m/s}\}$ based on conventional CS-based radar. (b) RDM for PM-based modulation and the same target in (a). (c) RDM of a target $\{R_{\text{tg}} \simeq 30\,\text{m}, v_{\text{tg}} \simeq -90\,\text{m/s}\}$ based on conventional CS-based radar. (d) RDM for PM-based modulation and the same target in (c). (e) RDM of a target $\{R_{\text{tg}} \simeq 26\,\text{m}, v_{\text{tg}} \simeq -9\,\text{m/s}\}$ based on TFSK modulation. (f) RDM for TFSK-based modulation and the same target in (e), but with PCF correction. (g) RDM of a target $\{R_{\text{tg}} \simeq 26\,\text{m}, v_{\text{tg}} \simeq -90\,\text{m/s}\}$ based on TFSK modulation in high-velocity scenarios. (h) RDM for TFSK-based modulation and the same target in (g), but with additional adjustment as in Fig. 3.11.

according to Fig. 3.11 is employed, the phase of the two sections of each chirp can be reconstructed, and the examined target emerges again as one reflection in Fig. 3.17(j) compared to its counterpart in Fig. 3.17(i) so that the SNR_{rad} level can be preserved.

PSLR and ISLR

Fig. 3.18 depicts the influence of the communication data on the integrated side lobe level. Although the level of PSLR does not change dramatically, as can be seen concerning PM-based modulation, the level of PSLR drops approximately 2 dB based on the radar image visualized in Fig. 3.18(a) for the same range bins if a fourth of the chirp is modulated. In other words, integrating communication data within the transmit radar signal yields a reasonable increment of the side lobes, as depicted in Fig. 3.18(a). Besides, the broader section within each chirp can be assigned for communication data, and more loss in ISLR can be caused since ISLR is more sensitive during one integral duration. Fig. 3.18(b) shows a comparison of ISLR for different $T_{com} \in \{T_{chirp}/16, T_{chirp}/8, T_{chirp}/4\}$. The increased modulation duration of every chirp results in a more significant influence on the ISLR level. Furthermore, Fig. 3.18(c) to Fig. 3.18(h) illustrate the variation in PSLR and ISLR levels according to the TFSK-based modulation compared to their counterparts for conventional CS-based schemes. Fig. 3.18(c) and Fig. 3.18(d) depict the impact of time shifts on the performance of PSLR and ISLR techniques, mainly the comparison focuses on different values for the time shift of the chirp duration T_{chirp}, which leads to an increased level of both values as soon as the shift increases. The analysis revealed distinct characteristics between PSLR and ISLR when subjected to different time shifts. For PSLR, the difference in level changes is almost constant between various time shifts. In contrast, ISLR demonstrated greater sensitivity to even slight time shifts, resulting in significantly increased levels, particularly beginning from $t_l = T_{chirp}/5$. However, if the correction of the RDM does not fit correctly in the frequency domain to the correct value, it can cause misalignment to the phase of the IF signal, leading to a drop in PSLR and ISLR values, especially in the middle of the velocity profile. In this context, the reduction above in PSLR and ISLR values depends on the frequency content of the IF signal and the associated time shift and suffers severe deterioration due to the main lobe degradation effect described in [GdOAN+22], as depicted in Fig. 3.18(e) and Fig. 3.18(f). Moreover, the mean value with its confidence interval (CI) has been calculated for different time shifts to quantify the overall error variations. The results indicated that as the time shift increases, both PSLR and ISLR undergo an increment in the mean error value. Additionally, the standard deviation of the error also increases, suggesting a higher variability in the ranging accuracy as the time shift deviated from the optimal value, as illustrated
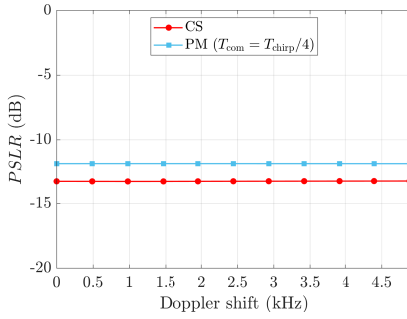
(a)
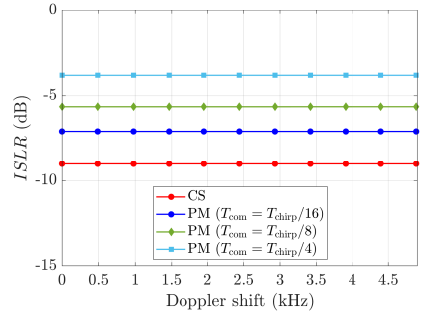
(b)
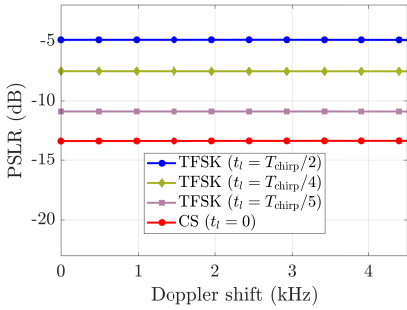
(c)
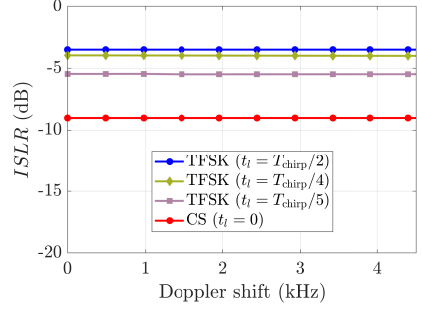
(d)
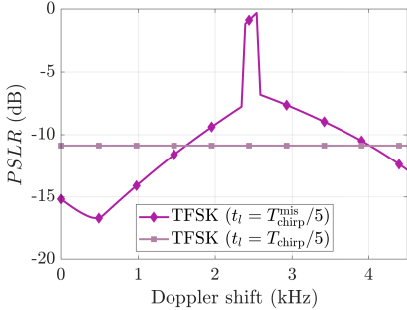
(e)
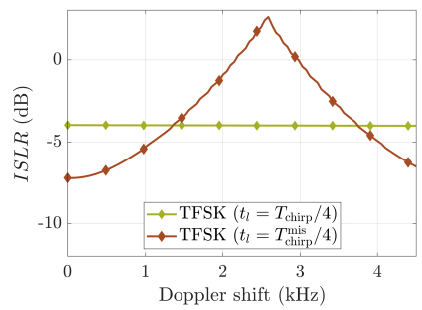
(f)
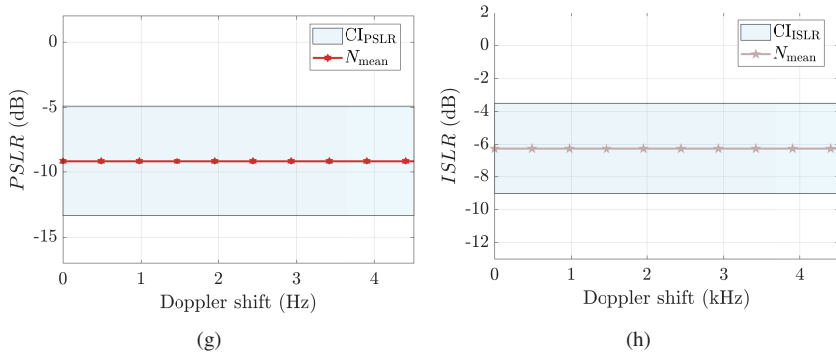
Fig. 3.18: PSLR and ISLR levels based on the detection of CS-based radar adopting conventional waveform, PM-based modulation, and TFSK of a target with $\{R_{tg} = 25\,\text{m}, v_{tg} = 30\,\text{m/s}\}$. (a) PSLR level of conventional CS-based waveform compared to its counterpart PM-based modulation ($T_{com} = T_{chirp}/4$). (b) ISLR level for different durations of $T_{com} \in \{T_{chirp}/16, T_{chirp}/8, T_{chirp}/4\}$. (c) PSLR level of conventional CS-based waveform compared to its counterpart TFSK modulation ($t_l \in \{T_{chirp}/5, T_{chirp}/4, T_{chirp}/2\}$). (d) $ISLR$ level for the same time shift in (c). (e) PSLR level misalignment based on $t_l = T_{chirp}^{mis}/5$. (f) ISLR level misalignment based on $t_l = T_{chirp}^{mis}/4$. (g) Mean value N_{mean}^{PSLR} of PSLR based on different time shifts and CI_{PSLR} for TFSK-based modulation. (h) Mean value N_{mean}^{ISLR} of ISLR based on different time shifts and CI_{ISLR} for TFSK-based modulation.

in Fig. 3.18(g) and Fig. 3.18(h). It should be mentioned that all the values in Fig. 3.18 have been taken in dB, which means that $PSLR_{dB} = 20\log_{10}(PSLR)$, and $ISLR_{dB} = 20\log_{10}(ISLR)$, respcitvely. Furthermore, the x-axis is adjusted according to the maximum radial velocity detected by the CS-based radar system and located close to $50\,\text{kHz}$.

Setup Modification for Communication Measurements

The architecture of the measurement setup presented in Section 2.7 is adjusted to accord the investigation to communication analyses, as depicted in Fig. 3.19. At the core of this setup resides the RFSoC to generate signals that initiate the measurement process. Following the measurement chain, the signal can be emitted and captured by the measurement setup through the RF front end, which acts as an intermediary step managing the interface between the elec-
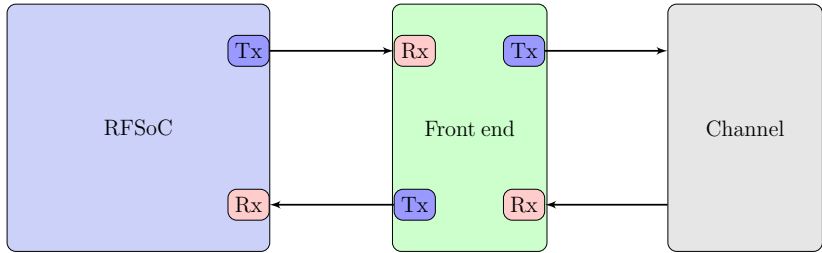
Fig. 3.19: Adjustment of the measurement setup according to the modulation scenario presented in this section. The RFSoC has represented both transmitter and receiver in the baseband among the measurements. The components of the front end are identical to their counterparts introduced in Chapter 2 and Appendix B.

tromagnetic wave and the physical medium for the frequency range of 79 GHz and its components introduced in Appendix B. On the receiver, the RF front end serves as a gateway to capture the echoes from the environment for further processing. Next, the signal is downconverted to the baseband at 1 GHz, enabling it to entail translating the high-frequency echoes into a lower-frequency range for further digital signal processing. Within the extent of the RFSoC, the downconverted baseband signal encounters an estimation of the influence of the channel on the examined signal. After that, the signal is equalized based on the channel estimation to extract the communication data transmitted from one node dependent on the adopted digital modulation scheme.

It is worth noting that the transmission is simulated through an AWGN channel and a dual mobility scenario from QuaDRiGa tool for PM technique, whether the measurements are conducted in one of the laboratories at IHE, as depicted in Fig. 3.20(a) and therefore has undergone some channel effects related to the setup and the distance between the transmitter and receiver up to 2 m. The channel imperfections are equalized with a correlation-based approach to minimize the error. In this context, the simulated and measured BER curves are illustrated in Fig. 3.20(b). The recovery of the transmitted communication symbols is provided when $N_{com} = 8$, $N_{com} = 32$ and in the case of $N_{com} = 64$, which assures the verification of the suggested equalization method. It should be mentioned that due to the limited number of samples assigned for each communication symbol, the curves deviate slightly when $N_{com} = 32$ and more if $N_{com} = 64$ compared to its counterpart when $N_{com} = 8$ [ANWZ19]. In

(a)

(b)

(c)

(d)

(e)   (f)
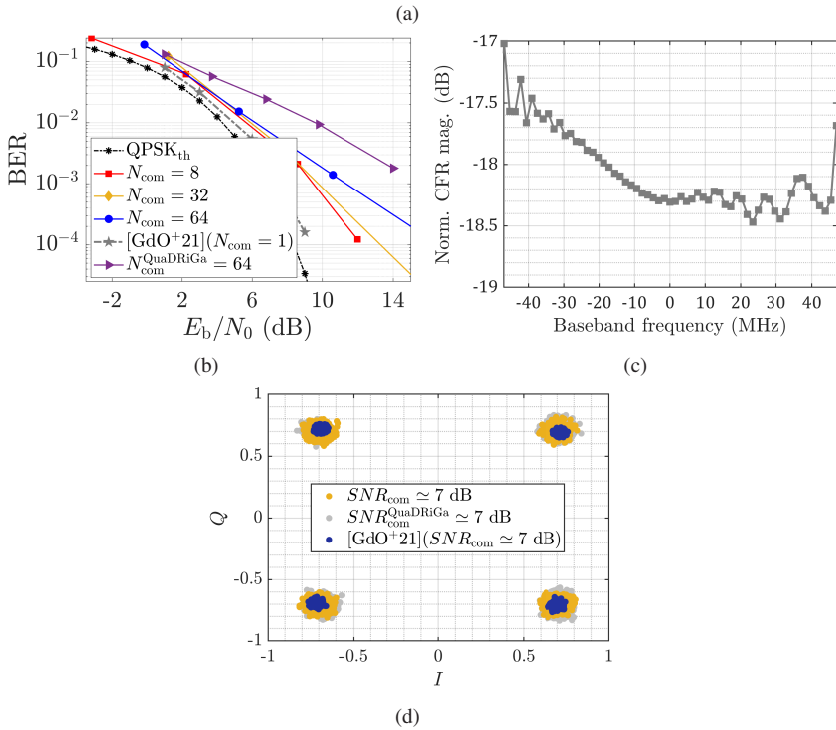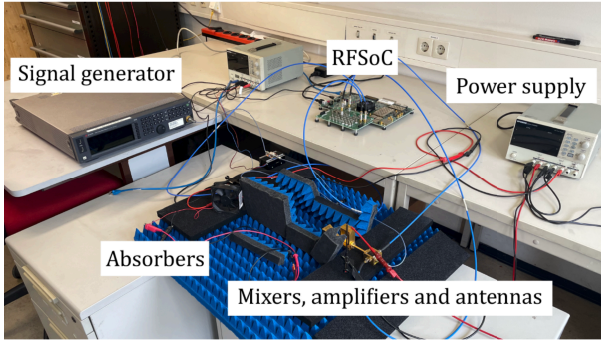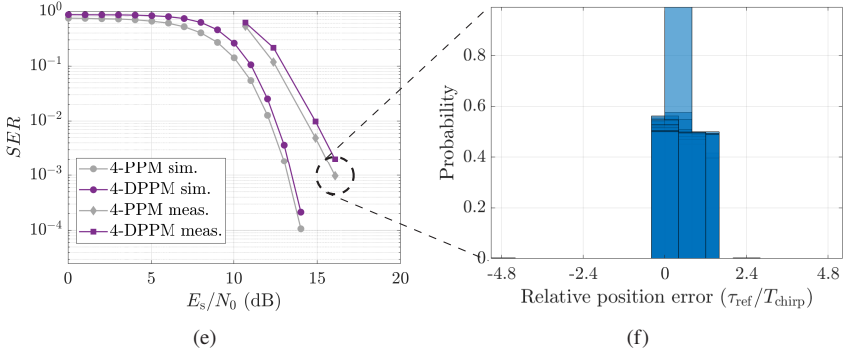
Fig. 3.20: Measurement and simulation results of the proposed method. (a) The measurement setup. (b) The simulated and measured BER curves for $N_{com} \in \{8, 32, 64\}$ based on PM. (c) Channel frequency response of the communication section regarding h_{com} and the constellation diagram of the QPSK scheme. (d) Constellation diagram of the QPSK scheme for $SNR_{com} \in \{7, 15\}$dB in communication scenarios compared to the theoretical case of QPSK$_{th}$. (e) Simulated and measured SER regarding conventional and differential 4-PPM with the same effects of the channel response derived in (c) and $N_{com} = 1$. (f) Correlator position error (τ_{ref}/T_{chirp}) [A$^+$22a], [AGdON$^+$24].

addition, Fig. 3.20(c) depicts the channel frequency response (CFR) applied to the communication section during the measurements, where its formation deteriorates according to the effects of higher frequencies experienced at the end of each chirp. Accordingly, Fig. 3.20(d) illustrates the constellation diagram of the QPSK modulation for different SNR$_{com}$ values compared to the theoretical counterpart. In this sense, the transmission can be successful by adopting SNR$_{com}$ and SNR$_{com}^{QuaDRiGa} \simeq 7$ dB.

In conjunction with TFSK-based modulation, RTS is adopted within the measurement setup to create additional virtual delays and frequency shifts, emulating more realistic communication scenarios within the laboratory environment, according to Section 2.7 and Fig. 3.20. After estimating and equalizing the channel effects, as explained for PM modulation, the communication data transmitted through the wireless channel are demodulated and compared with their counterparts before the transmission to generate SER curves, as illustrated in Fig. 3.20(e). Taking into account the parameters in Table 3.2, the equivalent achievable symbol rate can be calculated $R_s = N_{Com}/T_{RRI}^{rc} = 90$ kBd/s. Since the radar sensors do not send for the whole time cycle, the achieved data rates

can be reduced by $\mathcal{CR}$. For $\mathcal{CR} = 50\,\%$, the aforementioned rate is halved. Besides, Fig. 3.20(f) shows the overlapped outputs of the correlator from different measurements, where the decision error $\tau_{\mathrm{ref}}/T_{\mathrm{chirp}}$ is almost neglectable compared to the false decision case ($\tau_{\mathrm{ref}}/T_{\mathrm{chirp}} = 1$). In addition, if the differential decoding is employed, the first symbol is spared.

Table 3.2: Parameters of the differential decoding

Time difference	Value
$T_{\mathrm{chirp}}/4$	00
$T_{\mathrm{chirp}}/2$	01
$3 \cdot T_{\mathrm{chirp}}/4$	10
T_{chirp}	11

Link Budget and Achievable Communication Criteria

Based on the parameters above, the link budget of the communication scenario in automotive applications can be calculated for different transmit power $P_{\mathrm{com}}^{\mathrm{Tx}} \in \{0, 5, 10, 15\}$dBm. Fig. 3.21 illustrates the path loss factor PL_{com} and $\mathrm{SNR}_{\mathrm{com}}^{\mathrm{in}}$ level dependent on the distance between the communicating nodes. When the distance increases, the path loss escalates, and the $\mathrm{SNR}_{\mathrm{com}}^{\mathrm{in}}$ level decreases. Fig. 3.21(a) depicts PL_{com} dependent on the distance, while Fig. 3.21(b) shows the behavior of $\mathrm{SNR}_{\mathrm{com}}^{\mathrm{in}}$ adopting different values of $P_{\mathrm{com}}^{\mathrm{Tx}}$, corresponding to fixing other parameters. According to this assumption, the following values have been adopted $G_{\mathrm{Tx}} = G_{\mathrm{Rx}} = 10$ dB, $f_c = 79$ GHz, the noise figure $NF = 10$ dB, where PL_{com} and $\mathrm{SNR}_{\mathrm{com}}^{\mathrm{in}}$ level can be calculated without associated processing gain as

$$PL_{\mathrm{com}} = 20 \log_{10}\left(\frac{4\pi R_{\mathrm{com}}}{\lambda}\right), \tag{3.26}$$

$$SNR_{\mathrm{com}}^{\mathrm{in}} = \frac{P_{\mathrm{com}}^{\mathrm{Rx}}}{P_{\mathrm{N}}}, \tag{3.27}$$
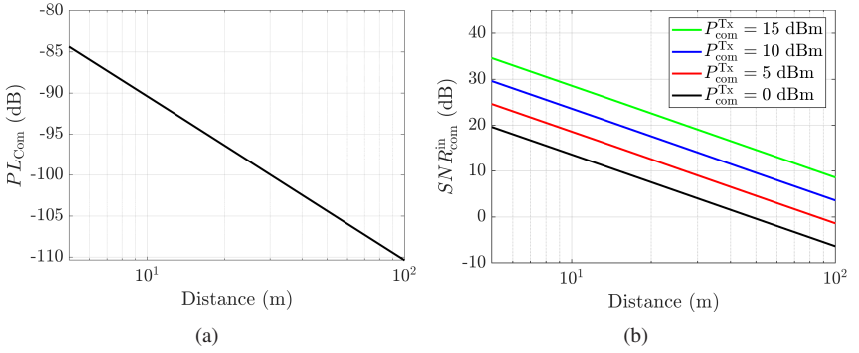
Fig. 3.21: Exemplary pattern of the link budget at the communication receiver based on the achieved distance. (a) Incident path loss. (b) $\text{SNR}^{\text{in}}_{\text{com}}$ level at the communication receiver without processing gain.

where P_N is the noise power and $P^{\text{Rx}}_{\text{com}}$ is the received counterpart given in Chapter 2. In summary, Table 3.3 demonstrates the output parameters of the investigated communication techniques presented in this chapter compared with a traditional communication technique in [GdO+21]. PM communication technique proposes a notable enhancement in data rate compared to its TFSK and conventional counterpart. This more elevated achievable data rate is connected with the number of communication symbols assigned per chirp. It should be noted that $T_\text{p} = 1\,\mu s$ and $C\mathcal{R} = 50\,\%$ are adopted in Table 3.3. Besides, in dual mobility scenarios within QuaDRiGa simulations, $T_\text{p} = 10\,\mu s$ is employed to conceal the potential long delay that occurred in the channel, which leads to a data rate of $\simeq 3.2\,\text{Mbit/s}$. Beyond data rate, Table 3.3 delves into additional performance metrics, such as the time duration set for communication within the radar signal. PM and TFSK communication techniques assign solely $10\,\%$ of the time compared to the proposed method in [GdO+21]. However, the sampling rate remains the same for all the communication techniques mentioned in Table 3.3. Furthermore, PM and TFSK techniques adopt a separate architecture for the communication receiver, granting more freedom within the design for both radar and communication procedures, in contrast to the study in [GdO+21], which employs the same transceiver for radar and communication. A correlation-based approach is adopted for the channel equalization for both PM and TFSK techniques since the chirps are downconverted with a single tone

at the communication receiver side, while the study in [GdO⁺21] suggested a matched filter approach, whereby the downconversion occurs by employing the transmit signal.

Table 3.3: Comparison of Communication Systems

Method	[GdO$^+$21]	PM	TFSK
f_s	100 MHz		
$\mathcal{R}_b$	$\simeq 90\,\text{kbit/s}$	$\leq 5.8\,\text{Mbit/s}$	$\simeq 90\,\text{kbit/s}$
N_{com}	1	$N_{com} \leq N_{samp}$	1
E_s	$\equiv (\Sigma\,N)$	≥ 1 Sample	$\equiv (\Sigma\,N)$
T_{com}	T_{chirp}	$T_{chirp}/10$	
Com Tx	+ Modulator		Radar Tx
Com Rx	Radar Rx	Separate	
Equalization	ZF	Correlation	
Scenario	LRR & MRR	SRR & MRR	LRR & MRR

3.2.4 Conclusion of this Chapter

This chapter analyzes PM and TFSK communication techniques to consolidate communication data into the radar signal. PM modulation partially integrates the communication data within the radar signal to preserve the quality of radar detection. Additionally, its ability to merge multiple communication symbols overcomes the conventional methods in the literature that either impact the radar measurements or limit the transmit data rate. It has been shown that one communication symbol per sample can be sent, and $\mathcal{R}_b \simeq 5.8\,\text{Mbit/s}$ can be achieved. However, PSLR and ISLR can deteriorate depending on the modulation duration, with $\simeq 2\,\text{dB}$, $6\,\text{dB}$ respectively for $T_{com} = T_{chirp}/4$. On the other hand, TFSK modulation represents the communication symbols by reforming the structure of the transmit chirps based on the LoRa scheme. This modulation technique demonstrates promising results according to the radar measurements and communication between the radar sensors in the surroundings. However, one communication symbol per chirp is sent, and the integration of communi-

cation data can cause an increment in PSLR levels, up to worse 6 dB compared with PM modulation if $t_l = T_{\text{chirp}}/2$. Throughout this chapter, a measurement setup with 79 GHz front end has provided empirical evidence supporting the effectiveness and applicability of both modulation methods for integrating communication within radar signals without significantly restricting radar capabilities. The insights gained from this chapter can contribute to the growing knowledge of RadCom concepts, facilitating advancements and innovations in the automotive sector so that further improvements can be made to their systems in the upcoming years.

4 Synchronization between Communication Nodes in CaCS-based Systems

This chapter discusses a chirp-like synchronization method in detail. The proposed method employs a sequence of up- and down chirps to estimate frequency and time offsets and supports mainly the modulation schemes in Chapter 3, particularly PM and TFSK modulations. Nevertheless, it can be adapted for similar systems that utilize chirp signals for communication and radar purposes.

The main milestones of this chapter are included in the following points. This chapter emphasizes the importance of ensuring synchronization in communication systems by schematically visualizing imperfect synchronization in the time and frequency domains relative to the QPSK modulation scheme. Next, a brief overview of the synchronization methods for shared radar and communication systems in the literature is performed, where the proposed synchronization in this work is reported in detail. Finally, the new approach is optimized and validated using numerical analysis and experimental measurements.

The aspects in this chapter are mainly based on the publication from [A+22b] with reused texts and figures © [2022] PIER C.

4.1 Analyses of Imperfect Synchronization

In communication systems, the data is transmitted from one node to another according to a predefined modulation scheme between the transmitter and receiver. Many communication systems adopt synchronous hierarchies at the receiver side, where the data flow has to be detected and recognized. Those systems can employ coherent detection algorithms and ensure several advantages in terms of bandwidth efficiency and noise performance compared with their
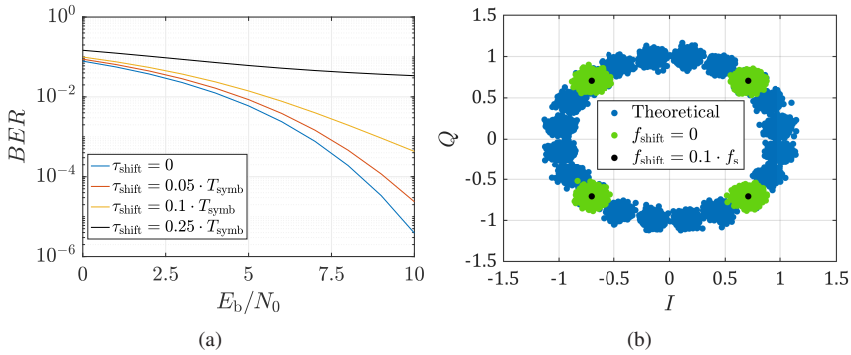
Fig. 4.1: Exemplary impacts of imperfect synchronization on the quality of QPSK communication. (a) BER deviation due to the shift in the time domain for 0, $\tau_{\text{shift}} = 0.1 \cdot T_{\text{symb}}$, $\tau_{\text{shift}} = 0.05 \cdot T_{\text{symb}}$, $\tau_{\text{shift}} = 0.1 \cdot T_{\text{symb}}$ and $\tau_{\text{shift}} = 0.25 \cdot T_{\text{symb}}$. (b) Constellation diagram of QPSK symbols with occurred frequency shifting $f_{\text{shift}} = 0.1 \cdot f_{\text{s}}$, without any shifts compared with the theoretical allocation of the four symbols.

noncoherent counterparts. However, if the synchronization is not guaranteed, a loss of information can occur, and the transmission quality drops equivalently. The synchronization analyses can be split into two groups concerning the time or frequency domain and differ in attainment according to the proposed communication system. Fig. 4.1(a) illustrates an exemplary synchronization error in the time domain for QPSK symbols. A slight deviation can lead to a deterioration in the performance of BER for different E_{b}/N_0 values. For instance, $\tau_{\text{shift}} = 0$ represents the case where no time shift has occurred, and the transmit symbols can be recovered correctly. However, for $\tau_{\text{shift}} = 0.1 \cdot T_{\text{symb}}$, the deviation in the performance drops to $\simeq 2.5$ dB, and for $\tau_{\text{shift}} = 0.25 \cdot T_{\text{symb}}$, BER can not achieve better than (8×10^{-1}), which emphasizes the importance of ensuring the accurate time allocation on the communication receiver. Furthermore, the influence of an exemplary frequency shift on the constellation diagram for QPSK has been shown in Fig. 4.1(b). A slight shifting in the frequency domain with the value $f_{\text{shift}} = 0.1 \cdot f_{\text{s}}$ can impact the distribution of the symbol within the constellation diagram. The figure shows this effect in blue compared with its counterpart in green when no shifting is present during the transmission. Both explained cases are plotted with the theoretical constellation for a better overview. As can be seen, synchronization has a significant role in communi-

cation systems with a view to the shared radar-communication schemes in the future.

4.2 Synchronization in Joint Radar-Communication Systems

In automotive applications, current radar sensors utilize waveforms based on CS-based waveforms to detect various targets in their surroundings [RBK$^+$19, HY19, WHM21]. This approach not only reduces the design complexity and manufacturing costs compared to other digital waveform techniques like OFDM and PMCW but also offers flexibility in applying signal processing algorithms based on the preferences of automotive suppliers. However, the existing standards governing the allocation of frequency bandwidths $(77-81)$ GHz for radar applications do not address the distribution of radar signals within this occupied bandwidth for specific time durations. Consequently, the absence of standardization in this regard can potentially impact the synchronization between communicating nodes and the demodulation process of communication data at the receiver side, particularly in systems where communication and radar functionalities coexist. Previous studies on integrating communication data in shared radar communication systems have focused on system-based models that rely on external systems specifically designed for this purpose, such as 5G and ITS-G5. In such cases, the synchronization between the communicating CaCS nodes is dependent, in this case, on an additional system used for communication, as well as an external source for accurate time synchronization, such as the Global Positioning System (GPS) and Global Navigation Satellite System (GNSS) [MX16], [ETS12]. On the other hand, signal-based systems modulate communication data within the transmit radar signals without using an additional framework for synchronization, resulting in RadCom systems [SW11], DFRC systems [GdO$^+$21], or CaCS radar systems [A$^+$22a]. Along with CaCS-based radar systems introduced in Chapter 3, the integration of the communications symbols within the radar signal can satisfy the hardware requirements of the current radar sensors in terms of the limited sampled bandwidth at the receiver side and achieve appropriate data rates for specific purposes such as interference mitigation between active radar sensors in the surroundings. In this context, a separate communication receiver is needed at the receiver node, or the radar receiver should be able to switch between the

two functionalities. However, the system requires a synchronization procedure to guarantee the correct demodulation of the data transmitted between the communicating vehicles [L+20].

Depending upon the aforementioned requirements, this work presents a novel image-like synchronization approach between CaCS nodes based on chirp signals. The proposed synchronization approach mainly supports the communication method introduced in Chapter 3 and can be adapted for equivalent systems that employ chirp signals, where the structure of the entire sequence is adjusted to achieve this goal, as is further shown in the next section.

4.3 System Model Including Synchronization Chirps

Considering the CS signal presented in Chapter 2 and the novel communication modulation methods presented in Chapter 3, a sequence of multiple chirps $Q \in \mathbb{N}_+$ with index $q \in \{0, 1, \ldots, Q - 1\}$ combined with short spacing is designed to estimate the RDM of different objects in automotive scenarios. In addition, every chirp enclosed in the sequence implicates an adequate amount of communication symbols located at the upper part of the chirp, as shown in Fig. 4.2, or by its division into unique pairs (TFSK-based modulation) to support the foundation of a communication link between the communicating vehicles in the milieu. Since the communication receiver is to be found in another CaCS node, a predefined synchronization procedure should be carried out to detect the communication section in each modulated chirp. This issue means that if there are any differences in the parameters used by the radar sensors at the transmitter and receiver, the carrier alignment of the communication receiver in the time-frequency plane may not match the transmit counterpart from the other CaCS node. This misalignment in the frequency domain, denoted as f_{shift}, causes the transmitted data to be incorrectly detected since the communication receiver can miss the modulation section dedicated to the transmitted symbols. To illustrate this, Fig. 4.2 shows an example of a frequency difference at the communication receiver side, where the unmodulated part of the transmitted chirp within $B_{\text{com}}^{\text{Rx}}$ is mistakenly extracted instead of the intended communication symbols within $B_{\text{com}}^{\text{Tx}}$. This variation occurs due to the large bandwidth occupied within the investigated frequency range of $(77 - 81)\,\text{GHz}$ commonly used in
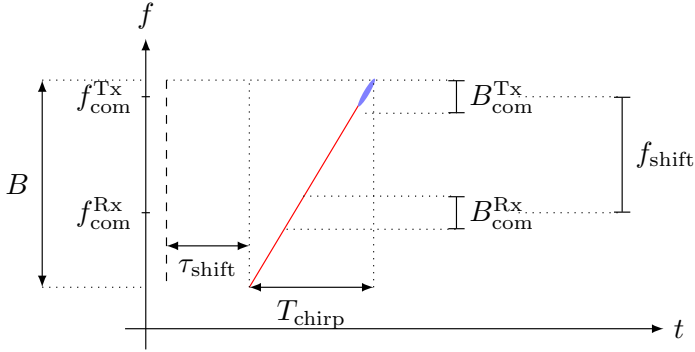
Fig. 4.2: Exemplary frequency difference f_{shift} between the carrier frequencies at the transmitter and receiver side with arbitrary time shifting τ_{shift} for partial chirp modulation [A$^+$22b].

radar applications. Additionally, the exact beginning of the modulation section may be unknown, resulting in a shift in the time domain denoted as τ_{shift}, which can also impact the demodulation process. It is important to note that the same consideration applies to TFSK modulation, as discussed in Chapter 3.

Sequence Structure

The structure showing the transmit signal for the proposed CaCS radar system with a duration T_{seq} is depicted in Fig. 4.3. As determined by this structure, every CaCS node that aims to communicate with other nodes, i.e., radar sensors, in the environment should predetermine at least one synchronization CS-based frame. This structure is adopted for CaCS nodes that rely on the chirp scheme for the radar measurements presented in Chapter 2, and it might be employed with modification based on other assigned waveforms to deal with coarse and fine shifts occurring at the receiver side during the transmission. A set of multiple up- and down-chirps $Q_s \in \mathbb{N}_+$ chirps (e.g., contains 8 predetermined intervals) with index $q_s \in \{0, 1, \ldots, Q_s - 1\}$ and a duration $T_{\text{seq}}^{\text{sync}}$ is assigned for dealing with synchronization. The sector responsible for the synchronization within the CS-based frame is predetermined at the beginning of the transmission and plays
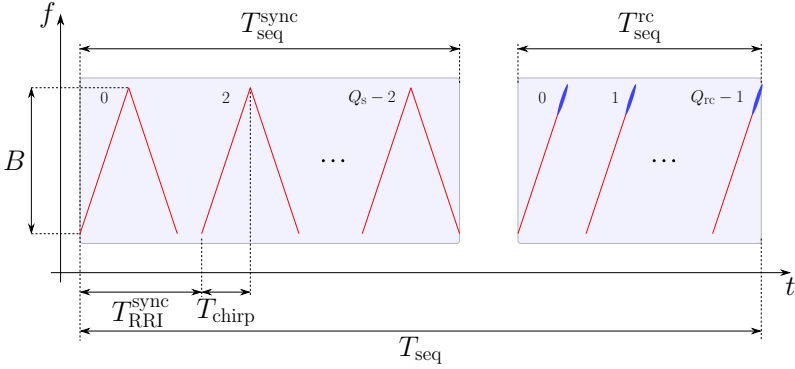
Fig. 4.3: Structure of the transmit CaCS signal, including the pattern of the coarse and fine synchronization chirps within the time duration $T_{\text{seq}}^{\text{sync}}$, the dedicated chirps for both radar and communication within the time duration $T_{\text{seq}}^{\text{rc}}$. T_{seq} is the whole sequence duration, $T_{\text{RRI}}^{\text{sync}}$ is the duration of one synchronization interval, and T_{chirp} is the duration of one chirp [A+22b].

a significant role as a preamble to orientate the receiver in the time-frequency plane optimally. Although the mentioned pattern is equivalent to the classical FMCW dual-ramps waveform, the investigated signal lasts a shorter period (e.g., $T_{\text{chirp}} = 10\,\mu s$ for automotive radars with $B = 1\,\text{GHz}$ at the (77-81) GHz band). In the time domain, the continuous time signal $x_{q_s}(t)$ transmitted for enabling both radar and communication properties can be characterized as

$$
x_{q_s}(t) = \begin{cases}
A \cos\left(\pi\mu\left(t - q_s T_{\text{RRI}}^{\text{sync}}\right)^2 + 2\pi\left(f_c - \frac{B}{2}\right)t + \varphi_0\right), \\
\quad t \in [q_s T_{\text{RRI}}^{\text{sync}}, q_s T_{\text{RRI}}^{\text{sync}} + T_{\text{chirp}}) \\[2mm]
A \cos\left(-\pi\mu\left(t - q_s T_{\text{RRI}}^{\text{sync}}\right)^2 + 2\pi\left(f_c - \frac{B}{2}\right)t + \varphi_0\right), \\
\quad t \in [q_s T_{\text{RRI}}^{\text{sync}} + T_{\text{chirp}}, q_s T_{\text{RRI}}^{\text{sync}} + 2T_{\text{chirp}}) \\[2mm]
0, \\
\quad t \in [q_s T_{\text{block}}^{\text{sync}} + 2T_{\text{chirp}}, (q_s + 1)T_{\text{block}}^{\text{sync}})
\end{cases}
\tag{4.1}
$$

where A denotes the amplitude of the transmit signal, μ is the chirp rate, f_c is the center frequency. B presents the signal bandwidth and φ_0 is the initial phase of the investigated signal. Based on the presented concept, the whole synchronization sequence can be chosen to correct coarse time and frequency offsets, and the last two intervals, for example, adopting the same configuration, are enforced to further compensate for any fine shifts in the time-frequency plane. Furthermore, Fig. 4.3 depicts an exemplary structure of the chirps employed for radar and communication measurements. The depicted chirps in Fig. 4.3 adopt the partial modulation of communication symbols within the upper section of each transmit chirp (marked in blue) within a sequence of $Q_{rc} \in \mathbb{N}_+$ modulated chirps during the time duration T_{seq}^{sync}, as presented in Chapter 3. It should be mentioned that although the radar-communication signal follows the integration method described in [ANWZ19] and depicted in Fig. 4.3, the TFSK approach can be adapted, where the communication symbols are equivalent to predefined time-frequency shifts and can replace the PM technique in the whole sequence structure adopted in this chapter.

4.4 Receiving Procedure

This section describes the chosen receiving procedure to extract the communication data at the receiver side of a CaCS-based radar system. The receiving scheme mainly consists of a synchronization section and a demodulation process, as depicted in Fig. 4.4, where all the blocks are individually represented in the upcoming subsections. The synchronization ensures the time-frequency alignment of the signal at the communication receiver side by performing both coarse and fine corrections. The alignment is a way to estimate the signal pattern transmitted from CaCS nodes dependent on STFT and linear regression on the received signal. Next, demodulation is performed on the received modulated chirps to retrieve communication data associated with a preselected digital modulation constellation. Assuming the structure of the modulated signal presented in Chapter 3, the receiving procedure shown in Fig. 4.4 contains multiple sections within one sequence dedicated on the one hand to facilitate the synchronization between two examined CaCS nodes and, on the other hand, to radar and communication measurements.
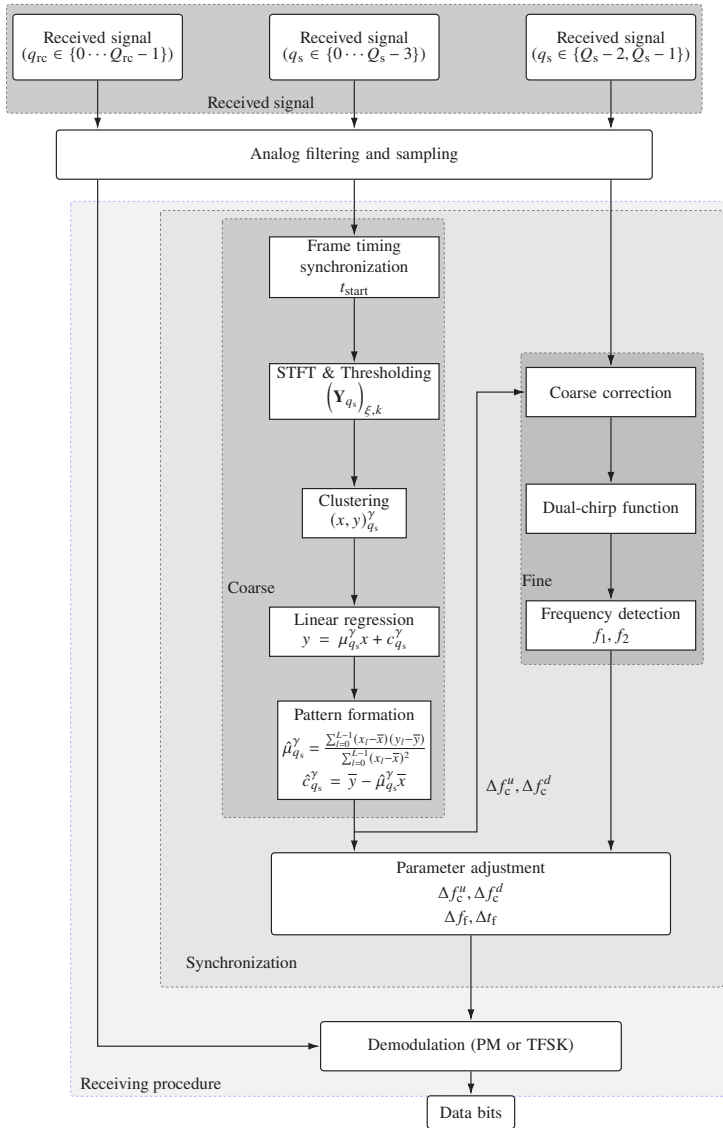
Fig. 4.4: Receiving procedure of the communication receiver, including the steps of the proposed synchronization method and the demodulation. The first chirps are responsible for the synchronization, while the latter convey radar-communication data [A$^+$22b].

The first section of the signal transmitted from one CaCS node is employed for synchronization according to the sequence structure presented in the last section, where the indicated signal pattern is adapted from the conventional FMCW radar, as shown in Fig. 4.3. Besides, the next chirps convey the radar-communication data according to the modulation schemes presented in Chapter 3. Apart from the chirps assigned for shared radar and communication purposes, Fig. 4.5 illustrates exemplary depictions of the synchronization signal explored in the proposed receiving procedure adopting the following parameters. $T_{\text{chirp}} = 10\,\mu s$, $f_c = 79\,\text{GHz}$, and $B = 1\,\text{GHz}$. The normalized amplitude of the chosen signal in the time domain is shown in Fig. 4.5(a). In this figure, two transitions in the phase at 5 µs and 15 µs can explicitly be observed according to the proposed sequence structure in the previous section, where each distinctive transition corresponds to one up- or down-chirp. Furthermore, Fig. 4.5(b) illustrates the allocation of one interval of the synchronization signal in the time-frequency plane using STFT, where the magnitude of the signal is also normalized. In the following subsection, the signal depicted in Fig. 4.5 is further employed for analyzing coarse synchronization properties in the time-frequency plane.

4.4.1 Coarse Synchronization

As indicated in the previous section, the proposed communication receiver can be employed separately at the receiver side of one CaCS node to avoid restrictions on the radar functionalities. Besides, it has a limited frequency bandwidth, which keeps the adjustment equivalent to the hardware adopted in current CS-based radar sensors. In addition, the bounded frequency bandwidth limits the hardware costs compared with digital radar systems, which require fast ADCs. However, since the current radar sensors can adopt various unknown parameters, such as the assigned center frequency and the occupied time duration, within the same frequency bandwidth, the demodulation process might fail without a guaranteed synchronization between the transmitter from one CaCS node and receiver from another node. In this section, the coarse synchronization is intended to amend the time and frequency offsets that occurred at the communication receiver of one CaCS node. The signal adopted for the coarse synchronization is equivalent to the one shown in Fig. 4.5. The structure and
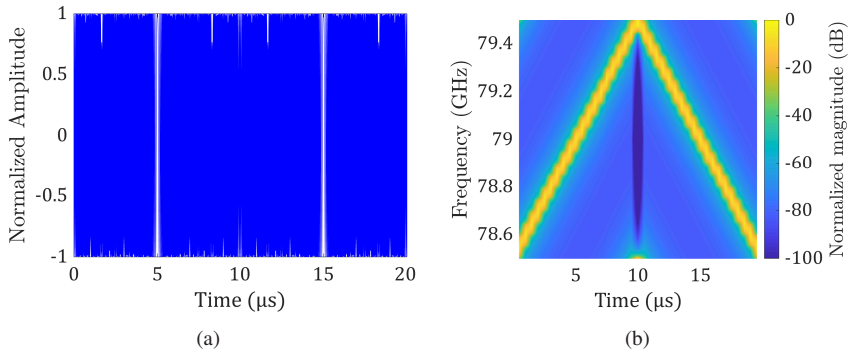
Fig. 4.5: The synchronization signal adopting the following parameters. $T_{\text{chirp}} = 10\,\mu\text{s}$, $f_{\text{c}} = 79\,\text{GHz}$, and $B = 1\,\text{GHz}$. (a) The representation of the signal in the time domain. (b) Spectrogram of the signal using STFT in the time-frequency plane.

functions of the coarse synchronization are depicted in Fig. 4.4 and explained as follows.

Sequence Timing Synchronization

At the receiver of the CaCS-based radar system, the received synchronization signal $y_{q_s}(t) \in \mathbb{R}$ acts as preamble, which precedes the radar-communication data transmitted by $y_{q_{\text{rc}}}(t) \in \mathbb{R}$, and contains the output version of the signal $x_{q_s}(t) \in \mathbb{R}$ influenced by the channel. In this framework, the considered synchronization signal $y_{q_s}(t)$ assigned firstly for coarse synchronization is filtered according to the bandwidth B_{com} dedicated for communication in Chapter 3 and sampled by ADCs for further processing. The start of the preamble appointed for synchronization is determined by a sliding window derived from Schmidl and Cox algorithm (SCA) [SC97], which has been used in digital communication multiplexing systems, such as OFDM and OCDM. The procedure of detecting the beginning of the preamble includes two successive steps. First, the sliding window is divided into two identical sections (each has 4 chirps), as depicted in Fig. 4.6. Second, Both assigned parts are correlated to generate a peak detection pattern, which determines the start of the preamble, as shown later in Fig. 4.7. If $2U$ presents the length of the preamble in samples of the
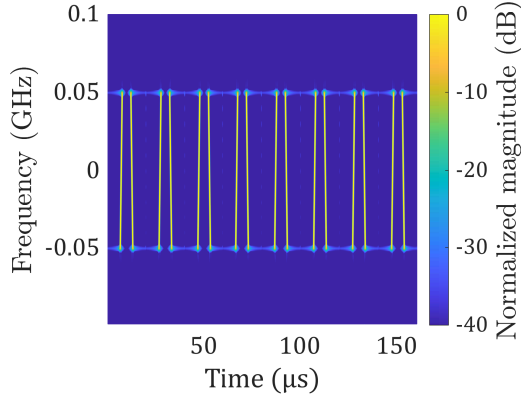
Fig. 4.6: Visualization of the sliding window employed for coarse corrections in the time-frequency plane.

signal $y_{q_s}(t)$ after filtering and sampling it in the digital domain, the correlation between the two assigned sections is given by

$$AC_n = \sum_{u=0}^{U-1} y_{n+u}^{q_s *} y_{n+u+U}^{q_s},$$ (4.2)

where n is the sample index related to the sliding window, and u is the window index. In this context, the metric of the correlation process scaled by the received energy of the second half-preamble MC is performed as

$$ME_n = \frac{|AC_n|^2}{(MC_n)^2},$$ (4.3)

where the energy of the preamble is calculated as

$$MC_n = \sum_{u=0}^{U-1} |y_{n+u+U}^{q_s}|^2.$$ (4.4)

Fig. 4.7 illustrates an exemplary output of the correlator caused by the shift during the transmission for different values of delay τ_{shift} based on the length of the preamble $2U$. The maximum peak value of the correlator indicates the start
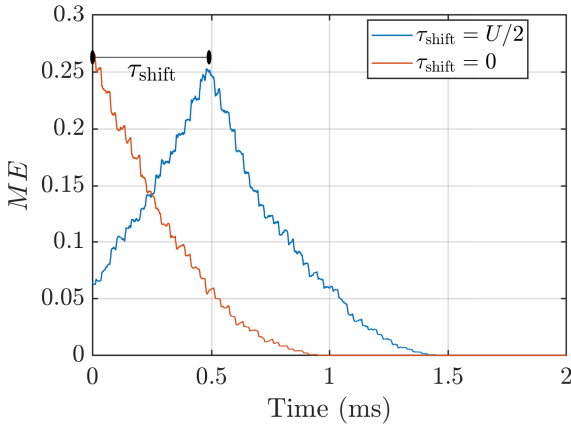
Fig. 4.7: Exemplary output of the correlator caused by the shift during the transmission for different values of delay τ_{shift} based on the length of the preamble $2U$, including the influence of noise and channel [A+22b].

position of the preamble t_{start}, and the pattern formulated by the correlation has its shape according to the specifications of chirp signals, where the influence of noise and the channel have been included.

STFT and Thresholding

After indicating the start point of the preamble t_{start} in the previous paragraph, the filtered signal is analyzed by STFTs in the time-frequency plane as an adaptation of audio and image signal processing. STFT is an adjustment of the DFT, and in radar application, it has been applied in several studies to evaluate the micro movement of objects observed in the surroundings [DPBS17]. In terms of the proposed synchronization method, STFT is used as one of the specialized tools for time-frequency distributions (such as Gabor and Wigner-Ville distributions) applied to the investigated signals to extract its allocation in the time-frequency plane [Mü15]. The signal is divided into multiple segments of an adequate size $\Xi \in \mathbb{N}$ and multiplied with a chosen windowing function w_u of
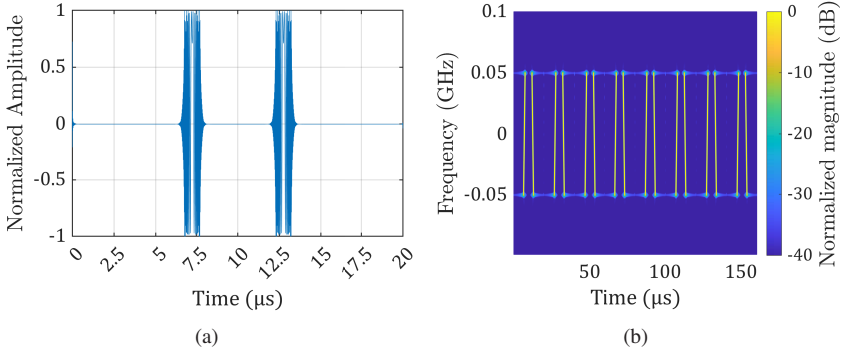
Fig. 4.8: The filtered synchronization interval in the baseband. (a) The synchronization interval in the time domain. (b) The synchronization sequence in the time-frequency plane using STFT.

length $U \in \mathbb{N}$ [KG14], [Mü15], (for instance, Hamming). The discrete equation representing the filtered signal after applying the STFT can be expressed as

$$\left(\mathbf{Y}_{q_s}\right)_{\xi,k} = \sum_{u=0}^{U-1} \left(y_{q_s}\right)_{u+\xi P_{hop}} w_u \exp\left(\frac{-2\mathrm{j}\pi k u}{U}\right) \tag{4.5}$$

with $\xi \in \mathbb{Z}$ being the segment index and for each segment $\in \mathbb{C}^K, u \in [0, U-1]$ the sample index, and $P_{hop} \in \mathbb{N}$ the STFT hop size. $k \in [0, K]$ is the frequency index, and $q_s \in \{0, 1, \ldots, Q_s - 1\}$ is the chirp index that indicates the coarse synchronization chirps, where $Q_s < Q$ relative to the frame structure presented in the last section. Fig. 4.8 shows an exemplary synchronization block after filtering it and applying the STFT in the baseband. Since only a part of the signal is sampled, the signal is visualized within the MHz scope in Fig. 4.8. The normalized amplitude of the signal in the time domain is shown in Fig. 4.8(a). In this figure, one interval assigned for synchronizing the transmit sequence can be explicitly observed. Additionally, Fig. 4.8(b) illustrates the allocation of the exemplary interval of the filtered synchronization signal in the time-frequency plane using STFT, where the magnitude of the signal is also normalized. Next,

a thresholding function $\gamma(a)$ is applied on Y_{q_c} to separate chirps from the noise and can be described as

$$\gamma(a) = \begin{cases} 0 & \text{if } |a| \leq H \\ a & \text{if } |a| > H \end{cases} \tag{4.6}$$

where $H \in \mathbb{R}$ is empirically set based on the value of the $\mathrm{SNR_{sync}}$ of the received signal (synchronization signal), i.e., all elements of the time-dependent power spectral density (PSD) of the signal less than H are set to zero. Setting H influences the density of the points after applying the STFTs so that the complexity of the calculation decreases when the number of the analyzed points drops. If a low value of H is adopted, the number of allocated points increases, leading to more complexity in assigning the clusters and a deviation in the linear regression because of the escalating density of the examined points. The signal $\mathbf{Y}_{q_c}$ after applying the thresholding is given as

$$\left(\mathbf{Y}_{q_s}^{\gamma}\right)_{\xi,k} = \gamma\left(\left(\mathbf{Y}_{q_s}\right)_{\xi,k}\right) \tag{4.7}$$

After applying the thresholding on the investigated signal, the signal can be represented in sets of points $\{(x,y)_{q_s}^{\gamma}\}$ for each up- or down chirp that can be classified and categorized to achieve the desired goal of reforming the pattern of the transmit signal, as shown in the latter subsections.

Clustering

Clustering aims to group several points into one or several sets to simplify further analyses applied to the explored datasets. For this reason, clustering has been used in many fields. Besides radar applications, clustering has been mainly employed for many purposes, such as clustering the targets [LLK18] after the performed conventional detection algorithms, as shown in Chapter 2. In the framework of the proposed synchronization method, a clustering method can be chosen and implemented to denoise the examined signal carried out for the synchronization and efficiently estimate the desired pattern in the next step. One algorithm adopted in this work is density-based spatial clustering of applications with noise (DBSCAN) [EKSX96]. DBSCAN relies on the advantage that no *a priori* input about the number of clusters is required. In other words,
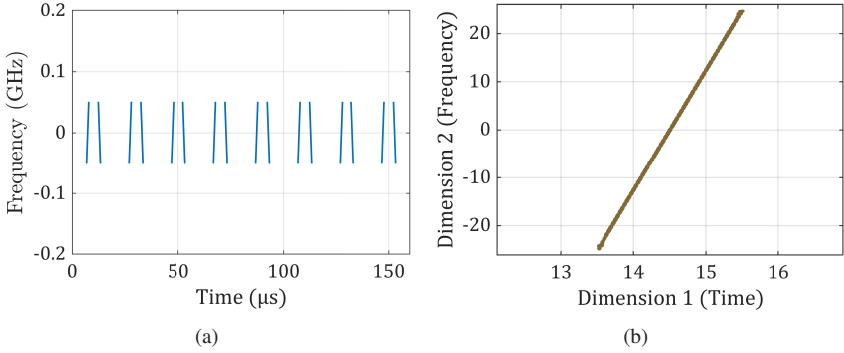
Fig. 4.9: Visualization of the synchronization sequence after thresholding and clustering. (a) The time-frequency plane of the signal after applying thresholding. (b) The time-frequency plane of the signal after clustering the investigated points into a 2D grid within one cluster for simplicity, and the case with multiple clusters is illustrated in Chapter 5.

the DBSCAN algorithm divides the investigated points in some space into clusters based on a predefined radius and the minimum points within a cluster. Consequently, the algorithm identifies the following categories of points. First, points in a cluster $C_{\text{cluster}} \in \mathbb{N}_+$ are classified as core points if they hold at least the minimum number of neighbors $N_{\text{min}} \in \mathbb{N}_+$ in their epsilon neighborhood $\epsilon \in \mathbb{R}_+$. Second, border points whose number of neighbors $< N_{\text{min}}$. Third, noise points are outliers that are classified into no clusters. The algorithm input includes the following data. The output matrix of the thresholding operation after the STFTs, the minimum number of neighbors N_{min} required for a core point, and the radius for a neighborhood search ϵ around the point. A point o is directly density-reachable from another point b with respect to ϵ, N_{min}, and a sub-dataset $D_{q_s}^{\gamma} = \{(x, y)_{q_s}^{\gamma}\} \in D = \{D_0^{\gamma}, D_1^{\gamma}, \cdots, D_{Q_{s-1}}^{\gamma}\}$ if

- $Eps(o) = \{b \in D_{q_s}^{\gamma} | dist(o, b) \le \epsilon\}$, and
- $|Eps(o)| \ge N_{\text{min}}$.

where $dist$ is the measured distance between the points, and $D_{q_s}^{\gamma}$ represents the points in the time-frequency plane of the investigated signal $\mathbf{Y}_{q_s}^{\gamma}$. As soon as the clusters are defined and set together to create the linear structure of the received chirps, the next step is responsible for anticipating the signal pattern

based on the output of this step $\left(D_{q_s}^{\gamma}\right)^{C}$. Fig. 4.9(a) depicts the examined signal in the time domain after applying the STFT and thresholding, while Fig. 4.9(b) shows an exemplary cluster consequently, where the points of each filtered chirp are classified collectively into one group. A brief mathematical explanation of DBSCAN is summarized in Algorithm 1. As soon as the clusters are determined, the following subsection discusses the detection of the slope of each chirp.

Algorithm 1 : DBSCAN algorithm.

---

1 **Input**: $D_{q_s}^{\gamma} = \{(x, y)_{q_s}^{\gamma}\}$, $N_{\min}$, ϵ, $C_{\text{cluster}} \leftarrow 0$
2 **for** *each point $o \in D_{q_s}^{\gamma}$* **do**
3   **if** *p is unclassified* **then**
4   the lable of clusters $C_{\text{cluster}} = C_{\text{cluster}} + 1$
5   **for** *each point $u \in D_{q_s}^{\gamma}$* **do**
6   **if** $Eps(o, b) = dist(o, b) \leq \epsilon$ **then**
7   o is directly density-reachable from b
8   b is a neighbor point
9   **if** $Eps(o) \geq N_{\min}$ **then**
10   o is a core point
11   **else**
12   o is a noise point
13   **else**
14   select another point
15   **else**
16   select another point
17 **Output**: $\left(D_{q_s}^{\gamma}\right)^{C}$ according to C_{cluster}

Linear Regression

The key idea of reconstructing the transmit chirps applied for synchronization is to estimate the slope of every up- and down-chirp within the mentioned synchronization sequence to derive the complete pattern. Given the output of the clustering step, the slope of the chirps within the empirical dataset

$D_{q_s}^\gamma \equiv \{(x, y)_{q_s}^\gamma\}$ is computed. The calculation depends on linear regression (least-squares approximation), described as a line-fitting problem in [Bag05] and in conformity with the following equation

$$y = \mu_{q_s}^\gamma x + c_{q_s}^\gamma \tag{4.8}$$

where $\mu_{q_s}^\gamma$ is the slope of the line, and $c_{q_s}^\gamma$ is the y-intercept value. Given a set of points $D_{q_s}^\gamma = \{(x, y)_{q_s}^\gamma\}$ in the time-frequency plane, there is a line $\hat{y} = \hat{\mu}_{q_s}^\gamma x + \hat{c}_{q_s}^\gamma$ that best qualifies the data in terms of minimizing the root mean square (RMS) error, where $\hat{\mu}_{q_s}^\gamma \in \mathbb{R}$ can be calculated as

$$\hat{\mu}_{q_s}^\gamma = \frac{\sum_{l=0}^{L-1}(x_l - \overline{x})(y_l - \overline{y})}{\sum_{l=0}^{L-1}(x_l - \overline{x})^2} \tag{4.9}$$

with $\overline{y}$ and $\overline{x}$ denoting the mean of the chosen time-frequency plane points. $l \in \{0, 1, \ldots, L-1\} \in \mathbb{N}$ is the index of the points within the investigated dataset $D_{q_s}^\gamma$, which represents the time-frequency plane in this study. In addition, $\hat{c}_{q_s}^\gamma \in \mathbb{R}$ can be derived from

$$\hat{c}_{q_s}^\gamma = \overline{y} - \hat{\mu}_{q_s}^\gamma \overline{x} \tag{4.10}$$

The output of the linear regression is a set of linear lines corresponding to the investigated datasets $\{D_0^\gamma, D_1^\gamma, \cdots, D_{Q_s-1}^\gamma\}$. Since the transmit chirps are linear and well predetermined, every consequent set of up-down chirps and down-up will intersect at a certain point in the time-frequency plane, as depicted in Fig. 4.10. The procedure above is reiterated between the analyzed up-down chirps to deduce all intersections. From this perspective, every intersection (top - or down - seeded) between every two successive chirps shown in Fig. 4.10(a) and can be given by solving the two linear equations

$$y = \hat{\mu}_{q_s}^\gamma x + \hat{c}_{q_s}^\gamma, \tag{4.11}$$
$$y = \hat{\mu}_{q_s+1}^\gamma x + \hat{c}_{q_s+1}^\gamma \tag{4.12}$$

The solution includes one set of coordinates within the intersections chain $\{(\hat{X}, \hat{Y})_0^\gamma, (\hat{X}, \hat{Y})_1^\gamma, \ldots, (\hat{X}, \hat{Y})_{Q_s-1}^\gamma\}$. $(\hat{X}, \hat{Y})_{q_s}^\gamma \in \mathbb{R}^2$ represents the intersection coordinates in the time-frequency plane, and q_s being the chirp index. The up-
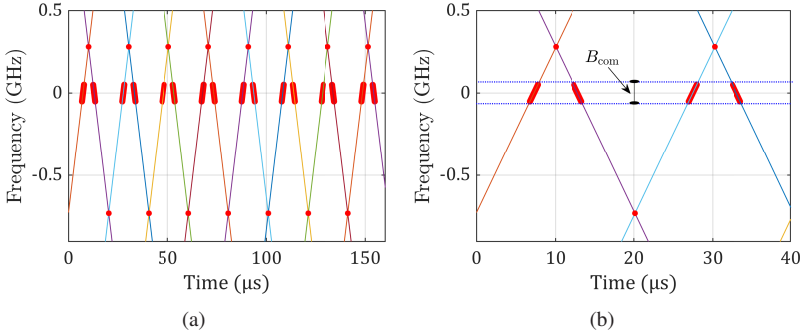
Fig. 4.10: Formation of the pattern using the synchronization signal based on linear regression. (a) The pattern extraction in the time-frequency plane of the whole synchronization sequence based on linear regression. (b) Two synchronization intervals with intersected points in the time-frequency plane within B_{com} [A$^+$22b].

seeded frequency offset $\Delta f_{\mathrm{c}}^{\mathrm{u}} \in \mathbb{R}$ is derived from the mean value of the upper intersections black-marked along the Y-Axis as shown in Fig. 4.10(b)

$$\Delta f_{\mathrm{c}}^{\mathrm{u}} = \frac{2}{Q_{\mathrm{s}}} \sum_{q_{\mathrm{s}}=0}^{Q_{\mathrm{s}}/2-1} \hat{Y}_{2q_{\mathrm{s}}}^{\gamma} \tag{4.13}$$

while the down-seeded frequency offset $\Delta f_{\mathrm{c}}^{\mathrm{d}} \in \mathbb{R}$ can be derived from the mean value of the lower intersections along the Y-Axis as shown in Fig. 4.10(b)

$$\Delta f_{\mathrm{c}}^{\mathrm{d}} = \frac{2}{Q_{\mathrm{s}} - 2} \sum_{q_{\mathrm{s}}=0}^{Q_{\mathrm{s}}/2-2} \hat{Y}_{2q_{\mathrm{s}}+1}^{\gamma} \tag{4.14}$$

As a result, the sequence pattern is reconstructed in the time-frequency plane, as depicted in Fig. 4.10(b), and the carrier frequency $f_{\mathrm{com}}^{\mathrm{Rx}}$ at the receiver side of the investigated CaCS node is retuned dependent on the distance between the intersections and the communication part. The mentioned distance above should be known so that the former process does not lead to further undesired misalignments. The complexity of the proposed synchronization method depends mainly on the STFT and linear regression after indicating the beginning of the sequence. The start point detection is equivalent to the complexity of applying a matched filter w.r.t the correlation and is adopted further in Chapter 5. For

---

Algorithm 2 : Coarse synchronization algorithm.

---

1 Detection of the start point $\rightarrow$ (4.2) and (4.3) $\rightarrow t_{\text{start}}$

2 **Image-like processing**

3   **Input:** $\mathbf{Y}_{q_{\text{s}}}$

4   **for** *each up-down chirp within the coarse synchronization sub-sequence* **do**

5   compute STFT to obtain $\left(\mathbf{Y}_{q_{\text{s}}}\right)_{\xi,k}$

6   set a threshold H for the samples $\rightarrow \left(\mathbf{Y}_{q_{\text{s}}}^{\gamma}\right)_{\xi,k} = \gamma\left(\left(\mathbf{Y}_{q_{\text{s}}}\right)_{\xi,k}\right)$

7   extract the data and set them together after clustering (Algorithm 1 $\rightarrow \{(x,y)_{q_{\text{s}}}^{\gamma}\}$)

8   compute both $\hat{\mu}_{q_{\text{s}}}^{\gamma}$ and $\hat{c}_{q_{\text{s}}}^{\gamma} \rightarrow$ (4.9) and (4.10)

9   calculate the up- and down-seeded intersections between every two successive chirps $\rightarrow$ (4.11), and (4.12)

10   extract $(\hat{X},\hat{Y})_{q_{\text{s}}}^{\gamma}$ of every up- and down-seeded intersection

11   calculate $\Delta f_{\text{c}}^{\text{u}}$ and $\Delta f_{\text{c}}^{\text{d}} \rightarrow$ (4.13) and (4.14)

12 **Output**: $\Delta f_{\text{c}}^{\text{u}}$ and $\Delta f_{\text{c}}^{\text{d}}$

---

each STFT process, the computational complexity is given by $\Xi \times O(U \log U)$, where U is the length of the assigned window, and Ξ represents the number of FFT operations (number of segments) employed to calculate STFT. In addition, for clustering, $O(L \log L)$ operations are needed in the best case, where L represents the number of scanned points. On the other hand, for each linear regression operation after thresholding, $O(\Upsilon_{\text{norm}}^3)$ is required, where Υ_{norm} is the number of features in the normal equation of the linear regression. A short explanation of the coarse synchronization is summarized in Algorithm 2.

4.4.2   Fine Synchronization

Since the bandwidth used in automotive applications can occupy 1 GHz or even above in the frequency range $(77 - 81)$ GHz, the time and frequency shifts might be considerable and cause some failures during the demodulation of communication data transmitted between the communicating CaCS nodes. Although the coarse synchronization in the preceding subsection can reallocate the receiver
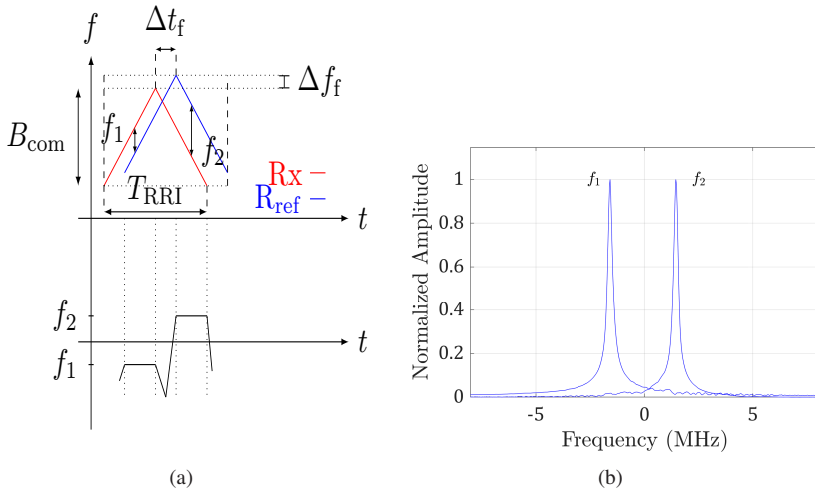
Fig. 4.11: Visualization of the pattern formation using the synchronization signal based on linear regression. (a) Exemplary residual misalignments between the transmitter and receiver, which are corrected by fine synchronization. (b) Frequency shifts related to the fine-stage based on range-Doppler estimation [A+22b].

carrier, estimate, and correct the occurred offsets in the time-frequency plane, the method is bounded by the minimum RMS error caused during the estimation of the slopes. These additional offsets are usually small but might influence the demodulation process; therefore, they should be compensated. Fig. 4.11(a) illustrates an exemplary signal created at the communication receiver (R_{ref}, blue-marked) for fine synchronization that should match the received counterpart (Rx, red-marked) if the investigated signals are fully synchronized. As described previously in this section, this approach mainly relies on employing a set of an up- and a down-chirp to estimate two residual frequencies equivalent to the range-Doppler estimation in FMCW radar [VPSE02]. The aforementioned frequency offset between the investigated nodes related to the fine stage $\Delta f_f \in \mathbb{Z}$ can be defined as

$$\Delta f_f = \frac{f_1 - f_2}{2},$$ (4.15)

Algorithm 3 : Fine synchronization algorithm.

---

1 Adopt the correction results from the coarse synchronization

2 Filter the chirps according to the investigated bandwidth, and convert
the signal to the digital domain

3 **for** *set of an up- and a down chirp within the joint radar-communication
sequence* **do**

4 Downconvert the chirps according to FMCW concept
(downconversion with a reference set of up- and down-chirps)

5 compute DFT to attain both f_1, $f_2 \rightarrow$ (4.15) and (4.16)

6 **Output**: Δf_{f}, and Δt_{f}

---

and the corresponding time offset $\Delta t_{\mathrm{f}} \in \mathbb{R}$ can be derived from

$$\Delta t_{\mathrm{f}} = \frac{f_2 + f_1}{2\mu}, \tag{4.16}$$

where μ is the chirp rate and f_1, f_2 are the respective residual frequencies
associated with the up- and down-chirps after the downconversion and applying
of the DFT in the baseband successively, as depicted in Fig. 4.11(b). It is
worth highlighting that the mentioned fine synchronization concept is complex
to execute without any previous coarse synchronizations due to the broadly
utilized bandwidth in automotive applications (1 GHz or more). Moreover, the
receiver of the investigated CaCS node must consecutively generate an up- and a
down-chirp, which might be digitally performed after the CW downconversion
concerning the communication carrier frequency. A brief description of the fine
synchronization is introduced in Algorithm 3.

4.4.3 Demodulation

After correcting the receiver alignment of the investigated CaCS node in the
time-frequency plane (i.e., the prediction of the transmit signal pattern), the
demodulation can be applied to extract the transmit communication data, as
mentioned in Fig. 4.4. A detailed description of the demodulation has been car-
ried out in Chapter 3, where the study investigated the partial chirp modulation
with various digital modulation schemes (e.g., QPSK) and TFSK modulation as

possible candidates for integrating communication data into CS-based radars. It is worth highlighting that a part of each transmit chirp has been used as another preamble to detect the beginning of the communication section in the described PM technique.

4.4.4   Analyzing of Errors in the Time-Frequency Plane

In light of the proposed synchronization method in this chapter, both time and frequency errors that occurred in the time-frequency plane are analyzed. Since several studies have introduced similar approaches to the fine synchronization algorithm presented in the previous section, this section is concentrated on the error that occurred w.r.t the coarse synchronization algorithm proportional to different SNR_{sync} values. This investigation is carried out with simulations and measurements in the automotive frequency band 79 GHz to verify the validity of the proposed method. According to the receiving procedure presented in Fig. 4.4, the synchronization preamble is sent at the beginning of the transmit sequence, while the next chirps are implemented for radar and communication purposes based on the modulation schemes presented in Chapter 3. On account of this, the simulations are inspected by Matlab, and the measurement concept is investigated at one of the laboratories at IHE, as explained in Chapter 2. Given the block diagram of the measurement setup, the high-frequency hardware components employed during this work cover the range $(71 - 86)$ GHz and can be introduced as follows. Two subharmonic mixers are set to up and downconvert the signal from the baseband to the passband and conversely. Next, a frequency multiplier and a signal generator are set to upconvert the signal to the domain of $(29 - 43)$ GHz. Furthermore, an RFSoC (FPGA, DACs, and ADCs) has been responsible for the signal characterization in the baseband as representative of the transmitter and receiver of CaCS nodes. First, the examined signal has been manually shifted in time relative to τ_{shift} to ensure the presence of time and frequency shifts. Second, the chosen carrier frequency on the receiver is manually assigned to deviate $(B/4)$ in the baseband from its counterpart at the transmitter side of one CaCs node to ensure signal misalignment. Using the parameters performed in Table 4.1 (extended from Table 2.1), and the measurement setup presented in Section 2.7, the coarse frequency difference shown in Fig. 4.12 ($f_{shift} = f_{com}^{Tx} - f_{com}^{Rx} \pm f_{offset}$) is estimated with the synchronization sequence represented as a preamble at the beginning of the transmission
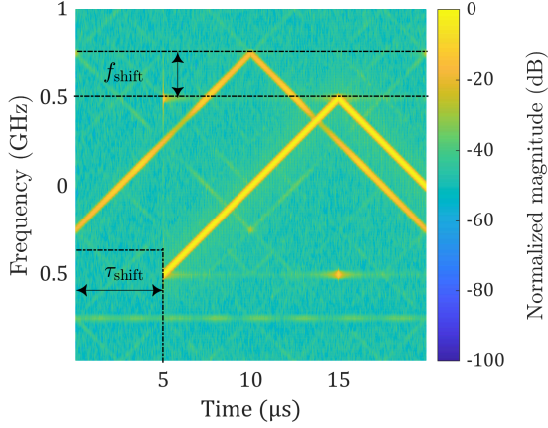
Fig. 4.12: Spectrogram of exemplary transmit and received signals through the measurement before applying the proposed synchronization algorithm. $f_{\text{shift}} = f_{\text{com}}^{\text{Tx}} - f_{\text{com}}^{\text{Rx}} \pm f_{\text{offset}}$ and τ_{shift} represents the frequency and time offsets in the baseband [A+22b].

of the whole sequence, where $f_{\text{offset}} \in \mathbb{R}$ is a random offset value connected with the employed RFSoC in the measurement. The start point of the preamble is detected ($\tau_{\text{shift}} \cdot f_s \simeq 500$ Samples) according to the approach suggested in Section 4.4. Fig. 4.13 depicts the elaborated measurement flow of the coarse

Table 4.1: CS parameters applied to measurement setup for synchronization

Symbol	Parameter	Value
B	Chirp bandwidth	1 GHz
f_c	Radar carrier frequency	79 GHz
T_{chirp}	Chirp duration	10 μs
T_p	Pause duration	0.1 μs
$T_{\text{RRI}}^{\text{sync}}$	Ramp Repetion Time	10.1 μs
$f_{\text{com}}^{\text{Rx}}$	Communications receiving frequency	78.75 GHz
Q_s	Chirps per sequence	8
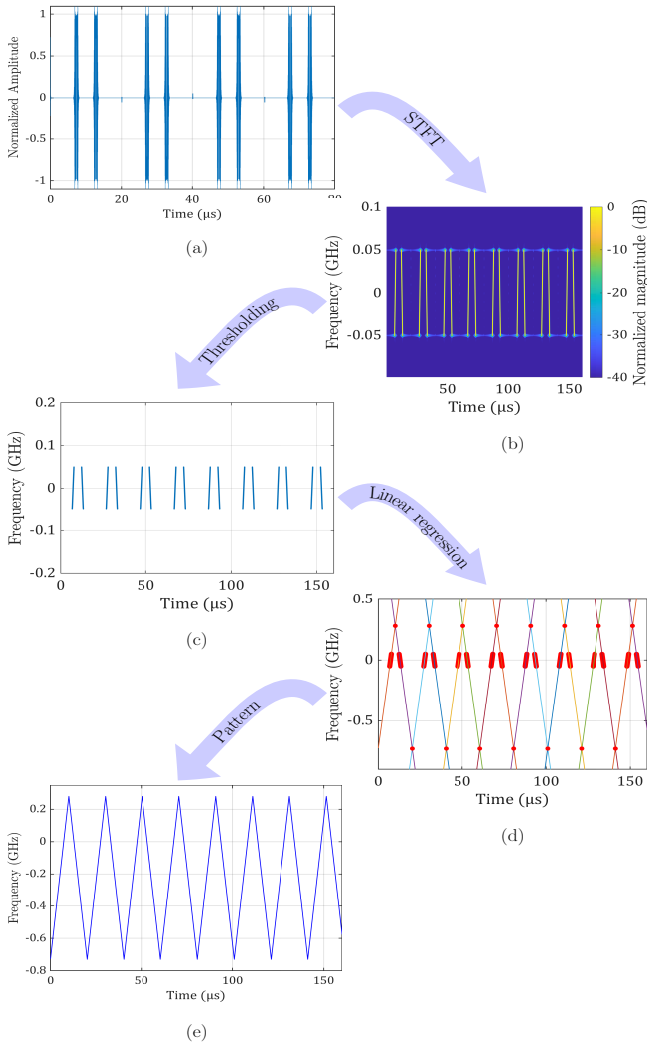
Fig. 4.13: Summary of the synchronization signal under the proposed method where the filtered signal at the receiver side concludes solely a part of the complete bandwidth. (a) The illustration of the investigated signal in the time domain. (b) Spectrogram of the signal using STFT. (c) The time-frequency plane of the signal after thresholding and clustering. (d) Intersections finder based on linear regression. (e) The synchronization sequence after applying pattern formation under the intersections finder.

synchronization method relevant to Algorithm 2. Fig. 4.13 shows the coarse synchronization chirps in the time domain after the downconversion to the baseband domain and filtering of the signal, which seems equivalent to short data bursts in limited time durations compared to the original received signal before filtering. Besides, Fig. 4.13 and Fig. 4.13 illustrate the filtered signal in the time-frequency plane after applying both thresholding and clustering, where the clusters that compose one chirp are summarized in one cluster for simplicity. Next, the slope of every up- and down-chirp is estimated relying on the linear regression analysis presented in (4.9) and (4.10), where least square estimations are carried out limited to the boundaries of Cramér Rao Bound (CRB) presented later in this section, and dependent on the obtained points from each slope. Since the investigated slopes are linear with a specific slant, the successive line intersects in the time-frequency planes in particular locations on the grid. The output of the intersections finder from (4.13) and (4.14) is shown in Fig. 4.13. In this context, intersections created by the up- and down-seeded points are plotted as black-marked points between the diagonal lines.

After analyzing the output of all mentioned steps, the sequence pattern is designed and reconstructed as depicted in Fig. 4.13 and $\Delta f_c^u \simeq 250\,\text{MHz}$, $\Delta f_c^d \simeq -750\,\text{MHz}$ are determined. After that, the time-frequency alignment of the receiver is updated, and the fine synchronization scheme is carried out with the last two intervals dependent on Algorithm 3. As a result, the two residual frequency shifts are estimated according to the range-Doppler concept. The corresponding fine frequency offset is calculated as $\Delta f_f = (f_2 - f_1)/2$, and the fine time offset is $\Delta t_f \cdot f_s = (f_2 + f_1)f_s/(2\mu)$, as shown in Fig, 4.11(b) in the last section. It is worth highlighting that almost any chirp modulation can be adopted, reliant on the mentioned method. Nevertheless, the recommended synchronization approach has been chosen to verify PM and the TFSK schemes presented in Chapter 3.

Line Fiting

The reconstruction of the desired pattern in linear regression depends on the number of obtained points after filtering the examined signal and applying thresholding to it to decrease complexity efforts. The influence of the number

of points on the analyses in the time-frequency plane turns, in this case, into a line-fitting problem, which can be described as

$$y(n) = \hat{\mu}_{q_s}^{\gamma} x(n) + \hat{c}_{q_s}^{\gamma} + w(n), \qquad (4.17)$$

where $w(n)$ is the gaussian noise. Additionally, the determination of CRB for the slope $\hat{\mu}_{q_s}^{\gamma}$ and the intercept $\hat{c}_{q_s}^{\gamma}$ depends on the computation of 2×2 Fisher matrix that represents the parameter vector $\theta = [\hat{c}_{q_s}^{\gamma} \hat{\mu}_{q_s}^{\gamma}]^T$

$$\mathbf{I}(\theta) = \begin{pmatrix} -E\left[\frac{\partial^2 (\ln f(x;\theta))}{\partial(\hat{c}_{q_s}^{\gamma})^2}\right] & -E\left[\frac{\partial^2 (\ln f(x;\theta))}{\partial(\hat{c}_{q_s}^{\gamma})\partial(\hat{\mu}_{q_s}^{\gamma})}\right] \\ -E\left[\frac{\partial^2 (\ln f(x;\theta))}{\partial(\hat{\mu}_{q_s}^{\gamma})\partial(\hat{c}_{q_s}^{\gamma})}\right] & -E\left[\frac{\partial^2 (\ln f(x;\theta))}{\partial(\hat{\mu}_{q_s}^{\gamma})^2}\right] \end{pmatrix} \qquad (4.18)$$

The likelihood function is given as

$$f(x;\theta) = \frac{1}{(2\pi\sigma_{\text{awgn}}^2)^{\frac{N}{2}}} \exp\left\{-\frac{1}{2\sigma_{\text{awgn}}^2} \sum_{n=0}^{N-1} (x(n) - \hat{c}_{q_s}^{\gamma} - \hat{\mu}_{q_s}^{\gamma} n)^2\right\}, \qquad (4.19)$$

After solving the mathematical derivatives

$$\text{var}\,(\hat{c}_{q_s}^{\gamma}) \geq \frac{2(2N-1)\sigma_{\text{awgn}}^2}{N(N+1)}, \qquad (4.20)$$

$$\text{var}\,(\hat{\mu}_{q_s}^{\gamma}) \geq \frac{12\sigma_{\text{awgn}}^2}{N(N^2-1)}, \qquad (4.21)$$

According to (4.20) and (4.21), the variance of the estimation for both variables (the slope and interception on the y-axis) highly depends on the number of investigated points w.r.t. the noise distribution $\mathcal{N}(N_{\text{mean}}, \sigma_{\text{awgn}}^2)$, where λ is the mean and σ_{awgn} is the variance of the distribution. In this context, the forthcoming subsections show frequency and time error analyses of different applied bandwidths, i.e., different numbers of points after filtering the STFT signal. A detailed description of the derivation of (4.20) and (4.21) is presented in Appendix **A**.

Frequency Error

The influence of the SNR_{sync} on the proposed synchronization method is investigated with simulations and compared to the ones obtained from the measurements. The parameters adopted in this Chapter are equivalent to their counterparts in Chapters 2 and 3, with some adjustments according to the synchronization preamble shown in Table 4.1. A predefined number of up- and down-chirps (e.g., 8 sets) are reserved at the beginning of the transmit sequence to perform the synchronization procedure. Fig. 4.14 depicts the estimated frequency error w.r.t the coarse synchronization dependent on the SNR_{sync} level. The investigation related to Fig. 4.14(a) has been carried out with a filter that possesses only 5% of the broad analog bandwidth. The depiction in the figure can be divided into three regions to state the efficiency of the proposed method up to a limited examined bandwidth. The blue zone illustrates the minimum error achieved based on the minimum square error within the linear regression applied to the received signal after the STFT, thresholding, and clustering. On the other hand, the green field represents the zone where the proposed scheme can correct the failure that occurred. However, the green section might differ based on the designed system (the bandwidth of the adopted filter on the communication receiver). Furthermore, the red zone illustrates the case where the synchronization fails to correct the receiver misalignment. In this zone, the linear regression employed on the received signal can not extract the signal pattern correctly if the explored signal has low SNR_{sync}, which leads to a failure by the inaccurate alignment between the transmitter of one CaCS node and the receiver of another node and influences fine synchronization. In addition, although clustering can mitigate the influence of noise beforehand, the summarized clusters can not generate an accurate scheme to be adopted in the linear regression step when the noise level increases. The indicated relative frequency misalignment can be calculated as

$$\Delta Y_{\text{Filter}} = \left(\frac{Y_{\text{Filter}}^{\text{I}} - \hat{Y}_{\text{Filter}}^{\text{I}}}{Y_{\text{Filter}}^{\text{I}}} \right), \tag{4.22}$$

where $Y_{\text{Filter}}^{\text{I}} \in \mathbb{R}$ being the right alighment and $\hat{Y}_{\text{Filter}}^{\text{I}}$ the estimated counterpart. For $SNR_{sync} \leq 5$, the estimation can attain values in the vicinity of 10^{-2}; however, the presented curve in Fig. 4.14(a) is scaled to match the results in [A+22b], where the examined bandwidth was 40 MHz that restrain the number

(a)

(b)

(c)
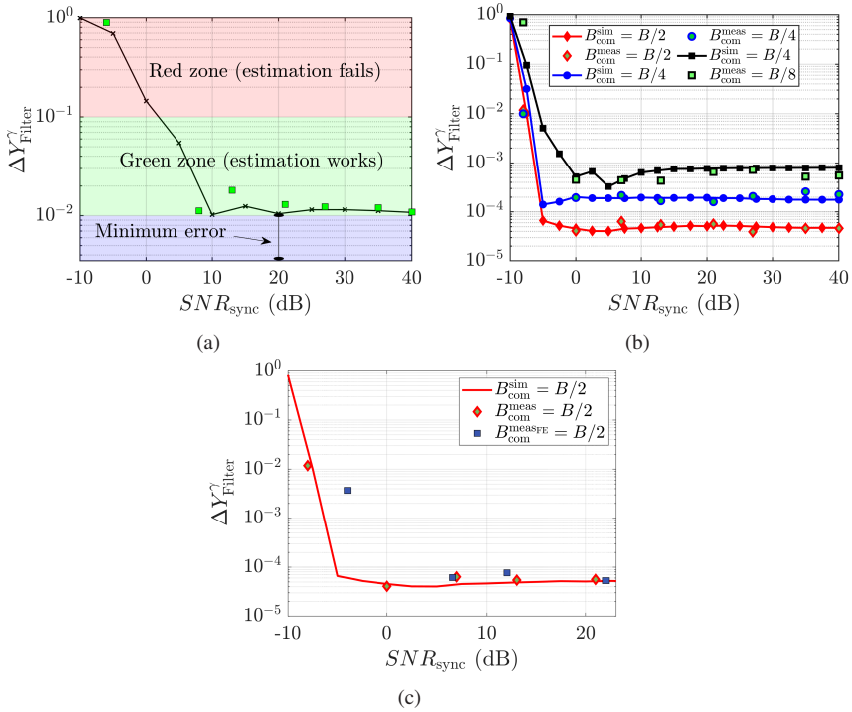
Fig. 4.14: Simulation and measurement results of the coarse synchronization verification based on the frequency error analyses. $B_{\text{com}}^{\text{sim}}$ is the examined bandwidth for simulations, $B_{\text{com}}^{\text{meas}}$ is the examined bandwidth for measurements in the baseband, and $B_{\text{com}}^{\text{meas}_{\text{FE}}}$ represents the examined bandwidth using the hardware components. (a) The frequency misalignment error is dependent on SNR$_{\text{sync}}$ for $B_{\text{com}} = B/20$. (b) Simulated and measured frequency misalignment error for different communication bandwidths $B_{\text{com}} \in \{B/8, B/4, B/2\}$. (c) Simulated and measured frequency misalignment errors related to $B_{\text{com}} = B/2$ carried out with the influence of the utilized hardware components [A+22b].

of the attained points after thresholding. Furthermore, Fig. 4.14(b) depicts the frequency misalignment error related to different bandwidths analyzed on the communication receiver of one CaCS node. For $B_{\text{com}} = B/8$ is the minimum achieved misalignment error $\Delta Y_{\text{Filter}}^{\gamma} \simeq 7 \times 10^{-3}$, while using a wider bandwidth (e.g., $B_{\text{com}} = B/2$) $\Delta Y_{\text{Filter}}^{\gamma}$ is located around 7×10^{-5}. The obtained results are compared with their counterparts analyzed during the measurement. Both

observations are almost matchable, except when the SNR_{sync} decreases, where the estimation deteriorates proportionally to the number of investigated points based on CRB. Moreover, Fig. 4.14(c) illustrates the frequency misalignment error associated with $B_{com} = B/2$ for simulations and measurements in the baseband and with the front end. The achieved results are almost congenial when $SNR_{sync} > 0$, while the error increases for the setup with the front end when $SNR_{sync} < 0$.

Time Error

Although the frame start has been detected at the beginning of the receiving procedure, the equivalent reconstruction of the points in the time-frequency plane can perform the same analysis for the time as in the last subsection for frequency. Fig. 4.15(a) presents the estimated time error $\Delta X_{\text{Filter}}^{\gamma}$ of the proposed synchronization method dependent on different values of the explored bandwidth $B \in \{B_{com} \in B/8, B/4, B/2\}$ assigned at the communication receiver of one CaCS node. The relative time misalignment can be calculated as

$$\Delta X_{\text{Filter}}^{\gamma} = \left(\frac{X_{\text{Filter}}^{\gamma} - \hat{X}_{\text{Filter}}^{\gamma}}{T_{\text{RRI}}} \right) \tag{4.23}$$

where $X_{\text{Filter}}^{\gamma} \in \mathbb{R}$ is the right time alignment and $\hat{X}_{\text{Filter}}^{\gamma}$ the estimated counterpart and the aforementioned misalignment is normalized by $T_{\text{seq}}^{\text{sync}}$ and located around 10^{-4} for $B_{com} = B/2$. Furthermore, Fig. 4.15(b) depicts the comparison between the simulated and measured results in the baseband for $B_{com} = B/8$, while Fig. 4.15(c) depicts the comparison between the simulated and measured results with the implemented front end for $B_{com} = B/2$. All the shown results are almost alike, where the deviation between the outcomes is relatively minimal compared with their counterparts in Fig. 4.14 for frequency error analyses. It is worth highlighting that the performance achieved with the proposed algorithm in Fig. 4.14 and Fig. 4.15 highly depends on the steps applied for the coarse synchronization, including the filtering, where the density of the points of the received signal filtered after the downconversion increase with higher SNR_{sync} leading to saturate the error curves around particular values in Fig. 4.14 and Fig. 4.15.

(a)

(b)

(c)
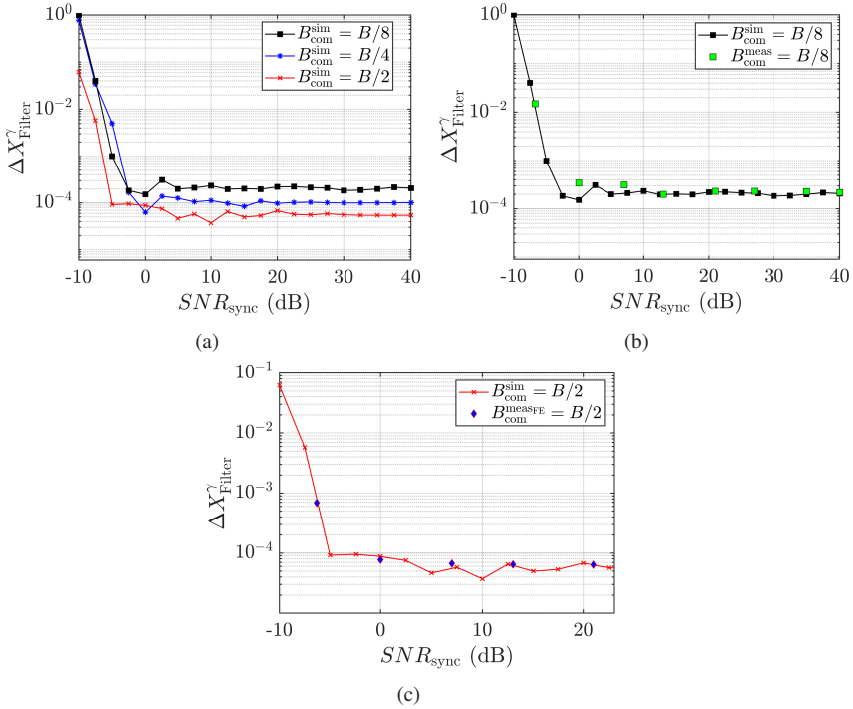
Fig. 4.15: Simulation and measurement results of the coarse synchronization verification related to the time error analyses. B_{com}^{sim} is the examined bandwidth for simulations, B_{com}^{meas} is the examined bandwidth for measurements in the baseband, and $B_{com}^{meas_{FE}}$ represents the examined bandwidth using the hardware components. (a) Simulated and measured time misalignment error related to different communication bandwidths $\{B_{com} \in B/8, B/4, B/2\}$. (b) Simulated and measured time misalignment errors when $B_{com} = B/8$. (c) Simulated and measured time misalignment errors when $B_{com} = B/2$ carried out with the influence of the utilized hardware components [A+22b].

Windowing and Thresholding

According to the implementation of the suggested synchronization method in this section, STFTs are employed to represent the analyzed signal in the time-frequency plane. STFT encompasses many features that can lead to some deviations in the results. The art of windowing operation involves many

preferences that can be adopted. In this context, three window variants (Hanning, Chebyshev, and Gaussian) are analyzed and shown in Fig. 4.16(a) for $B_{com} = B/10$. The divergence obtained from the three windows is slight and amounts to 2×10^{-3}. In addition, some other windows, such as Blackman-Harris, Kaiser, and the rectangular, lead to the same curves in Fig. 4.16(a). Besides, the applied threshold influences the number of filtered points and their orientation, particularly when SNR_{sync} has low values. Fig. 4.16(b) illustrates two curves with different thresholds ($H_2 > H_1$), where the yellow curve undergoes some saturation when $SNR_{sync} \leq 5$ because of the increment of the number of filtered points. Furthermore, if a scalable threshold is adopted in the investigation with ($H \pm \Delta H$), the best orientation of the points can be found with different values of SNR_{sync}, as shown in [SW02b], Fig. 4.16(c). Since the results in the time-frequency plane are based on the allocation of the intersecting points between two successive regression lines, the theoretical derivation of the variance is derived in Appendix A, and similar analyses can be employed for time error curves.

4.5 Conclusion of this Chapter

This chapter investigated a time-frequency approach for synchronization between two CaCS communicating nodes. The proposed approach utilizes SCA, STFT, and linear regression techniques to synchronize the communication receiver of one CaCS communicating node with the transmitter of another CaCS counterpart. Simulations and a measurement setup at 79 GHz were conducted to validate the suggested approach. The findings indicated that as the bandwidth of the investigated scene increased, the synchronization accuracy improved based on the number of detected points of each line. Due to the narrow bandwidth assigned for the communication, synchronization can be achieved with a moderate MSE error of 10^{-3} in both time and frequency values when $B_{com} = B/10$.

(a)

(b)

(c)
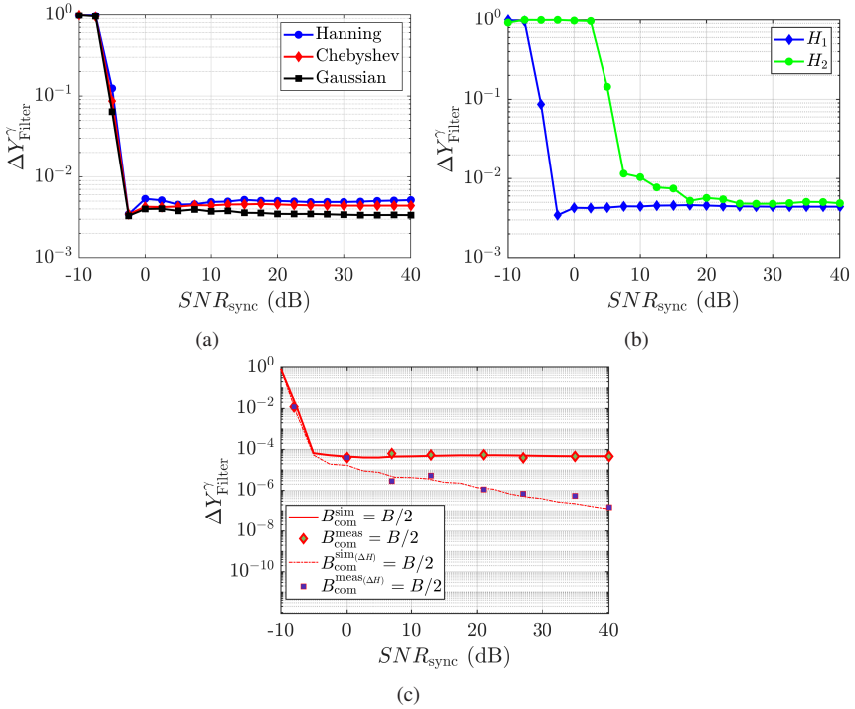
Fig. 4.16: Simulation and measurement results of the coarse synchronization verification based on the frequency error analyses based on special cases. $B_{\mathrm{com}}^{\mathrm{sim}}$ is the examined bandwidth for simulations, $B_{\mathrm{com}}^{\mathrm{meas}}$ is the examined bandwidth for measurements in the baseband, and $B_{\mathrm{com}}^{\mathrm{sim}(\Delta H)}$, $B_{\mathrm{com}}^{\mathrm{meas}(\Delta H)}$ represents the examined bandwidth relative to ΔH for simulations and measurements respectively. (a) The frequency misalignment error according to different communication bandwidths $B_{\mathrm{com}} = B/10$ with different windowing functions (Hanning, Chebyshev, and Gaussian). (b) The frequency misalignment error based on different communication bandwidths $B_{\mathrm{com}} = B/10$ with different thresholding (H_1 and H_2). (c) Simulated and measured frequency misalignment errors related to $B_{\mathrm{com}} = B/2$ carried out with the influence of the utilized hardware components and a variable thresholding function $H \pm \Delta H$.

5 Interference Detection

This chapter presents an innovative method for detecting interference between communicating CaCS nodes and analyzing its impact on synchronization in multi-user scenarios. The proposed method adopts a similar frame structure from Chapter 4 and mainly the modulation schemes mentioned in Chapter 3. Besides, a statistical framework is designed to investigate the influence of interference on communication between CaCS nodes for eminent scenarios in the automotive sector.

The main contributions of this chapter are discussed based on the following points. First, the approach for detecting interference between the communication nodes is explained. For this purpose, the chirp rates of the signals transmitted from different CaCS nodes in the examined scenario are estimated depending on fast quadratic phase transform (FQPT). Furthermore, the impact caused by interference from other nodes in the environment is analyzed. According to achieve this, two successive steps are performed. The former adopts an adjusted version of the SCA for frame synchronization to explore the consequence of the interference on time synchronization. The latter employs a correlation-based approach with reference signals based on a codebook of the assigned signals to minimize the influence of the interference on frequency synchronization at the receiver of the investigated CaCS node. As a proof of concept, measurements with the campaign performed in Section 2.7 validate the proposed method, where the resulting correlation metric and mean square error are illustrated as validation factors. Additionally, A simulator for evaluating the impact of interference on the communication link built between CaCS nodes in multi-user scenarios is presented. The simulator analyzes the interference by adopting a microscopic software tool (VISSIM) to create scenarios anticipated in automotive applications. Moreover, wave propagation uses a ray-tracer tool to represent the communication link as one or several trajectories between the nodes. Finally, the output of the wave propagation tool is evaluated and further

processed in MATLAB in terms of the relative cumulative interference BER values based on the examined scenarios.

These aspects are introduced in this section, which is mainly based on the publication from [ADM+23], [ADN+23] with reformed and reused texts and figures © [2023] IEEE.

5.1 Interference in Automotive Scenarios

Since each vehicle in ADAS and HAD applications should comprise several radar sensors to achieve the requirements of autonomous object detection, interference events can emerge caused by the signals transmitted from other sensors in the environment [A+21], [HSZ18], [K+21a], [S+15], [Sch17]. A possible approach to minimize the influence of interference is to include communication symbols within radar signals so that the sensors can contact each other beforehand to avoid potential overlappings during the transmission [GdO+21] [SW11], as shown in Chapter 3. The modulation schemes presented in Section 3.2.1 and Section 3.2.2 are convenient approaches, where the chirps are modulated in small sectors so that the impacts on the radar procedure stay limited and the amount of transmit data can satisfy the requirement of the applied service [ANWZ19]. Although the bandwidth utilized for communication purposes is narrow, the interference can impact the demodulation scheme and the synchronization in the former step. Since many studies have introduced the impact of interference on communication links, this chapter focuses more on its effect on synchronization within the proposed system. Since interference can disrupt synchronization by introducing noise or other sources of distortion into the system, the timing errors or frequency shifts can considerably reduce the quality of the examined communication link. Therefore, this chapter analyzes the impact relative to the overlapping degree of interference in the examined scenario.

5.2 Interference Detection and Synchronization

Although a chirp time duration within CaCS-based radar systems can be occupied by a limited number of coexisting signals [TTRW20], [DK90], [FBDM15],

[Kun12], [TMMW20], [UMW$^+$22], [Dit20] the incidence of interference can restrict the synchronization and communication purposes desired from the designed system. Fig. 5.1 shows an exemplary case of the distribution of several signals within the time-frequency plane, where the worst incidence emerges when the composition of up- and down-chirps, dedicated to synchronization, in each transmit signal is shown in the same time duration. The signals are depicted by straight slopes of up- and down-chirp dedicated to synchronization. The first composition of up- and down-chirps represents the desired pattern, while the second counterpart represents the first interferer. Its equivalent composition has the narrowest bandwidth and is displayed as a steep slope that rises sharply in frequency over a short time duration. Besides, the third signal represents the second interferer, which has the widest bandwidth and is illustrated as a broader signal that rises more gradually in frequency over a considerable chirp duration. According to this, the aforementioned patterns are depicted with arbitrarily different chirp rates $\{\mu_1, \mu_2, \mu_3\}$, signal durations $\{T_{chirp_1}, T_{chirp_2}, T_{chirp_3}\}$, and bandwidths $\{B_1, B_2, B_3\}$. The suggested communication methods in [AN-WZ19], [A$^+$22a] apply a limited-band communication receiver related to the current radar sensors in the automotive industry so that only the sector between the dashed lines in Fig. 5.1 within B_{com} is further evaluated in the signal processing chain. However, interference events between the aforementioned chirp compositions can be destructive and significantly impact the synchronization. For this purpose, this section presents the modified receiving procedure, presented in Chapter 4, in case of coexistence of interference, as depicted in Fig. 5.2. First, the signal is received, which applies the frame structure introduced in the last chapter. Second, if no *A priori* information associated with the transmit signals in the environment is available, the synchronization can be applied based on the linear regression approach, as shown in Section 4.4.1. On the other hand, if *A priori* information is unrestricted, a scheme involving two successive steps can be adjusted w.r.t examined scenario. Since other CaCS nodes transmit their signals within the same bandwidth, the interference can be detected according to FQPT. Next, a correlation-based method can be implemented to extract the information of the desired pattern.
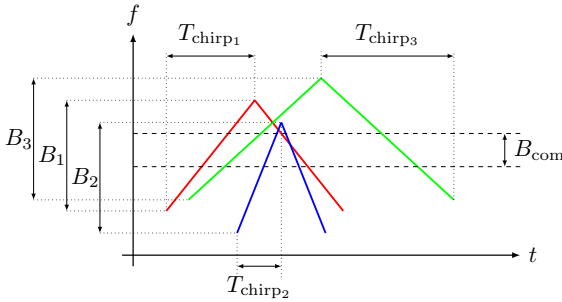
Fig. 5.1: Visualization of several chirp signals with different parameters in the time-frequency plane: chirp rates $\{\mu_1, \mu_2, \mu_3\}$, time durations $\{T_{\text{chirp}_1}, T_{\text{chirp}_2}, T_{\text{chirp}_3}\}$, and bandwidths $\{B_1, B_2, B_3\}$ [ADN$^+$23].

5.2.1 Linear Regression Approach

According to the synchronization method presented in Chapter 4, the signal pattern is predicted at the communication receiver to synchronize it with the transmitter of another CaCS node. Since the current radar manufacturers adopt different parameters, frequency and time shifts are anticipated at the communication receiver. Moreover, the proposed synchronization method is based on the slope estimation applied by STFTs and linear regression to represent the complete desired signal pattern and accomplish the coveted performance for the chosen application in automotive scenarios. In this context, when different signals are simultaneously transmitted within the bandwidth of the communication receiver, all different signal patterns should be estimated at the receiver node so that the desired signal can be resolved and recovered if the information of the chosen slope is shared. However, when the number of interfering signals increases, the complexity of applying linear regression in a one-time duration tends to be exacerbated by the factor $O(\Upsilon_{\text{norm}}^3)$, where Υ_{norm} is the number of features in the normal equation of the linear regression, as investigated in the study in the last chapter.

Furthermore, Fig. 5.3 illustrates the capability of the proposed synchronization approach to recreate the desired signal pattern despite the coexistence of other signals in the surroundings. The simulations are applied depending on the number of coexisting signal patterns N_i carried within the entire bandwidth B of
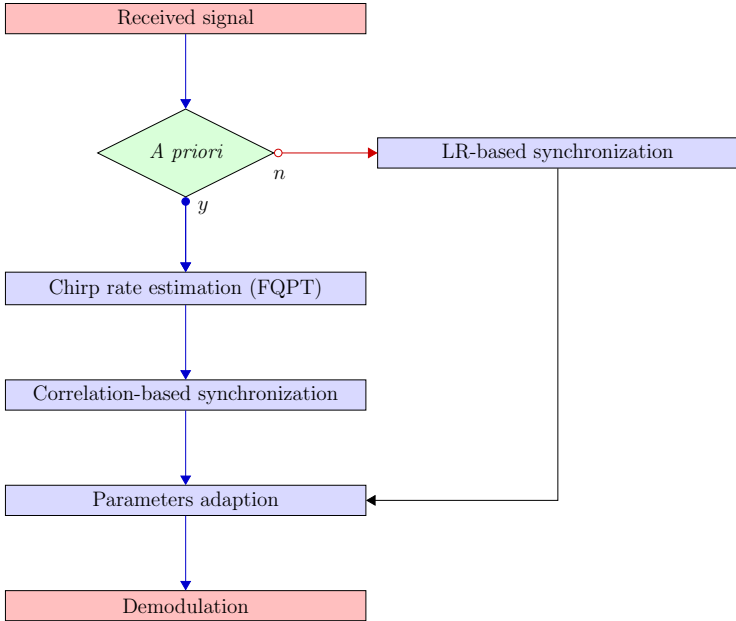
Fig. 5.2: Receiving procedure of the communication receiver, including the steps of the proposed interference detection approach and the demodulation [ADN+23].

the radar-communication system, as depicted in Fig. 5.3(a). In this context, since the proposed method employs a partial bandwidth B_{com} to estimate the desired signal pattern, the probability of deterioration in performance relative to the applied algorithm is limited. Furthermore, the CDF represents the cumulative misalignment of the wrong pattern formation (failure of synchronization), as shown in Fig. 5.3(b), where not every coexisting signal transmitted within the bandwidth B should interfere with the desired signal in B_{com}. In light of the linear regression described in Section 4.4.1, the pattern formation, in this case, also depends on the distance assessment between the up- and down-seeded intersections, as presented in Chapter 4.
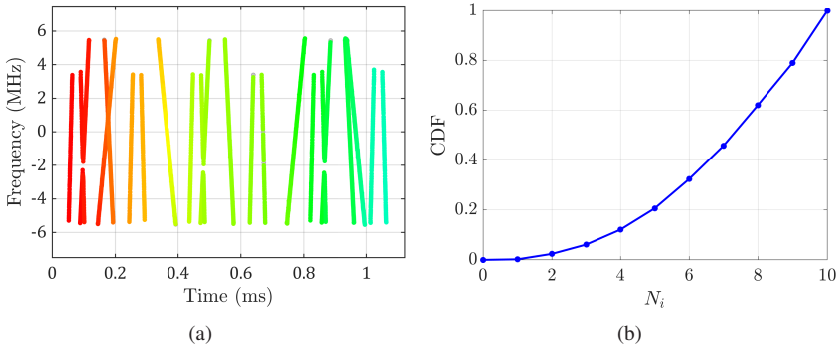
Fig. 5.3: Simulation results for the CDF regarding synchronization failures in multi-user scenarios with N_i number of users. (a) Exemplary cluster allocations in a scenario with multiple coexisting signals. (b) CDF reliant on the number of coexisting signals within the complete bandwidth of the system [A+22b].

5.2.2 Correlation Approach

Another alternative approach to synchronize the transmitter and receiver of communicating CaCS nodes in an interfering environment is to create a codebook that incorporates the parameters of the signals. Firstly, based on the chirp rates estimation of the transmit patterns, whose slopes are uniquely assigned among the predetermined codebook. Second, correlation can be applied to the chosen detected patterns within the codebook to synchronize the receiver of one CaCS node with one of the desired transmit signals for communications.

Chirp Rate Estimation

Within the structure illustrated in Fig. 5.2, it is possible to detect all the signals that coincide within a given period T_{chirp} if each signal has a distinct chirp rate. This approach utilizes FQPT [IAMH96] to estimate the detected chirp rates. The FQPT is a modified version of the conventional FFT designed to assess the received signal parameters within the communication bandwidth. This process is illustrated in Fig. 5.4. Only N samples of the received signal are employed to estimate chirp rates after filtering it about the communication
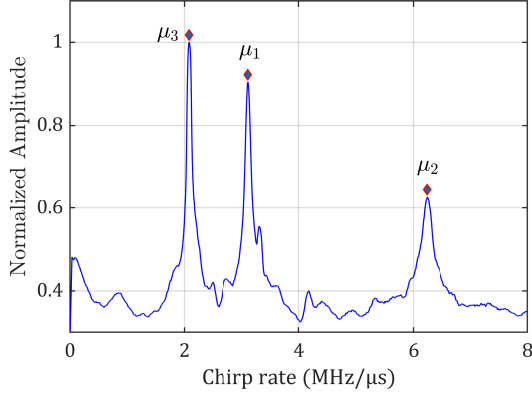
Fig. 5.4: Exemplary detection of three different chirp signals with unique slopes $\{\mu_1, \mu_2, \mu_3\}$ [ADN$^+$23].

methods presented in 3.2.1 and 3.2.2. The parameters can be evaluated regarding the following equation

$$(\mathbf{Y}_{\text{cr}})_{k,\kappa} = \sum_{n=0}^{N-1} (y_{q_s})_n \, W_N^{\kappa \Lambda n^2} \, W_N^{kn} + w_n \qquad (5.1)$$

where $(y_{q_s})_n \in \mathbb{C}$ is the sampled signal at the output of the filter dedicated to the modulation bandwidth B_{com}, $(\mathbf{Y}_{\text{cr}})_{k,\kappa} \in \mathbb{C}$ represents the output of the estimator. $W_N^{\kappa \Lambda n^2} = e^{-j\frac{2\pi\kappa\Lambda}{N}n^2}$ represents the chirp function and $W_N^{kn} = e^{-j\frac{2\pi kn}{N}}$ is the fourier factor. w_n is the noise, $k, n = 0, ..., N-1$ and $\kappa = 0, ..., \frac{N}{\Lambda} - 1$ defines the chirp index, where $\Lambda = 2^{-\varrho}$ is an incremental step introduced for the estimation of the chirp rates dependent on the slopes assigned in the investigation, and $\varrho \in \mathbb{Z}$.

Synchronization based-Correlation

After detecting the number of signals overlapping in the same time duration, the beginning of the frame is detected based on a modified version of the SCA [SC97], as proposed in Chapter 4. Since the scenario is impaired by inter-

fering signals, the proposed algorithm is explored based on [MS07] to analyze the impact of interference on frame synchronization. Next, a set of different up- and down-chirps are generated using the parameters of the suggested codebook within the sampled receiver bandwidth B_{com}. The received signal is correlated with each set of up- and down-chirps deployed from the codebook. Fig. 5.5 depicts an exemplary output of the correlator of the desired signal that should be synchronized at the receiver side to deliver the communication data. The frequency offset $f_{shift}^{(i)}$ of the first set can be calculated dependent on the difference between the maximum correlation peaks of the up- and down-chirps ΔC_i, which are represented in samples

$$f_{shift}^{(i)} = \left(\Delta C_i \cdot \frac{1}{f_s} - T_{chirp} \right) \cdot \mu \qquad (5.2)$$

where μ is the chirp rate, T_{chirp} is the chirp duration and f_s represents the sampling frequency. Furthermore, a modified version of the study in [BMKCF20] is adopted to accomplish high accuracy in terms of frequency estimation. For accurate time estimation in each time duration, the delay τ_{shift} in samples relative to each correlation peak can be calculated by

$$\tau_{shift}^{(i)} \cdot f_s = C_i - \left(\frac{f_{shift}^{(i)}}{f_s} \right) \qquad (5.3)$$

Measurement Results for Interference Detection

The measurements are conducted at a laboratory at IHE. A SoC platform is employed in the baseband to emulate the transmitter, the interferers, and the receiver of the CaCS-based [DNPZ22], as described in Section 2.7. The measurements adopt various parameters adopted by current automotive radar sensors. For this purpose, the maximum analyzed bandwidth is assigned to 1 GHz, and the maximum sampling frequency amounts to 100 MHz. According to [TTRW20] regarding the level of interference, the duration of the investigated signals has uniquely varied between 10 µs and 100 µs with a maximum degree of interference $\kappa_{int} = 3$ representing the number of interferers in the same time duration spaning together with the desired signal. Fig. 5.6(a) and Fig. 5.6(b) depict the results corresponding to the proposed synchronization method after detecting
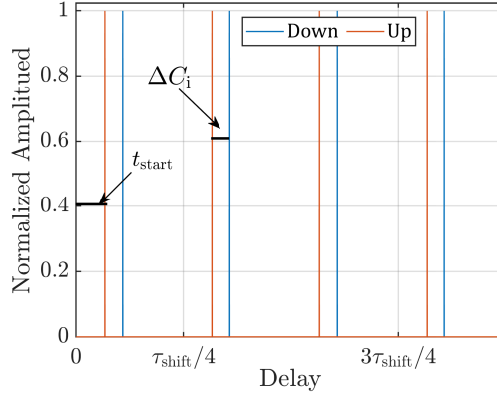
Fig. 5.5: Exemplary time shift τ_{shift} at the output of the correlator for four successive up- and down-chirps, composing one preamble dedicated to synchronization correlated with the reference signals. Red peaks represent the output of the correlator concerning the up-chirps, whereas blue counterparts are the output related to down-chirps. For simplicity, only the peaks for one assigned signal are illustrated [ADN+23].

the number of interferers within the examined scenario according to (5.1) and Fig. 5.5. In Fig. 5.6(a), the correlation metric ME relative to the modified SCA for frame synchronization is visualized for several cases with the same time shift dependent on the degree of the occurred interference, where κ_{int} represents the number of interferers contributes to the transmission with the scenario. As can be seen, if the setup does not undergo any interference, the normalized value of ME reaches its maximum. However, the value decreases gradually to the contributed interference, where the employment of unique slopes reduces the impact of the interference on the desired signal. Additionally, Fig. 5.6(b) illustrates different curves w.r.t the examined frequency synchronization between two communicating CaCS-nodes. The more interference persists in the setup, the more deterioration the synchronization can suffer relative to the mean square error (MSE). If $\kappa_{int} = 1$, the synchronization can be accomplished among the assigned SNR_{sync} values (sync, in case of synchronization). On the other hand, If $\kappa_{int} = 3$, appropriate values of SNR_{sync} are required to conduct the information of the frequency synchronization, where the maximum value of the normalized ME, in Fig. 5.6(a), is less than (0.3) and MSE, in Fig. 5.6(b), is less than (10^{-6}) for $SNR_{sync} \leq 8$ dB. Besides, the deviations witnessed in the curves under $\kappa_{int} = 3$ interference conditions provide valuable insights into the
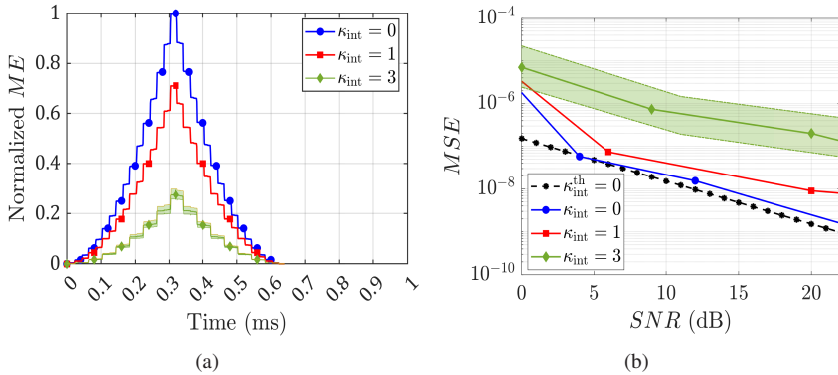
Fig. 5.6: Measurement setup and results for time-frequency synchronization according to the proposed method. Dashed black: theoretical curve for synchronization without interference $\kappa_{\text{int}}^{\text{th}} = 0$, blue: measured curve according for synchronization without interference $\kappa_{\text{int}} = 0$, red: synchronization with one interferer $\kappa_{\text{int}} = 1$, and green: synchronization with three interferers $\kappa_{\text{int}} = 3$. (a) Remaining time error based on frame synchronization w.r.t correlation metric (ME). (b) Remaining frequency error based on normalized MSE corresponding to f_{s} [ADN$^+$23].

proposed approach. This deviation is according to the position of the signal of the interferer in the time-frequency plane, which can be further analyzed along with the CI based on Fig. 5.6.

5.3 Statistical Analyses

Since automotive scenarios comprise vehicles with multiple radar sensors, interference events can influence the communication signal and the radar counterpart in CaCS-based radar systems. Therefore, this section introduces a statistical case study where several sensors transmit signals analyzed by a simulator for CaCS-based radar systems in multi-user scenarios. The simulator is designed based on the software VISSIM developed by the company PTV [PTV14] to represent statistical investigations for different traffic scenarios in a facile environment and import them in a convenient form for further processing, dependent on the objective of the study [Mes20].

5.3.1 Simulation Setup

Fig. 5.7 depicts the simulation setup applied in this study to investigate the interference impacts on the communication symbols transmitted between the communicating radar sensors in the environment for automotive applications. Additionally, the influences from the radar hardware and a typical radio channel between vehicles are included in the simulation, similar to [Sch17]. The simulator involves mainly the following steps. A traffic flow simulator VISSIM is adopted to generate stochastically simulated scenarios over a fixed number of snapshots N_{snap} relative to the examined time. Next, a vehicle selector approach is assigned in MATLAB to randomly select the communicating vehicles during the assigned snapshot $n_{snap} \in \{0, 1, 2, \ldots, N_{snap} - 1\}$ and perform the communication link according to the explored scenario. In this term, the accessibility of communication links is verified to ensure time efficiency among the simulator. If the communication link is not performed, n_{snap} was assigned to the next step as $n_{snap} = n_{snap} + 1$ to execute the following snapshot. Furthermore, the information exported from the simulator is inserted into the subsequent step to accomplish wave propagation. This block is implemented by a ray-tracing tool programmed at IHE. The ray tracer presents all the propagation trajectories between the communicating vehicles and each interferer involved in the scenario. At the output of the ray tracer, the delay, Doppler shift, and attenuation for all the paths are carried out. The signal processing using MATLAB applies the parameters to the received signal to estimate the effects that occurred on it. Finally, the received signal is demodulated regarding the investigated modulation method in [ANWZ19]. Subsequently, the next time snapshot n_{snap} is selected by the vehicle selector, and the process is repeated till the end of the time snapshots. Finally, the results can be sent to the output for evaluation according to the desired parameters.

5.3.2 Adopted Scenarios

The automotive scenarios include many case studies. However, two main classes of automotive schemes are considered in this section. First, straight lanes are employed in the setup according to the number of traffic lanes involved in each scenario. In the framework of the simulator, single, two and three-lane schemes are investigated, as depicted in Fig. 5.8(a) and Fig. 5.8(b). Second,
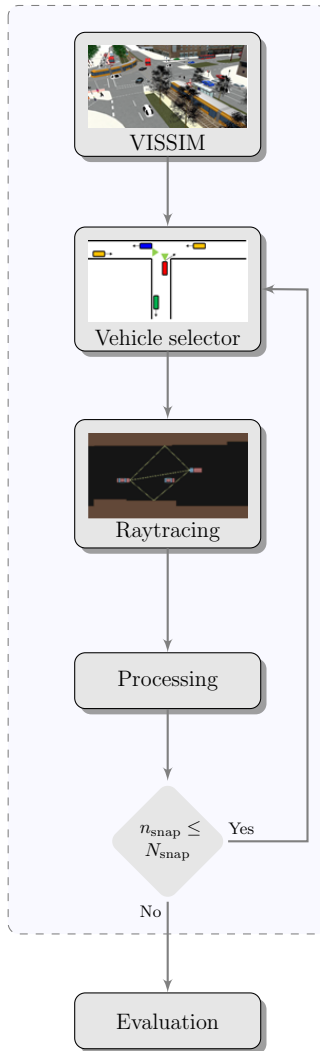
Fig. 5.7: Simulation setup for automotive scenarios. The simulator involves a scenarios maker VIS-SIM, vehicle selector, ray-tracing approach, and signal processor in MATLAB [ADM+23].
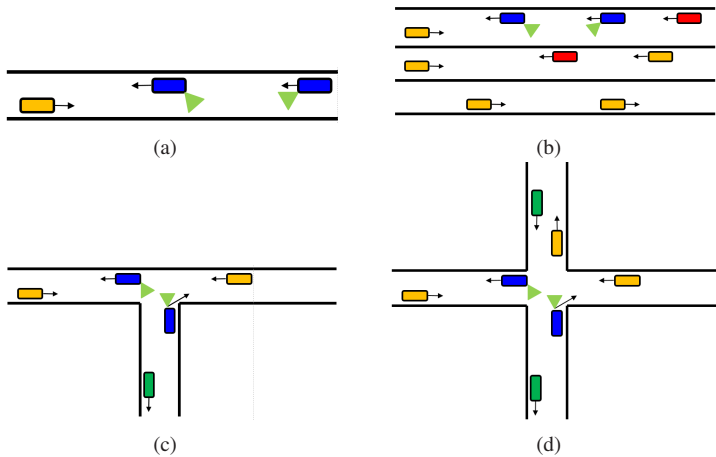
Fig. 5.8: Exemplary straight lane and crossroad scenarios adopted by the simulator: (a) single-lane scenario, (b) three-lane scenario, (c) T-crossroad scenario, and (d) X-junction scenario. Blue vehicles represent the communication link, while their counterparts with other colors act as interferers. Light-green and red vehicles are potential candidates in the vehicle selector for the next snapshots, and light-green triangular represent corner radars equipped with communication [ADM⁺23].

crossroad scenarios are frequent on the roads. Therefore, they are analyzed in two terms, T-crossroad and X-junctions, as illustrated in Fig. 5.8(c) and Fig. 5.8(d). Furthermore, the simulations were implemented for one hour in a step of one second, and the scenarios adopt a flow of 500 vehicles/h with an average velocity of 50 km/h, as adopted in [Sch17].

5.3.3 Simulation Results

The simulation involves various parameters adopted by current radar sensors for automotive applications. For this purpose, the analyzed carrier frequency is applied within the band $(76 - 81)$ GHz with a varying bandwidth from 200 MHz to 2 GHz, and the maximum sampling frequency amounts to 100 MHz. The chirp duration is adopted to vary between 10 µs and 100 µs, and the maximum frame duration that contains all the chirps is assigned to 20 ms. In terms of

the transmit power, the selected nodes are determined by a value in the range $[-5,+10]$ dBm with a maximum equivalent isotropically radiated power of 40 dBm. Additionally, the effects of the interference are evaluated relative to the average received interference power ($\overline{P}_{RI}$) as performed in [Sch17]. The employment of $\overline{P}_{RI}$ allows better comparability of scenarios that adopt a narrow band receiver architecture, where such a calculation of this parameter can be found in commercial wave propagation programs [AWE14]. For the synchronization, a preamble of 8 up- and down-chirps is reserved, as presented in the last chapter. In addition, the aforementioned preamble is deployed for detecting the number of interferers in one snapshot [A+22b]. Fig. 5.9 depicts an exemplary output of the simulator based on the desired scenarios investigated in this paper. Both main classes have been introduced, including straight lane and crossroad scenarios. Fig. 5.9(a) depicts the distribution of interference events that clearly shows the probability of their occurrence in both categories of examined schemes. In this term, T-crossroad scenarios undergo more interference than the simple-lane case, where the interference can be three times higher within the similar conducted time snapshots. In addition, Fig. 5.9(b) illustrates the relative CDFs of the interference that occurred in the examined scenarios with several penetration rates (PRs). The penetration rate represents the level of the occurred interference and is assigned within the range (0–100) %. In this term, the receiver of one CaCS node undergoes more interference when PR = 100 %. Besides, the impact of interference events in T-crossroad scenarios is explicitly higher with 10 dB compared to the single-lane scheme. Since the receiver bandwidth is narrow, the impact of interference when PR = 25 % is limited. Furthermore, Fig. 5.9(c) illustrates the impact of interference on X-junction scenarios compared to single-lane, T-crossroad, and congested three-lane counterparts, where X-junction scenarios undergo an advanced degree of interference. Moreover, Fig. 5.9(d) depicts the fickleness in BER behavior with two different ($PR = 100$ %) for T-crossroad, congested three-lane, and X-junction scenarios. As soon as PR tends to reach 100%, the probability of achieving ($BER = 0$) decreases to 83%, and this amount is distributed among other BER values with higher error rates. For congested three-lane scenarios, the likelihood of ($BER = 0$) decreases with $\simeq 7$% compared to its counterpart for T-crossroad scenarios. In addition, the probability of ($BER = 0$) decreases more in X-junction scenarios and reaches 60%, where $\overline{P}_{RI}$ increases in this case.
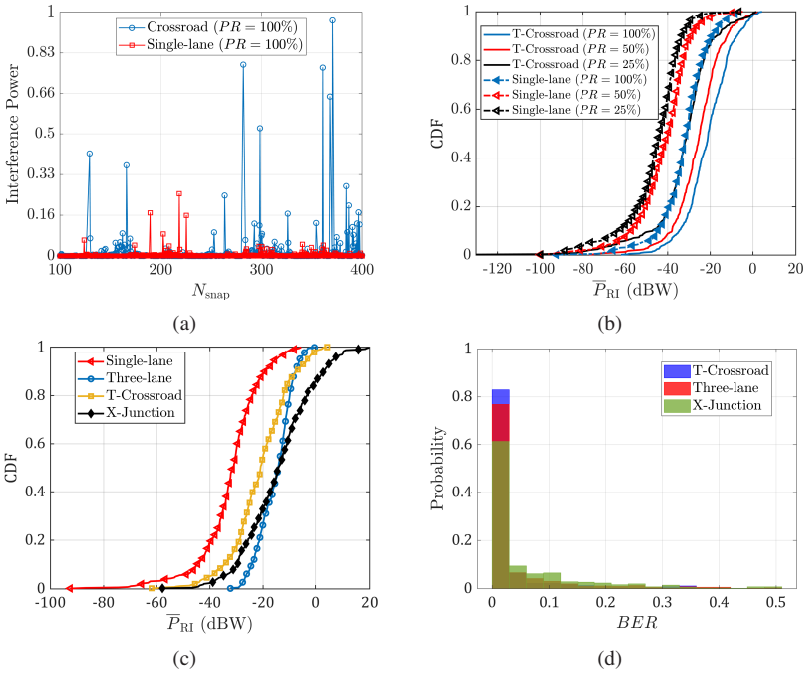
Fig. 5.9: Exemplary results of the simulator. (a) the distribution of interference events based on the number of snapshots, where the respective magnitude is normalized by the maximum received interference value. (b) The CDF of the average received interference power $\overline{P}_{RI}$ for single-lane and T-crossroad scenarios with several ($PR \in \{0\,\%, 50\,\%, 100\,\%\}$) values. (c) The CDF of $\overline{P}_{RI}$ single-lane, three-lane, T-crossroad and X-junction scenarios with ($PR = 100\,\%$). (d) the probability in histogram of BER relative to T-crossroad, three-lane and X-junction scenarios for ($PR = 100\,\%$) [ADM+23].

5.4   Conclusion of this Chapter

This chapter presents a time-frequency method for interference detection and its influence on the synchronization in CaCS systems is presented. The proposed method adopts FQPT to detect the overlapping signals in the same time duration and a correlation-based approach for time-frequency synchronization. The more interference persists in the investigated time duration, the more deterioration the synchronization can endure. Since the bandwidth assigned for the communication is narrow, the synchronization can be accomplished with a moderate grade of coexisting interference $\kappa_{\text{int}} \leq 3$. Furthermore, a simulator for CaCS systems in multi-user automotive scenarios is presented. The simulator analyzes the influence of interference events on the transmitted communication symbols integrated within chirp sequence signals and adopts a statistical tool to create scenarios between randomly communicating vehicles. Since the bandwidth assigned for communication is narrow, single-lane setups undergo limited impact of interference on the detection of the communication data compared with their three-lane, T-crossroad, and X-junction counterparts. Besides, the communication links built up in X-junction scenarios can endure more interference and information loss for BER = 0 compared with three-lane and T-crossroad counterparts.

6 Conclusion

This thesis proposes and designs a novel concept for communication-assisted chirp sequence radar (CaCS) systems. These systems can merge communication data within the same radar signal but solely with a narrow bandwidth and limited time duration. For this purpose, the sampling rate of the ADC at the receiver side can remain fixed. This issue is explicitly critical because fast and high-resolution ADC converters are expensive. In this term, an advanced architecture consisting of a separate narrowband communication receiver at 79 GHz combined with the classical CS-based radar transceiver is evolved. Specifically, the radar transmitter sends both radar and communication patterns, but two separate receivers for each term are adopted. Inspired by the proposed novel concept for CaCS systems, two novel techniques for modulating the data within each chirp are proposed. The first partially modulates the chirp, and the latter adopts LoRa rearrangement of the chirp segments. Both communication techniques analyze a narrow bandwidth to reduce the impact on the radar quality. Moreover, a synchronization approach for the communication transceiver is designed. This approach utilizes image-like synchronization algorithms based on STFT and LR, giving the narrowband communication receiver the advantage of remapping their communication receivers in the time-frequency plane to predict the pattern of the entire signal. Besides, these algorithms can help analyze the impact of interference on the synchronization scheme, where the slopes of the signals can be estimated by LR or using a correlation-based method if *a priori* information of the investigated signals is considered.

Following the aforementioned aspects, the elaborated achievements of this work are elucidated below according to the detailed findings in each chapter.

Signal model and communication methods

Chapter 2 performs a detailed analysis of the chirp signal employed in automotive applications. A well-known 2D-FFT is adopted for detecting the range and velocity of observed targets in the surroundings. Seeking to mitigate the interference between radar sensors that occupy the same spectrum, the integration of communication data within radar signals was introduced as CaCS-based radar in Chapter 3. Two communication techniques were developed during the research time. First, the communication data can be partially integrated within a limited bandwidth $B_{com} \ll B$ that is required for the radar signal so that the influence on the radar quality can be limited during the measurement within an equivalent duration of the whole transmit signal. Second, another technique to modulate the radar signal is to divide each chirp into two sectors dependent on preplanned time and frequency shifts. This approach is introduced as TFSK in Chapter 3 and is initially derived from the LoRa scheme used for long-range communication. It is shown that the TFSK technique can require sampling a massive part of the employed bandwidth dependent on the transmit signal. Therefore, an evolved PPM-based approach is designed to conform to the limited bandwidth that current sensors could sample. Furthermore, due to the slight transition between the two sectors of each chirp in TFSK modulation, a modified version of the conventional 2D-FFT should be implemented to recompense the range-Doppler errors. The errors mentioned above are considerable when the targets occupy high-velocity values in the surroundings. For both communication techniques, the receiver concept is suggested to demodulate the communication symbols transmitted from one CaCS node to the communication receiver of another node within a narrow band compared to the whole utilized radar bandwidth. In connection with the findings related to the mentioned communication techniques, the following points were observed:

- PM and TFSK are applied to the equivalent duration of the radar signal. Therefore, there is no impact on the maximum velocity of objects detected from radar sensors compared with the concept, where the radar and communication are active in consecutive time durations.
- The aforementioned modulation schemes do not restrict the use of MIMO specifications to estimate the angle information of the detected targets in the surroundings as applied in traditional CS without communication features.

- Although the chirp is modulated with communication symbols, the modulated section can be used for radar signal processing in the partial communication method in trade-off with the PSLR and ISLR levels, which proportionally increases in the TFSK method with the adopted modulation order because of the transition between the two sectors of each chirp. In PM-based modulation method, PSLR level detoriates about 2 dB if the modulation section $T_{com} = T_{chirp}/4$ and ISLR 5 dB for the same duration. On the other hand, the TFSK-based method undergoes a larger impact with 8 dB on average for both PSLR and ISLR according to the assigned transition between the two parts of the modulated chirps.
- The influence of the channel on the proposed communication methods is investigated in Chapter 3. Since the work presents the communication between the radar sensors for automotive scenarios, multipath effects (at least the reflection from the ground) can impact the detection of communication symbols transmitted from one CaCS node to the receiver of another CaCS system. Given the PM-based modulation, it has been shown that the number of communication symbols transmitted from one CaCS system is limited, reliant on the length of the channel impulse response associated with the transmission for each transmitted communication symbol, and it is possible to send one communication symbol per sample if the criteria are fulfilled (e.g., $N_{com} = 64$ in Chapter 3). Besides, the BER curves with a different number of communication symbols are illustrated, showing slight deviation if each sample point represents one symbol, particularly in dual mobility scenarios. On the other hand, using the TFSK-based method, the influence of the channel on the communication symbols can be limited since each chirp stands for only one communication symbol.

Synchronization

In Chapter 4, a preamble-based synchronization method was proposed for CaCS systems, presented in Chapter 3, that operate in $(76 - 81)$ GHz, where the investigated spectrum is assigned to radar signals relative to standardization from ITU and 3GPP. The suggested approach relies on an innovative two-stage approach to synchronize the transmitter of one CaCS node and the receiver of another node. The former stage applies coarse features, reallocates the carrier frequency at the receiver, and corrects eventual time shifts during the trans-

mission using the following schedule. The latter, in turn, applies an equivalent range-Doppler estimation in FMCW radars to amend additional time and frequency offsets that have not been compensated during the coarse counterpart. The main observations, dependent on the proposed synchronization method, can be formulated according to the following points:

- The synchronization between the communicated radar sensors can be achieved without previous knowledge of the signal parameters. However, the acquaintance of the frame structure applied during the transmission is required by all the communicated sensors, i.e., a well-known preamble should be transmitted at the beginning of each signal block before the signal dedicated to radar measurement and communication and radar sensors that aim to communicate should know the composition of the signal transmitted for radar and communication purposes.
- Due to implementing an image-like processing scheme, which includes several STFT transforms and an LR-based algorithm, the complexity of the synchronization method increases compared with a possible matched filter approach, where only FFT operations are required. In this term, previous knowledge of the signal parameters should be available before commencing with the synchronization in the case of the matched filter. However, authorized and approved regulation between the radar manufacturers is necessary for the latter option.
- The applied window in STFT and the proposed threshold values influence the result obtained in the next step when the chirp slope is estimated dependent on the LR-based approach. Therefore, an investigation for different bandwidths and threshold values is carried out in Chapter. 4.
- An adaptive applied threshold can improve the transition of the error curves between low and high SNR values, leading to linear fitting characteristics.

Interference in Multi-User Scenario

Additionally, Chapter 5 explores expanding the investigated systems to multi-scenario cases. Typical automotive scenarios include many radar sensors that can work within the same bandwidth and time duration, leading to interference between the signals transmitted in the surroundings. According to this, the following remarks have been observed.

- Since the proposed communication methods in Chapter 3 carry the data partially (e.g., on 10% of the radar bandwidth B), it has been shown that the probability of interference over communication data can be limited. Besides, only a fraction of the coexisting signals N_i within the radar bandwidth B can influence the communication symbols carried within the B_{com}.
- A critical case concerning the proposed synchronization method, presented in Chapter 4, is the STFT and LR applied to estimate the exact slope of the transmit chirps. If the number of the investigated overlapping signals increases, the algorithm undergoes imprecision in inferring the desired signal pattern because of the growing error based on the linear regression.
- If the parameters of signals operating in the surroundings are known, a matched filter-based approach can be implemented to synchronize the receiver with the desired signal.

Furthermore, a statistical tool (VISSIM) is adopted to create dynamic and representative automotive scenarios, including lane, T-crossroad, and X-junction scenarios. Since the communication receiver bandwidth is narrow, it is noted that the communication links established exhibit greater resilience to interference and loss, even under conditions if PR level is not high, in contrast to their $PR = 100\%$. Besides, congested three lanes can undergo more interference compared to their X-junction and T-crossroad counterparts.

Demonstration and Measurements Verifications

As a proof of concept, a demonstrator at one of the laboratories of IHE was built to verify communication, synchronization, and interference detection methods proposed between two CaCS nodes. The demonstration is the first one so far to the knowledge of the author that represents the communication carried in $(76-81)$ GHz integrated within the radar signals with active microwave components. According to the information above, the following remarks have been observed.

- The demonstrator can be arranged with a low-cost approach by encompassing two subharmonic mixers in the range $(29-43)$ GHz to up- and downconverts the desired signal based on the presented CaCS system in

Chapter 3 and Chapter 4. The idea behind involving two subharmonic mixers is to limit the frequency required from the local oscillator according to the specifications of the equipment accessible at IHE.

- A frequency multiplier is applied beforehand to quadruple the transmit frequency and reach the range of the employed mixers so that the required frequency from the signal generator on the transmitter side (e.g., $f_{LO,max} = 10\,\text{GHz}$). Furthermore, amplifieres are adopted at $(71-86)\,\text{GHz}$ to strengthen the radio signal investigated within the demonstrator.

- The transmitter and receiver of CaCS-based nodes can be designed dependent on an SoC platform Zynq (ZCU111). In addition, an RTS can be integrated within the SoC to emulate the investigated targets with different range and velocity cells and the delays for the communication channel presented in Chapter 3.

In summary, as explored in this thesis, integrating communication data into conventional CS-based radar systems exhibits promising potential for enhancing current radar functionalities in automotive scenarios, especially in ADAS and HAD applications. In addition, the novel communication receiver concept discussed herein presents an innovative approach for facilitated integration, requiring only low-cost technological advancements. The proposed concept obviates the need for an external, standalone communication system based on mobile networks. This forward-looking concept emphasizes the potential of CS-based radar systems with communication integration to play a fundamental role in shaping future automotive safety standards and upcoming evolved technologies such as 6G networks.

A   Appendix

A.1   A Point of Intersection Estimator

The derivation of the intersection point of two straight lines is a fundamental concept in analytic geometry. Considering two lines with equations in the form of

$$\hat{y}_0 = \mu_{q_c}^{\gamma} \hat{x}_0 + c_{q_c}^{\gamma}, \tag{A.1}$$

$$\hat{y}_0 = \mu_{q_c+1}^{\gamma} \hat{x}_0 + c_{q_c+1}^{\gamma}, \tag{A.2}$$

where $\mu_{q_c}^{\gamma}$ and $\mu_{q_c+1}^{\gamma}$ represent the slopes of the lines, and $c_{q_c}^{\gamma}$ and $c_{q_c+1}^{\gamma}$ denote their respective y-intercepts. In this term, the two equations can be solved for x to find the intersection point.

$$\mu_{q_c}^{\gamma} \hat{x}_0 + c_{q_c}^{\gamma} = \mu_{q_c+1}^{\gamma} \hat{x}_0 + c_{q_c+1}^{\gamma}, \tag{A.3}$$

By equating the abovementioned equations, x can be isolated and determine its value. Rearranging the equation

$$\hat{x}_0 = \frac{c_{q_c+1}^{\gamma} - c_{q_c}^{\gamma}}{\mu_{q_c}^{\gamma} - \mu_{q_c+1}^{\gamma}} = -\frac{\Delta c^{\gamma}}{\Delta \mu^{\gamma}}, \tag{A.4}$$

Dividing both sides of the equation by $\Delta \mu^{\gamma}$, $\hat{x}_0$ can be found. Substituting this value back into either of the original equations allows us to calculate the corresponding $\hat{y}_0$ of the intersection point.

Since the examined values $\mu_{q_c}^\gamma$, $c_{q_c}^\gamma$ are correlated based on the investigation in Chapter 4, and $\mu_{q_c+1}^\gamma$, $c_{q_c+1}^\gamma$ follow similar conditions, the variance of the extracted point in the x-coordinate can be calculated as

$$\text{var}(\hat{x}_0) = \left(\frac{\partial \hat{x}_0}{\partial \Delta c^\gamma}\right)^2 \text{var}(\Delta c^\gamma) + \left(\frac{\partial \hat{x}_0}{\partial \Delta \mu^\gamma}\right)^2 \text{var}(\Delta \mu^\gamma)$$
$$+ 2\left(\frac{\partial \hat{x}_0}{\partial \Delta c^\gamma}\right)\left(\frac{\partial \hat{x}_0}{\partial \Delta \mu^\gamma}\right)\text{Cov}(\Delta c^\gamma, \Delta \mu^\gamma),$$

(A.5)

By rearranging the equation above mathematically, the variance can be given as

$$\text{var}(\hat{x}_0) = \frac{\text{var}(\Delta c^\gamma) + \hat{x}_0^2 \text{var}(\Delta \mu^\gamma) + 2\hat{x}_0 \text{Cov}(\Delta c^\gamma, \Delta \mu^\gamma)}{\Delta(\mu^\gamma)^2},$$

(A.6)

where

$$\text{Cov}(\Delta c^\gamma, \Delta \mu^\gamma) = \overline{x}_{q_c}\text{var}(\mu_{q_c}^\gamma) - \overline{x}_{q_c+1}\text{var}(\mu_{q_c+1}^\gamma)$$
$$= -\left[\frac{\overline{x}_{q_c}}{S_{q_c,xx}} + \frac{\overline{x}_{q_c+1}}{S_{q_c+1,xx}}\right]s_p^2$$

(A.7)

with $\overline{x}_{q_c}$ is the mean value, $S_{q_c,xx}$ represents the sum of squares about the mean and

$$s_p^2 = \frac{(N_{q_c} - 2)s_{q_c}^2 + (N_{q_c+1} - 2)s_{q_c+1}^2}{N_{q_c+} + N_{q_c+1} - 4}$$

(A.8)

where N_{q_c} is the number of points per line [MDMA17], [SW02a].

In additon, the variance of $\hat{y}_0$ can be given based on (A.1) or (A.2) according to $t_{\alpha_t/2}$, where t is the student distribution and α_t represents the degree of freedom [MDMA17], [SW02a].

A.2   Hardware Specifications

The hardware components designed to operate in the E-Band range play a significant role by enabling advanced communication and sensing capabilities.

Through detailed analysis and information in this appendix, the specification and facilities of the employed hardware are given based on their data sheets from the manufacturers.

A.2.1   E-Band Subharmonically Quadrature Mixer

The system employs subharmonic mixers from based on the model (**SFT-71386315-122FSF-N1-M**). The mixers cover a frequency range of $(76 - 81)$ GHz and offer a typical conversion loss of $20\,\mathrm{dB}$ with an LO driving power of $16\,\mathrm{dBm}$. With a low LO frequency range of $(29 - 43)$ GHz, the mixers are well-suited for low-cost E-band system solutions. Additionally, the mixers have a typical LO to RF port isolation of $20\,\mathrm{dB}$ and can be used as a phase detector since their IF port is DC coupled. Table B.1 and B.2 represent more information on their electrical and mechanical specifications.

Fig. A.1: The subharmonic mixer employed in the measurement campaign.

145

Table A.1: Electrical Specifications of the subharmonic mixer

Parameter	Minimum	Typical	Maximum
RF Frequency Range	71 GHz		86 GHz
LO Frequency Range	29 GHz		43 GHz
LO Pumping Power		+16 dBm	+20 dBm
IF Frequency Range	DC		12 GHz
Conversion Loss		20 dB	
LO to IF Isolation		20 dB	
LO to RF Port Isolation	20 dB	30 dB	
Combined RF			+20 dBm
Specification Temperature		+25 °C	
Operating Temperature	+0 °C		+25 °C

Table A.2: Mechanical Specifications of the subharmonic mixer

Item	Specification
RF Port	WR-12 Waveguide with UG-387/U Flange
LO Port	2.4 mm
IF-I, IF-Q Ports	SMA(F), SMA(F)
Case Material	Aluminum
Finish	Gold Plated
Weight	1.8 Oz
Size	[1.25, 1.25, 0.88]
Outline	FT-NEM

A.2.2 21-56 GHz Active 4F Multiplier

The frequency multiplier is adopted through the work to quadruple the input frequency within the range of $(5.25 - 14)$ GHz, generating a frequency in the range of $(21 - 56)$ GHz. The multiplier is marked as (**AQA-2156**) and provides 20 dBm with 0 dBm input power. The multiplier also offers superior harmonic suppressions and can produce enough LO drive for Marki S-, H-, and L- diode mixers. To ensure the best performance, a heat sink has been connected with the multiplier to limit the increased temperature during its operation, as shown in Fig. B.2. Additionally, the general and electrical specifications of the multiplier are listed in Table B.3 and B.4.
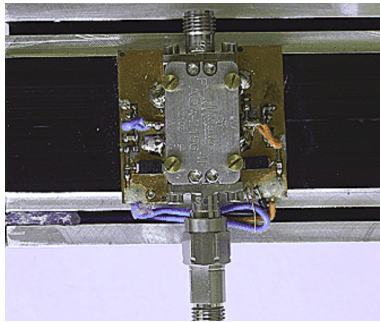
Fig. A.2: The frequency multiplier employed in the measurement campaign.

Table A.3: General Specifications of the frequency multiplier

Parameter	Maximum Rating
Positive Bias Voltage	4 V
Positive Bias Current	600 mA
Negative Bias Voltage	−10 V
Negative Bias Current	3 mA
RF Input Power	+5 dBm
ESD (Human Body Model)	Class 1A
Operating Temperature	$(-40 - 50)\,°C$
Storage Temperature RF	$(-65 - 150)\,°C$

Table A.4: Electrical Specifications of the frequency multiplier

Parameter	Test Conditions	Min	Typical	Max
Input Frequency Range		5.25 GHz		14 GHz
Output Frequency Range		21 GHz		56 GHz
Input Power		-	+2 dBm	+4 dBm
4F Output Power	$(21 - 25)\,GHz$		20 dBm	
	$(25 - 48)\,GHz$	17 dBm	21 dBm	
	$(48 - 56)\,GHz$		18 dBm	
Suppression	(1F) $(5.25 - 14)\,GHz$		44 dBc	
	(2F) $(10.5 - 28)\,GHz$		35 dBc	
	(3F) $(15.75 - 42)\,GHz$		24 dBc	
	(5F) $(26.25 - 67)\,GHz$		32 dBc	
Bias Requirements	Power Supply: +3.5 V		250 mA	
	Bias: −5 V		10 mA	

A.2.3 E-Band Broadband Power Amplifier

The power amplifier applied to the investigation is based on the model **AT-PA-7186-2017** with 17 dBm output power in the frequency of (71 − 86) GHz. The module is with a standard WR-12 waveguide. The power amplifier has high gain, high linearity, low input/output return loss, and flat gain response. It can also be used from (68 − 89) GHz with some variation of performance.

Fig. A.3: The frequency multiplier employed in the measurement campaign.

Table A.5: Electrical specifications of the PA

Parameter	Minimum	Typical	Maximum
Frequency	68 GHz	$(71 - 86)$ GHz	89 GHz
Gain		20 dB	
Drain Supply		+5 V	+8 V
Current Id		400 mA	
P1dB		15 dBm	
Psat		17 dBm	
Input Return Loss		−7 dB	
Output Return Loss		−7 dB	
Spec Temp		25 °C	

Table A.6: Mechanical specifications of the PA

Item	Specification
Input Port	WR-12
Output Port	WR-12
Case Material	Copper
Finish	Gold Plated
Weight (Without Heatsink)	221 g

A.2.4 E-Band Low Noise Amplifier

This work employs an efficient low-noise amplifier (LNA) based on the model (**SBL-5539532560-1212-E1**). The LNA operates in a wide frequency range of $(55 - 95)$ GHz and provides a nominal noise figure of only 6 dB, while delivering a signal gain of 25 dB. The LNA has a convenient inline structure compatible with WR-12 waveguides and UG-387/U anti-cocking flanges. Additionally, other ports are available for configuration under various model

numbers, including a right-angle construction with WR-12 waveguides or 1 mm connections.

Fig. A.4: Low-noise amplifier

Table A.7: Electrical specifications of the LNA

Parameter	Minimum	Typical	Maximum
Frequency	55 GHz		95 GHz
Gain		25 dB	
Noise figure		6 dB	
DC Voltage	+6 V	+8 V	+15 V
DC Current		300 mA	
P1dB		12 dBm	
Psat		16 dBm	
Input Return Loss		10 dB	
Output Return Loss		10 dB	
Spec Temp		25 °C	

Table A.8: Mechanical specifications of the LNA

Item	Specification
Input Port	WR-12
Output Port	WR-12
Case Material	Aluminum
Finish	Gold Plated
Weight	45 g

Bibliography

[3GP20]   3GPP. Service requirements for enhanced V2X scenarios (3GPP TS 22.186 version 15.3.0 Release 15), 2020.

[3GP22]   3GPP. 5G; Study on channel model for frequencies from 0.5 to 100 GHz. Technical Specification (TS) 38.901, 3rd Generation Partnership Project (3GPP), 04 2022. Version 17.0.0.

[A+13]   A. Anghel et al. FMCW transceiver wideband sweep nonlinearity software correction. In *2013 IEEE Rad. Conf. (RadarCon13)*, pages 1–5, 2013.

[A+21]   C. Aydogdu et al. RadChat: Spectrum Sharing for Automotive Radar Interference Mitigation. *IEEE Trans. on Intell. Transp. Syst.*, 22(1):416–429, 2021.

[A+22a]   M. B. Alabd et al. Modified Pulse Position Modulation for Joint Radar Communication Based on Chirp Sequence. *IEEE Microw. and Wireless Compon. Lett.*, 32(10):1247–1250, 2022.

[A+22b]   M. B. Alabd et al. Preamble-Based Synchronization for Communication-Assisted Chirp Sequence Radar. *Progress in Electromagn. Research (PIER C)*, 127(10):31–48, 2022.

[ADM+23]   M. B. Alabd, J. Dittmer, J. P. Messmer, B. Nuss, Y. Li, J. Galinsky, and T. Zwick. A simulator for cacs-based radar systems in multi-user automotive scenarios. In *2023 20th European Radar Conference (EuRAD)*, pages 152–155, 2023.

[ADN+23]   M. B. Alabd, J. Dittmer, Y. Nuss, B. Li, L. Giroto de Oliveira, A. Diewald, and T. Zwick. Time-frequency synchronization for cacs-based radar systems in interference scenarios. In *2023 20th European Radar Conference (EuRAD)*, pages 464–467, 2023.

[AdOGN+20]   M. B. Alabd, L. de Oliveira Giroto, B. Nuss, W. Wiesbeck, and T. Zwick. Time-Frequency Shift Modulation for Chirp Sequence based Radar Communications. In *Proc. IEEE MTT-S Int. Conf. on Microw. for Intell. Mobility (ICMIM)*, pages 1–4, 2020.

[AGdON$^+$24] M. B. Alabd, L. Giroto de Oliveira, B. Nuss, Y. Li, A. Diewald, J. Galinsky, Z. Kollár, and T. Zwick. Analysis of Channel Impact on Partial Communication based on Chirp Sequence Radar. *IEEE Microw. and Wireless Lett.*, accepted in (2024).

[ANWZ19] M. B. Alabd, B. Nuss, C. Winkler, and T. Zwick. Partial Chirp Modulation Technique for Chirp Sequence based Radar Communications. In *Proc. Eur. Radar Conf. (EURAD)*, pages 173–176, 2019.

[AWE14] AWE Communications GmbH. Winprop version 13, 2014.

[Ayh16] Serdal Ayhan. *Hochgenaue radarbasierte Abstandsmessung mit geführter Wellenausbreitung*. KIT Scientific Publishing, Karlsruhe, Feb 2016.

[Bag05] J. A. Baglivo. *Mathematica Laboratories for Mathematical Statistics*. Society for Industrial and Applied Mathematics, 2005.

[BBW17] J. Bechter, Kushan Deb Biswas, and Christian Waldschmidt. Estimation and cancellation of interferences in automotive radar signals. In *2017 18th Int. Rad. Symp. (IRS)*, pages 1–10, 2017.

[BEJ07] P. Barrenechea, F. Elferink, and J. Janssen. FMCW radar with broadband communication capability. In *2007 Eur. Rad. Conf. (EuRAD)*, pages 130–133, 2007.

[Bin92] P. Binns. FMCW radar: a low cost sensor for automotive applications. In *IEE Colloquium on Automotive Sensors*, pages 6/1–6/6, 1992.

[BJEPC14] F. Burkhardt, S. Jaeckel, E. Eberlein, and R. Prieto-Cerdeira. QuaDRiGa: A MIMO channel model for land mobile satellite. In *The 8th Eur. Conf. on Antennas and Propag. (EuCAP 2014)*, pages 1274–1278, 2014.

[BJT21] O. Bialer, A. Jonas, and T. Tirer. Code Optimization for Fast Chirp FMCW Automotive MIMO Radar. *IEEE Trans. on Veh. Technol.*, 70(8):7582–7593, 2021.

[BKYA13] G. Babur, O. A. Krasnov, A. Yarovoy, and P. Aubry. Nearly Orthogonal Waveforms for MIMO FMCW Radar. *IEEE Trans. Aerosp. Electron. Syst.*, 49(3):1426–1437, 2013.

[BMKCF20] A. Belen Martinez, A. Kumar, M. Chafii, and G. Fettweis. A Chirp-Based Frequency Synchronization Approach for Flat Fa-

ding Channels. In *2020 2nd 6G Wireless Summit (6G SUMMIT)*, pages 1–5, 2020.

[Bor22] F. Borngräber. Gesamtbewertung und Empfehlung für Standardisierung, 2022.

[Bra14] K. Braun. *OFDM Radar Algorithms in Mobile Communication Networks*. PhD thesis, Karlsruher Institut für Technologie (KIT), 2014.

[Bro07] Graham M. Brooker. Mutual Interference of Millimeter-Wave Radar Systems. *IEEE Trans. Electromagn. Compat.*, 49(1):170–181, 2007.

[BRRW17] J. Bechter, F. Roos, M. Rahman, and C. Waldschmidt. Automotive radar interference mitigation using a sparse sampling approach. In *Proc. Eur. Radar Conf. (EURAD)*, pages 90–93, 2017.

[BRW17] J. Bechter, F. Roos, and C. Waldschmidt. Compensation of Motion-Induced Phase Errors in TDM MIMO Radars. *IEEE Microw. and Wireless Compon. Lett.*, 27(12):1164–1166, 2017.

[BW$^+$18] W. Buller, B. Wilson, et al. Radar congestion study, 2018.

[CEPB02] S. Coleri, M. Ergen, A. Puri, and A. Bahai. Channel estimation techniques based on pilot arrangement in OFDM systems. *IEEE Trans. on Broadcast.*, 48(3):223–229, 2002.

[CF20] S. Coicheci and I. Filip. Self-driving vehicles: current status of development and technical challenges to overcome. In *2020 IEEE 14th Int. Symp. on pl. Comput. Intell. and Informat. (SACI)*, pages 000255–000260, 2020.

[Chi23] U. Chipengo. High Fidelity Physics-Based Simulation of a 512-Channel 4D-Radar Sensor for Automotive Applications. *IEEE Access*, 11:15242–15251, 2023.

[CL20] Dmytro Cherniak and Salvatore Levantino. *Chirp Generators for Millimeter-Wave FMCW Radars*, pages 33–47. Springer International Publishing, Cham, 2020.

[Cri57] David S. Crippen. The Air Traffic Control Radar Beacon System. *IRE Trans. Aeronaut. Navig. Electron.*, ANE-4(1):6–15, 1957.

[CS92] A. Colquhoun and L.P. Schmidt. MMICs for automotive and traffic applications. In *GaAs IC Symp. Tech. Dig. 1992*, pages 3–6, 1992.

[D⁺21]   J. Ding et al. Automotive radar 4D Point-cloud Imaging with
           2D Sparse Array. In *2021 CIE Int. Conf. on Rad. (Radar)*, pages
           2838–2842, 2021.

[DAN⁺21a] A. Diewald, T. Antes, B. Nuss, M. Pauli, and T. Zwick. Range
           Doppler Migration Synthesis for Realistic Radar Target Simu-
           lation. In *2021 IEEE Topical Conf. on Wireless Sensors and
           Sensor Netw. (WiSNeT)*, pages 56–58, 2021.

[DAN21b]   A. Diewald, T. Antes, and T. Nuss, B.and Zwick. Implemen-
           tation of Range Doppler Migration Synthesis for Radar Tar-
           get Simulation. In *2021 IEEE 93rd Veh. Technol. Conference
           (VTC2021-Spring)*, pages 1–5, 2021.

[DBSF19]   S. Dwivedi, A. N. Barreto, P. Sen, and G. Fettweis. Target Detec-
           tion in Joint Frequency Modulated Continuous Wave (FMCW)
           Radar-Communication System. In *Proc. 16th Int. Symp. on Wi-
           reless Commun. Syst. (ISWCS)*, pages 277–282, 2019.

[Dit20]   J. Dittmer. *Untersuchung des Interferenzeinflusses auf FMCW
           RadCom*. KIT, Karlsruhe, April 2020.

[DK90]   P.M. Djuric and S.M. Kay. Parameter estimation of chirp si-
           gnals. *IEEE Trans. on Acoust., Speech, and Signal Process.*,
           38(12):2118–2126, 1990.

[DL⁺21]   C. De Lima et al. Convergent Communication, Sensing and
           Localization in 6G Systems: An Overview of Technologies, Op-
           portunities and Challenges. *IEEE Access*, 9:26902–26925, 2021.

[DNPZ22]   A. Diewald, B. Nuss, M. Pauli, and T. Zwick. Arbitrary Angle
           of Arrival in Radar Target Simulation. *IEEE Trans. Microw.
           Theory Tech.*, 70(1):513–520, 2022.

[DPBS17]   I. Djurović, V. Popović-Bugarin, and M. Simeunović. The STFT-
           Based Estimator of Micro-Doppler Parameters. *IEEE Trans. on
           Aerosp. and Electron. Syst.*, 53(3):1273–1283, 2017.

[DZB⁺20]   S. Dwivedi, M. Zoli, A. N. Barreto, P. Sen, and G. Fettweis.
           Secure Joint Communications and Sensing using Chirp Modu-
           lation. In *2nd 6G Wireless Summit (6G SUMMIT)*, pages 1–5,
           2020.

[E⁺16]   F. Enggar et al. Performance comparison of various windowing
           On FMCW radar signal processing. In *2016 Int. Symp. on
           Electron. and Smart Devices (ISESD)*, pages 326–330, 2016.

[EKSX96]   M. Ester, H. Kriegel, J. Sander, and X. Xu. A Density-Based Algorithm for Discovering Clusters in Large Spatial Databases with Noise. In *Proc. of the 2nd Int. Conf. on Knowledge Discovery and Data Mining*, KDD'96, page 226–231. AAAI Press, 1996.

[El 95]   Mohamed B. El Mashade. Performance analysis of modified ordered-statistics CFAR processors in nonhomogeneous environments. *Signal Process.*, 41(3):379–389, 1995.

[ES01]   E. Elsehely and M.I. Sobhy. Reduction of interference in automotive radars using multiscale wavelet transform. In *2001 IEEE Int. Conf. on Acoust., Speech, and Signal Process.. Proc. (Cat. No.01CH37221)*, volume 5, pages 2881–2884 vol.5, 2001.

[ETS12]   ETSI. Intelligent Transport Systems (ITS);Performance Evaluation of Self-Organizing TDMA as Medium Access Control Method Applied to ITS; Access Layer Part, 2011-2012.

[FA18]   V. Fialho and F. Azevedo. Wireless Communication Based on Chirp Signals for LoRa IoT Devices. *i-ETC : ISEL Academic J. of Electron. Telecommun. and Comput.*, 4(1), 2018.

[FB08]   Keith W. Forsythe and Daniel W. Bliss. *MIMO Radar: Concepts, Performance Enhancements, and Applications*, chapter 2, pages 65–121. John Wiley, 2008.

[FBDM15]   C. Fischer, H. L. Blöcher, J. Dickmann, and W. Menzel. Robust detection and mitigation of mutual interference in automotive radar. In *2015 16th Int. R. Symp. (IRS)*, pages 143–148, 2015.

[FGM+21]   Martin Fuchs, Hansjerg Goelz, Jonathan Moss, Andreas Lefevre, and Michael Kritzner. A RADAR SYSTEM WITH SUB-BANDS, Aug 2021.

[FJ15a]   J. Fink and F. K. Jondral. A Numerical Comparison of Chirp Sequence versus OFDM Radar Waveforms. In *2015 IEEE 82nd Veh. Technol. Conf. (VTC2015-Fall)*, pages 1–2, 2015.

[FJ15b]   J. Fink and F. K. Jondral. Comparison of OFDM radar and chirp sequence radar. In *2015 16th Int. Rad. Symp. (IRS)*, pages 315–320, 2015.

[FJE21]   A. Figueroa, N. Joram, and F. Ellinger. Automatic delay and phase mismatch calibration in FMCW MIMO radar. In *2020 17th Eur. Rad. Conf. (EuRAD)*, pages 402–405, 2021.

[FME18]   B. Farley, J. McGrath, and C. Erdmann. An All-Programmable 16-nm RFSoC for Digital-RF Communications. *IEEE Micro*, 38(2):61–71, 2018.

[G+17]   D. Guermandi et al. A 79-GHz 2×2 MIMO PMCW Radar SoC in 28-nm CMOS. *IEEE Journal of Solid-State Circuits*, 52(10):2613–2626, 2017.

[Gar16]   M. Garrido. The Feedforward Short-Time Fourier Transform. *IEEE Trans. Circuits Syst. II, Exp. Briefs*, 63(9):868–872, 2016.

[GdO+21]   L. Giroto de Oliveira et al. Joint radar-communication systems: Modulation schemes and system design. *IEEE Trans. Microw. Theory Tech.*, pages 1–1, 2021.

[GdOAN+22]   L. Giroto de Oliveira, T. Antes, B. Nuss, E. Bekker, A. Bhutani, A. Diewald, M. B. Alabd, Y. Li, M. Pauli, and T. Zwick. Doppler Shift Tolerance of Typical Pseudorandom Binary Sequences in PMCW Radar. *Sensors*, 22(9), 2022.

[GdOANZ20]   L. Giroto de Oliveira, M. B. Alabd, B. Nuss, and T. Zwick. An OCDM Radar-Communication System. In *2020 14th Eur. Conf. Antennas Propag.*, pages 1–5, 2020.

[GJSW23]   T. Grebner, V. Janoudi, P. Schoeder, and C. Waldschmidt. Self-Calibration of a Network of Radar Sensors for Autonomous Robots. *IEEE Trans. on Aerosp. and Electron. Syst.*, pages 1–12, 2023.

[GKCC20]   L. Gaudio, M. Kobayashi, G. Caire, and G. Colavolpe. On the Effectiveness of OTFS for Joint Radar Parameter Estimation and Communication. *IEEE Trans. on Wireless Commun.*, 19(9):5951–5965, 2020.

[GNA+21]   L. Giroto de Oliveira, B. Nuss, M. B. Alabd, Y. Li, L. Yu, and T. Zwick. MIMO-OCDM-Based Joint Radar Sensing and Communication. In *2021 15th Eur. Conf. Antennas Propag.*, pages 1–5, 2021.

[HFS22]   J. Hasch, M. Fink, and T. Schmid. 77 GHz 4x4 TDM MIMO Radar with an Extended Unambiguous Velocity Range. In *2022 19th Eur. Rad. Conf. (EuRAD)*, pages 1–4, 2022.

[HL20]   R. Hu and P. Li. Calibration and Positioning of nonlinear wideband FMCW radar. In *2020 IEEE MTT-S Int. Wireless Symp. (IWS)*, pages 1–3, 2020.

[HSZ18]   K. Hahmann, S. Schneider, and T. Zwick. Evaluation of probability of interference-related ghost targets in automotive radars. In *2018 IEEE MTT-S Int. Conf. on Microw. for Int. Mobility (ICMIM)*, pages 1–4, 2018.

[HT20]   S. Häfner and R. Thomä. Compensation of Motion-Induced Phase Errors and Enhancement of Doppler Unambiguity in TDM–MIMO Systems by Model-Based Estimation. *IEEE Sensors Lett.*, 4(10):1–4, 2020.

[HW98]   M. H. Hsieh and C. H. Wei. Channel estimation for OFDM systems based on comb-type pilot arrangement in frequency selective fading channels. *IEEE Trans. on Consum. Electron.*, 44(1):217–225, 1998.

[HY19]   G. Hakobyan and B. Yang. High-Performance Automotive Radar: A Review of Signal Processing Algorithms and Modulation Schemes. *IEEE Signal Process. Mag.*, 36(5):32–44, 2019.

[Hü04]   C. Hülsmeyer. Verfahren, um metallische Gegenstände mittels elektrischer Wellen einem Beobachter zu melden, DE Patent 165546, April 30, 1904.

[Hü20]   T. Hülder. *Aufbau eines Front-Ends für FMCW RadCom*. KIT, Karlsruhe, April 2020.

[IAMH96]   M.Z. Ikram, K. Abed-Meraim, and Y. Hua. Fast discrete quadratic phase transform for estimating the parameters of chirp signals. In *Conf. Record of The 13th Asilomar Conf. on Signals, Syst. and Comput.*, volume 1, pages 798–802 vol.1, 1996.

[IEE08]   IEEE. 2007 Index IEEE Vehicular Technology Magazine Vol. 2. *IEEE Veh. Technol. Mag.*, 3(1):43–48, 2008.

[IEE10]   IEEE. IEEE Standard for Information technology– Local and metropolitan area networks– Specific requirements– Part 11: Wireless LAN Medium Access Control (MAC) and Physical Layer (PHY) Specifications Amendment 6: Wireless Access in Vehicular Environments. *IEEE Std 802.11p-2010 (Amendment to IEEE Std 802.11-2007)*, pages 1–51, 2010.

[IT17]   ITU-T. Guidelines for evaluation of radio interface technologies for IMT-2020. Recommendation M.2412, International Telecommunication Union, Geneva, 2017.

[J⁺22]   F. Javanshour et al. Performance Evaluation of Station-Based Autonomous On-Demand Car-Sharing Systems. *IEEE Trans. on Intell. Transp. Syst.*, 23(7):7721–7732, 2022.

[K⁺11]   G. Karagiannis et al. Vehicular Networking: A Survey and Tutorial on Requirements, Architectures, Challenges, Standards and Solutions. *IEEE Commun. Surv. Tutor.*, 13(4):584–616, 2011.

[K⁺21a]   S. Kumar et al. Interference Mitigation Methods for Coexistence of Radar and Communication. In *2021 15th Eur. Conf. on Antennas and Propag.(EuCAP)*, pages 1–4, 2021.

[K⁺21b]   U. Kumbul et al. Experimental Investigation of Phase Coded FMCW for Sensing and Communications. In *2021 15th Eur. Conf. on Antennas and Propag.(EuCAP)*, pages 1–5, 2021.

[KG14]   Ma. Krawczyk and T. Gerkmann. STFT Phase Reconstruction in Voiced Speech for an Improved Single-Channel Speech Enhancement. *IEEE/ACM Trans. on Audio, Speech, and Language Process.*, 22(12):1931–1940, 2014.

[KKI08]   D. Kim, U. K. Kwon, and G. H. Im. Pilot Position Selection and Detection for Channel Estimation of SC-FDE. *IEEE Commun. Lett.*, 12(5):350–352, 2008.

[KP18]   A. Knapp and L. Pap. A novel mobile communication system using Pulse Position based Chirp Spread Spectrum modulation. *J. Commun. Softw. Syst.*, 14(3):228–238, 9 2018.

[KR14]   M. Kronauge and H. Rohling. New chirp sequence radar waveform. *IEEE Trans. Aerosp. Electron. Syst.*, 50(4):2870–2877, 2014.

[KRM⁺16]   J. Khoury, R. Ramanathan, D. McCloskey, R. Smith, and T. Campbell. RadarMAC: Mitigating Radar Interference in Self-Driving Cars. In *2016 13th Annual IEEE Int. Conf. on Sens., Commun., and Netw. (SECON)*, pages 1–9, 2016.

[Kun12]   Kunert, M. Project Final Report MOSARIM: More Safety for all by Radar Interference Mitigation, 2012.

[L⁺17]   Y. Liu et al. Adaptive OFDM Integrated Radar and Communications Waveform Design Based on Information Theory. *IEEE Commun. Lett.*, 21(10):2174–2177, 2017.

[L⁺18]   F. Liu et al. Toward Dual-functional Radar-Communication Systems: Optimal Waveform Design. *IEEE Trans. on Signal Process.*, 66(16):4264–4279, 2018.

[L⁺20]   F. Lampel et al. System Level Synchronization of Phase-Coded FMCW Automotive Radars for RadCom. In *2020 14th Eur. Conf. Antennas Propag.*, pages 1–5, 2020.

[LLK18] S. Lim, S. Lee, and S. C. Kim. Clustering of Detected Targets Using DBSCAN in Automotive Radar Systems. In *2018 19th Int. Rad. Symp. (IRS)*, pages 1–7, 2018.

[LMI16] G. Lellouch, A. K. Mishra, and M. Inggs. Design of OFDM radar pulses using genetic algorithm based techniques. *IEEE Trans. on Aerosp. and Electron. Syst.*, 52(4):1953–1966, 2016.

[LP03a] Y. P. Lin and S. M. Phoong. BER minimized OFDM systems with channel independent precoders. *IEEE Trans. on Signal Process.*, 51(9):2369–2380, 2003.

[LP03b] Y. P. Lin and S. M. Phoong. MMSE OFDM and prefixed single carrier systems: BER analysis. In *2003 IEEE Int. Conf. on Acoust., Speech, and Signal Process., 2003. Proc. (ICASSP '03).*, volume 4, pages IV–229, 2003.

[LTAW19] F. Lampel, R. F. Tigrek, A. Alvarado, and F. M.J. Willems. A Performance Enhancement Technique for a Joint FMCW Rad-Com System. In *2019 16th Eur. Rad. Conf. (EuRAD)*, pages 169–172, 2019.

[LWYF21] X. Li, X. Wang, Q. Yang, and S. Fu. Signal Processing for TDM MIMO FMCW Millimeter-Wave Radar Sensors. *IEEE Access*, 9:167959–167971, 2021.

[M⁺20]   D. Ma et al. Joint Radar-Communication Strategies for Autonomous Vehicles: Combining Two Key Automotive Technologies. *IEEE Signal Processing Magazine*, 37(4):85–97, 2020.

[MBM17] P. M. McCormick, S. D. Blunt, and J. G. Metcalf. Simultaneous radar and communications emissions from a common aperture, Part I: Theory. In *2017 IEEE Rad. Conf. (RadarConf)*, pages 1685–1690, 2017.

[MDMA17] J. Martin, G. Delgado Martin, and A. G. Asuero. Intersecting Straight Lines: Titrimetric Applications. In Vu Dang Hoang,

editor, *Adva. in Titration Techn.*, chapter 3. IntechOpen, Rijeka, 2017.

[Mer64]   A.L. Merlo. Automotive Radar for the Prevention of Collisions. *IEEE Trans. on Ind. Electron. and Control Instrum.*, IECI-11(1):1–6, 1964.

[Mes20]   J. P. Messmer. *Statistische Untersuchung von Interferenzeffekten auf die Datenübertragung zwischen FMCW-RadCom Systemen*. KIT, Karlsruhe, April 2020.

[MMMK12]   C. Maag, D. Muhlbacher, C. Mark, and H. P. Kruger. Studying Effects of Advanced Driver Assistance Systems (ADAS) on Individual and Group Level Using Multi-Driver Simulation. *IEEE Intell. Transp. Syst. Mag.*, 4(3):45–54, 2012.

[MS07]   M. Marey and H. Steendam. Analysis of the Narrowband Interference Effect on OFDM Timing Synchronization. *IEEE Trans. on Signal Process.*, 55(9):4558–4566, 2007.

[MX16]   K. Manolakis and W. Xu. Time Synchronization for Multi-Link D2D/V2X Communication. In *proc IEEE 89th Veh. Technol. Conf. (VTC-Fall)*, pages 1–6, 2016.

[Mü15]   M. Müller. *Fundamentals of Music Process.* Springer International Publishing, 2015.

[N+16]   M. Nowak et al. Co-designed radar-communication using linear frequency modulation waveform. In *MILCOM 2016 - 2016 IEEE Military Commun. Conf.*, pages 918–923, 2016.

[N+20]   M. Q. Nguyen et al. A Fast-Chirp MIMO Radar System Using Beat Frequency FDMA With Single-Sideband Modulation. In *2020 IEEE/MTT-S Int. Microw. Symp. (IMS)*, pages 1015–1018, 2020.

[N+21]   F. Norouzian et al. Phenomenology of automotive radar interference. *IET Rad., Sonar & Navig.*, 15(9):1045–1060, 2021.

[NHK19]   H. J. Ng, R. Hasan, and D. Kissinger. A Scalable Four-Channel Frequency-Division Multiplexing MIMO Radar Utilizing Single-Sideband Delta–Sigma Modulation. *IEEE Trans. Microw. Theory Tech.*, 67(11):4578–4590, 2019.

[NKY17]   S. Neemat, O. A. Krasnov, and A. Yarovoy. Simultaneous processing of time-shifted orthogonal LFMCW waveforms. In *2017 Signal Process. Symp. (SPSympo)*, pages 1–4, 2017.

[NUKY19]   S. Neemat, F. Uysal, O. Krasnov, and A. Yarovoy. Reconfigurable Range-Doppler Processing and Range Resolution Improvement for FMCW Radar. *IEEE Sensors J.*, 19(20):9294–9303, 2019.

[OM21]   M. S. Omar and X. Ma. Performance Analysis of OCDM for Wireless Communications. *IEEE Trans. on Wireless Commun.*, 20(7):4032–4043, 2021.

[OZ16]   X. Ouyang and J. Zhao. Orthogonal Chirp Division Multiplexing. *IEEE Trans. on Commun.*, 64(9):3946–3957, 2016.

[PBF20]   T. M. Pham, A. N. Barreto, and G. P. Fettweis. Efficient Communications for Overlapped Chirp-Based Systems. *IEEE Wireless Commun.s Lett.*, 9(12):2202–2206, 2020.

[PFWS13]   C. Pfeffer, R. Feger, C. Wagner, and A. Stelzer. FMCW MIMO Radar System for Frequency-Division Multiple TX-Beamforming. *IEEE Trans. Microw. Theory Tech.*, 61(12):4262–4274, 2013.

[PS07]   J. Proakis and M. Salehi. *Digital Communications 5th Edition*. McGraw Hill, 2007.

[PTV14]   PTV Planung Transport Verkehr AG. VISSIM, Software zur mikroskopischen Simulation des Verkehrsflusses, 2014.

[RBK$^+$19]   F. Roos, J. Bechter, C. Knill, B. Schweizer, and C. Waldschmidt. Radar Sensors for Autonomous Driving: Modulation Schemes and Interference Mitigation. *IEEE Microw. Mag.*, 20(9):58–72, 2019.

[Rid46]   Louis N. Ridenour. Radar in war and peace. *Electr. Eng.*, 65(5):202–207, 1946.

[RK14]   H. Rohling and M. Kronauge. New radar waveform based on a chirp sequence. In *2014 Int. Rad. Conf.*, pages 1–4, 2014.

[RL95]   H. Rohling and E. Lissel. 77 GHz radar sensor for car application. In *Proc. Int. Rad. Conf.*, pages 373–379, 1995.

[Rob23]   Rob Decae (SWOV). European Road Safety Observatory Annual statistical report on road safety in the EU 2022, 2023.

[Roo20]   F. Roos. *Optimierte Signalverarbeitung für Chirp-Sequence-modulierte Kfz-Radarsensoren*. Universität Ulm, Ulm, June 2020.

[S⁺91]   A.J. Sephton et al. Segmentation of Land and Sea-Ice Synthetic-Aperture Radar Imagery. In *[Proceedings] IGARSS'91 Remote Sensing: Global Monitoring for Earth Management*, volume 3, pages 1809–1812, 1991.

[S⁺15]   T. Schipper et al. Simulative Prediction of the Interference Potential Between Radars in Common Road Scenarios. *IEEE Trans. on Electromagn. Compat.*, 57(3):322–328, 2015.

[S⁺17]   C. Sahin et al. A novel approach for embedding communication symbols into physical radar waveforms. In *2017 IEEE Rad. Conf. (RadarConf)*, pages 1498–1503, 2017.

[S⁺18]   Y. L. Sit et al. BPSK-based MIMO FMCW Automotive-Radar Concept for 3D Position Measurement. In *2018 15th Eur. Rad. Conf. (EuRAD)*, pages 289–292, 2018.

[S⁺21]   X. Shi et al. BER Performance Analysis of Non-Coherent Q-Ary Pulse Position Modulation Receivers on AWGN Channel. In *Sensors*, 2021.

[S⁺23]   N. Sichani et al. Waveform Selection for FMCW and PMCW 4D-Imaging Automotive Radar Sensors. In *2023 IEEE Rad. Conf. (RadarConf23)*, pages 1–6, 2023.

[SA05]   M. K. Simon and M. S. Alouini. *Digital Communication over Fading Channels; 2nd ed.* Wiley, Newark, NJ, 2005.

[SC97]   T.M. Schmidl and D.C. Cox. Robust frequency and timing synchronization for OFDM. *IEEE Trans. Commun.*, 45(12):1613–1621, 1997.

[Sch17] Tom Schipper. *Modellbasierte Analyse des Interferenzverhaltens von Kfz-Radaren*. KIT Scientific Publishing, Karlsruhe, Jun 2017.

[SFHS15] W. Scheiblhofer, R. Feger, A. Haderer, and A. Stelzer. Method to embed a data-link on FMCW chirps for communication between cooperative 77-GHz radar stations. In *2015 Eur. Rad. Conf. (EuRAD)*, pages 181–184, 2015.

[SSZ⁺11] Y. L. Sit, C. Sturm, T. Zwick, L. Reichardt, and W. Wiesbeck. The OFDM Joint Radar-Communication System: An Overview. In *The 3rd Int. Conf. on Adv. in Satellite and Sp. Commun., SPACOMM 2011, April 17-22, 2011 - Budapest, Hungary*, pages 69–74, 2011.

[SW02a]   G. Speyer and M. Werman. Parameter Estimates for a Pencil of Lines: Bounds and Estimators. In A. Heyden, G. Sparr, M. Nielsen, and P. Johansen, editors, *Computer Vision — ECCV 2002*, pages 432–446, Berlin, Heidelberg, 2002. Springer Berlin Heidelberg.

[SW02b]   Gavriel Speyer and Michael Werman. Parameter Estimates for a Pencil of Lines: Bounds and Estimators. In Anders Heyden, Gunnar Sparr, Mads Nielsen, and Peter Johansen, editors, *Computer Vision — ECCV 2002*, pages 432–446, Berlin, Heidelberg, 2002. Springer Berlin Heidelberg.

[SW11]   C. Sturm and W. Wiesbeck. Waveform Design and Signal Processing Aspects for Fusion of Wireless Communications and Radar Sensing. *Proc. of the IEEE*, 99(7):1236–1259, 2011.

[SZ21]   S. Sun and Yimin D. Zhang. 4D Automotive Radar Sensing for Autonomous Vehicles: A Sparsity-Oriented Approach. *IEEE J. of Sel. Topics in Signal Process.*, 15(4):879–891, 2021.

[Ter64]   D.G. Terrington. Development of secondary surveillance radar for air-traffic control. *Electron. and Power*, 10(12):428–431, 1964.

[TI17]   TI. *LMX2491 6.4-GHz Low Noise RF PLL With Ramp/ChirpGeneration*, 2017.

[TI20]   TI. *AWR2243 Single-Chip 76- to 81-GHz FMCW Transceiver*, 2020.

[TMMW20]   M. Toth, P. Meissner, A. Melzer, and K. Witrisal. Slow-Time Mitigation of Mutual Interference in Chirp Sequence Radar. In *2020 IEEE MTT-S Int. Conf. on Microw. for Intell. Mobility (ICMIM)*, pages 1–4, 2020.

[TTRW20]   L. L. Tovar Torres, F. Roos, and C. Waldschmidt. Simulator Design for Interference Analysis in Complex Automotive Multi-User Traffic Scenarios. In *2020 IEEE Rad. Conf. (RadarConf20)*, pages 1–6, 2020.

[UMW⁺22]   M. Umehira, T. Maruyama, Y. Watanabe, X. Wang, and S. Takeda. Narrowband Interference Suppression using Envelop Detection-based Interference Replica Regeneration for Automotive CS Radars. In *2022 23rd Int. Rad. Symp. (IRS)*, pages 48–53, 2022.

[V⁺20]   C. Vasanelli et al. Calibration and Direction-of-Arrival Estima-
           tion of Millimeter-Wave Radars: A Practical Introduction. *IEEE
           Antennas and Propag. Mag.*, 62(6):34–45, 2020.

[VPSE02]   T. G. Vishwanath, M. Parr, Z. L. Shi, and S. Erlich. Synchro-
           nization in mobile satellite systems using dual-chirp waveform,
           U.S. Patent 6,418,158 B1, Jul 9, 2002.

[VTGG⁺14] W. Van Thillo, V. Giannini, D. Guermandi, S. Brebels, and
           A. Bourdoux. Impact of ADC clipping and quantization on
           phase-modulated 79 GHz CMOS radar. In *2014 11th Eur. Rad.
           Conf.*, pages 285–288, 2014.

[Wax08]   H. Wax. Autonomous vehicle development: No accident. *IEEE
           Women in Eng. Mag.*, 2(1):34–37, 2008.

[WBV21]   T. Wild, V. Braun, and H. Viswanathan. Joint Design of Com-
           munication and Sensing for Beyond 5G and 6G Systems. *IEEE
           Access*, 9:30845–30857, 2021.

[Wei82]   M. Weiss. Analysis of Some Modified Cell-Averaging CFAR
           Processors in Multiple-Target Situations. *IEEE Trans. on Aerosp.
           and Electron. Syst.*, AES-18(1):102–114, 1982.

[WHM21]   C. Waldschmidt, J. Hasch, and W. Menzel. Automotive Radar
           - From First Efforts to Future Systems. *IEEE J. of Microw.*,
           1(1):135–148, 2021.

[Wil88]   G.T. Wilfong. Motion planning for an autonomous vehicle. In
           Proc. 1988 IEEE Trans. Robot. Autom., pages 529–533 vol.1,
           1988.

[Win07]   V. Winkler. Range Doppler detection for automotive FMCW
           radars. In *2007 Eur. Rad. Conf.*, pages 166–169, 2007.

[Win09]   V. Winkler. Novel Waveform Generation Principle for short-
           range FMCW-Radars. In *Proc. German Microw. Conf.*, pages
           1–4, 2009.

[Win18]   C. Winkler. *Gemeinsame Realisierung von Chirp-Sequence-
           Radar und Funkkommunikation*. KIT, Karlsruhe, Dec 2018.

[WZ09]   H. Wu and T. Zwick. Automotive SAR for Parking Lot Detection.
           In *2009 German Microw. Conf.*, pages 1–8, 2009.

[Xil23]   Xilinx. *ZCU111 Evaluation Board User Guide*, 2023.

[XTW11]   Y. Xie, R. Tao, and T. Wang. Method of Waveform Design for
           Radar and Communication Integrated System Based on CSS.
           In *2011 Int. Conf. on Instrum., Meas., Comput., Commun. and
           Control*, pages 737–739, 2011.

[YMF06]   S. Yousefi, M. S. Mousavi, and M. Fathy. Vehicular Ad Hoc
           Networks (VANETs): Challenges and Perspectives. In *2006 6th
           In. Conf. on ITS Telecommun.*, pages 761–766, 2006.

Publications

[1] **M. B. Alabd**, B. Nuss, C. Winkler, and T. Zwick. Partial Chirp Modulation Technique for Chirp Sequence based Radar Communications. In *2019 16th Eur. Rad. Conf. (EuRAD)*, pages 173–176, 2019.

[2] L. Giroto de Oliveira, **M. B. Alabd**, B. Nuss, and T. Zwick. An OCDM Radar-Communication System. In *2020 14th Eur. Conf. on Antennas and Propag. (EuCAP)*, pages 1–5, 2020.

[3] L. Giroto de Oliveira, **M. B. Alabd**, B. Nuss, and T. Zwick. Range Association and Fusion in a Network of Single-Channel Monostatic OFDM Radars. In *2020 IEEE MTT-S Int. Conf. on Microw. for Intell. Mobility (ICMIM)*, pages 1–4, 2020.

[4] Y. Li, J. Eisenbeis, R. Michev, **M. B. Alabd**, and T. Zwick. Measurement-based Misalignment Analysis of Dual-polarized 2×2 LoS MIMO System at 28 GHz. In *2020 German Microw. Conf. (GeMiC)*, pages 152–155, 2020.

[5] **M. B. Alabd**, L. Giroto de Oliveira, B. Nuss, W. Wiesbeck, and T. Zwick. Time-Frequency Shift Modulation for Chirp Sequence based Radar Communications. In *2020 IEEE MTT-S Int. Conf. on Microw. for Intell. Mobility (ICMIM)*, pages 1–4, 2020.

[6] L. Giroto de Oliveira, B. Nuss, **M. B. Alabd**, Y. Li, L. Yu, and T. Zwick. MIMO-OCDM-based Joint Radar Sensing and Communication. In *2021 15th Eur. Conf. on Antennas and Propag. (EuCAP)*, pages 1–5, 2021.

[7] Y. Li, J. Eisenbeis, X. Wan, S. Bettinga, X. Long, **M. B. Alabd**, J. Kowalewski, T. J. Cui, and T. Zwick. A Programmable-Metasurface-Based TDMA Fast Beam Switching Communication System at 28 GHz. *IEEE Antennas and Wireless Propag. Lett.*, 20(5):658–662, 2021.

[8] L. Giroto de Oliveira, T. Antes, B. Nuss, E. Bekker, A. Bhutani, A. Diewald, **M. B. Alabd**, Y. Li, M. Pauli, and T. Zwick. Doppler Shift Tolerance of Typical Pseudorandom Binary Sequences in PMCW Radar. *Sensors*, 22(9), 2022.

[9] L. Giroto de Oliveira, B. Nuss, **M. B. Alabd**, A. Diewald, M. Pauli, and T. Zwick. Joint Radar-Communication Systems: Modulation Schemes and System Design. *IEEE Trans. on Microw. Theory and Techn.*, 70(3):1521–1551, 2022.

[10] L. Giroto de Oliveira, Benjamin Nuss, **M. B. Alabd**, A. Diewald, Y. Li, L. Gehre, X. Long, T. Antes, J. Galinsky, and T. Zwick. Discrete-Fresnel Domain Channel Estimation in OCDM-Based Radar Systems. *IEEE Trans. on Microw. Theory and Techn.*, pages 1–0, 2022.

[11] **M. B. Alabd**, B. Nuss, L. Giroto de Oliveira, A. Diewald, Y. Li, and T. Zwick. Modified Pulse Position Modulation for Joint Radar Communication Based on Chirp Sequence. *IEEE Microw. and Wireless Compon. Lett.*, 32(10):1247–1250, 2022.

[12] **M. B. Alabd**, B. Nuss, L. Giroto de Oliveira, Y. Li, A. Diewald, and T. Zwick. Preamble-Based Synchronization for Communication-Assisted Chirp Sequence Radar. *Proc. In Electromag. (PIER C)*, 127(10):31–48, 2022.

[13] Y. Li, S. Bettinga, L. de Oliveira Giroto, **M. B. Alabd**, J. Eisenbeis, X. Wan, X. Long, T. Cui, and T. Zwick. Predictive tracking implementation for mobile communication using programmable metasurface. *China Communications*, 20(8):137–152, 2023.

[14] Y. Li, S. Bettinga, F.r Gedenk, X. Long, **M. B. Alabd**, L. Giroto Giroto de Oliveira, and T. Zwick. Experimental Study of Channel Estimation Algorithms for General IRS Applications. In *2023 17th Eur. Conf. on Antennas and Propag. (EuCAP)*, pages 1–5, 2023.

[15] Y. Li, S. Bettinga, X.n Long, **M. B. Alabd**, L. Giroto de Oliveira, and T. Zwick. Experimental study of channel estimation and transmit diversity for irs-based miso system. In *2023 53rd European Microwave Conference (EuMC)*, pages 202–205, 2023.

[16] Y. Li, X. Long, L. Giroto de Oliveira, J. Eisenbeis, **M. B. Alabd**, S. Bettinga, X. Wan, T. J. Cui, and T. Zwick. Programmable Metasurface Hybrid MIMO Beamforming: Channel Estimation, Data Transmission, and System Implementations at 28 GHz. *IEEE Syst. J.*, 17(1):1270–1281, 2023.

[17] **M. B. Alabd**, J. Dittmer, J. P. Messmer, B. Nuss, Y. Li, J. Galinsky, and T. Zwick. A simulator for cacs-based radar systems in multi-user automotive scenarios. In *2023 20th European Radar Conference (EuRAD)*, pages 152–155, 2023.

[18] **M. B. Alabd**, J. Dittmer, Y. Nuss, B. Li, L. Giroto de Oliveira, A. Diewald, and T. Zwick. Time-frequency synchronization for cacs-based radar systems in interference scenarios. In *2023 20th European Radar Conference (EuRAD)*, pages 464–467, 2023.

[19] D. Brunner, L. Giroto de Oliveira, C. Muth, S. Mandelli, M. Henninger, A. Diewald, Y. Li, **M. B. Alabd**, Schmalen. L, T. Zwick, and B. Nuss. Bistatic ofdm-based isac with over-the-air synchronization: System concept and performance analysis. *IEEE Trans. on Microw. Theory and Techn.*, pages 1–0, 2024.

[20] **M. B. Alabd**, L. Giroto de Oliveira, B. Nuss, Y. Li, A. Diewald, J. Galinsky, Z. Kollár, and T. Zwick. Communication-assisted chirp sequence radar with improved data rate. *IEEE Microw. and Wireless Lett.*, 34(10):1214–1217, 2024.

[21] **M. B. Alabd**, B. Nuss, L. Giroto de Oliveira, Z. Kollár, and T. Zwick. Analysis of Interference Effects on CaCS-based Radar Systems. *Int. J. of Microw. and Wireless Techn.*, Accepted in (2024).